Precast Lightweight Foamed Concrete Walling, a Structural System for Low-Rise Residential Buildings

by

Trevor Paul Andrew Dunn

Thesis presented in partial fulfilment of the requirements for the degree of Master of Structural Engineering in the Faculty of Engineering at Stellenbosch University

Supervisor: Prof. Gideon P.A.G van Zijl

Co-supervisor: Mr. Algurnon S. van Rooyen

December 2017

Declaration

By submitting this thesis electronically, I declare that the entirety of the work contained therein is my own, original work, that I am the sole author thereof (save to the extent explicitly otherwise stated), that reproduction and publication thereof by Stellenbosch University will not infringe any third party rights and that I have not previously in its entirety or in part submitted it for obtaining any qualification.

Date: December 2017

Abstract

Precast Lightweight Foamed Concrete Walling, a Structural System for Low-Rise Residential Buildings

T.P.A. Dunn

Department of Structural Engineering,
University of Stellenbosch,
Private Bag X1, Matieland 7602, South Africa.

Thesis: MEng (Civil)

October 2017

Lightweight foamed concrete, in contrast to normal weight concrete, is a low density, zero coarse aggregate concrete. The applications of foamed concrete have previously been non-structural and made use of the aesthetic, thermal, fire-resistant and void filling properties. These existing properties make lightweight foamed concrete an ideal building material for residential building construction, thus the material is now being developed into a building material for structural applications.

Previous research in the structural use of lightweight foamed concrete has focussed on the specific material properties and durability of the material. Contributing to the Centre for Development of Sustainable Infrastructure research unit, this study aims to contribute to the development of a reinforced lightweight foamed concrete building system as a substitute for unreinforced load-bearing masonry construction in low-rise (one to four storey) residential buildings in the South Western Cape of South Africa. This region of South Africa is a low to moderate seismic region which requires that the proposed building system be seismically sufficient.

A prototype lightweight foamed concrete building is the basis for the study, from which a wall segment is tested. An additional feature of the building system is the incorporation of precast construction; where load-bearing wall panels would be made in a factory and transported to the site for rapid yet high-quality construction. For the selected wall panel, the top and bottom (ground and floor slab) connections are grouted dowel connections in compliance with international precast construction standards for seismic regions. Bespoke mechanical connection boxes are used for the vertical connections between adjacent wall panels. These vertical connections are placed at the centre of the wall segment to allow for in-plane testing of two adjacent walls.

The testing of these wall panels is conducted according to precast concrete connection testing guidelines, as it is envisaged that stress concentrations at the connections will determine the seismic resistance of the walls. Three different physical tests are conducted on 1:3 scale wall panels from a single face of the prototype building. The first and third walls are tested via monotonic pull-over load action. These wall specimens vary in degree of grouted dowel reinforcement across their horizontal connections. The second wall is tested via quasi-static cyclic loading to determine the energy dissipation behaviour of the precast, lightweight foamed concrete building system. The objective of these tests is to determine the displacement behaviour and precast concrete connection behaviour under seismic load.

A lightweight foamed concrete finite element material model and finite element simulation of both pull-over tests are created. A further sensitivity study to establish the dependence of the walling system computed response to changes of connection interface friction, tensile and compressive strength, and connection dowel size is conducted. The aim of this numerical analysis is to provide information regarding the failure mechanisms within the precast wall assembly.

The results of the physical tests indicate that the wall's capacity to withstand lateral pull-over force is significantly affected by changes to the degree of dowel reinforcement crossing the horizontal connections. The observed energy dissipation for the cyclic tests indicates that connecting dowel number and placement also influence the displacement mechanisms of the wall and the observed cracking indicates sound in-plane behaviour of the wall system.

The finite element test results highlight the individual nonlinear displacement regions before ultimate slip failure at the horizontal connections. A normalisation study reveals that these regions are present at the same relative displacement within both the physical tests and numerical simulations.

An analytical model is proposed, which focusses on the results of the sensitivity study conducted that highlight the significant effect that changes to friction and dowel-diameter have on the ultimate capacity of horizontal connections. These properties are seen to allow ductile failure over large displacements. This analytical model shows that the shear capacity of these connections determine the lateral force resistance of the precast walls.

It is concluded that precast design for the proposed building system successfully dissipates energy, provided that care is taken for connection placement to prevent brittle failure. It is further concluded that reinforced lightweight foamed concrete walls give a ductile and predictable response, failing at lateral loads beyond the seismic demand in the region of interest.

Uittreksel

Precast Lightweight Foamed Concrete Walling, a Structural System for Low-Rise Residential Buildings

T.P.A. Dunn

Departement Struktuur Ingenieurswese,
Universiteit van Stellenbosch,
Privaatsak X1, Matieland 7602, Suid Afrika.

Tesis: MIng (Siviel)

Oktober 2017

Liggewig skuimbeton, in teenstelling met gewone gewigbeton, is 'n lae digtheid beton sonder growwe aggregaat. Die toepassings van skuimbeton was voorheen nie-struktureel en het gebruik gemaak van die estetiese, hitte-, brandbestande en opvul eienskappe. Hierdie eienskappe maak liggewig skuimbeton 'n ideale boumateriaal vir residensiële boukonstruksie, dus word die materiaal nou ontwikkel tot 'n boumateriaal vir strukturele toepassings.

Vorige navorsing in die strukturele gebruik van liggewig skuimbeton het gefokus op die spesifieke materiaaleienskappe en duursaamheid van die materiaal. As bydrae tot die Sentrum vir Ontwikkeling van Volhoubare Infrastruktuur-navorsingseenheid, is hierdie studie daarop gemik om by te dra tot die ontwikkeling van 'n bewapende liggewig skuimbeton stelsel as 'n plaasvervanger vir onbewapende lasdraende messelwerk konstruksie in lae (een tot vier verdieping) residensiële geboue in die Suid-Wes-Kaap van Suid-Afrika. Hierdie streek van Suid-Afrika is 'n lae tot matige seismiese streek wat vereis dat die voorgestelde boustelsel seismies bestand sal wees.

'n Prototipe liggewig skuimbeton gebou is die basis vir die studie, waaruit 'n muursegment getoets word. 'n Bykomende kenmerk van die boustelsel is die inkorporering van voorafvervaardigde konstruksie; waar lasdraende muurpanele in 'n fabriek gemaak word en na die terrein vervoer word vir vinnige, maar hoë gehalte konstruksie. Vir die geselekteerde muurpaneel is die boonste en onderste (grond- en vloerplaat) verbindings mortel gevulde dwarsstaaf verbindings wees in ooreenstemming met internasionale standaarde vir seismiese gebiede. 'n Geskikte meganiese verbindingsmeganisme word gebruik vir die vertikale verbindings tussen aangrensende muurpanele. Hierdie vertikale verbindings word in die middel van die

muursegment geplaas om die toets van in-vlak gedrag van twee aangrensende mure toe te laat.

Die toets van hierdie muurpanele word uitgevoer volgens die riglyne vir voorafvervaardigde beton verbindingstoets, aangesien dit verwag word dat spanningskonsentrasies by die verbindings die seismiese weerstand van die mure sal bepaal. Drie verskillende fisiese toetse word uitgevoer op 1:3 skaalmuurpanele van 'n enkele aansig van die prototipe gebou. Die eerste en derde mure word getoets deur monotone skuifbelasting. Hierdie muur toetspanele wissel in aantal dwarsstaaf verbindings oor hul horisontale verbindings. Die tweede muur word getoets deur middel van kwasi-statiese, sikliese skuifbelasting om die energie dissipasie van die voorafvervaardigde, liggewig skuimbeton boustelsel te bepaal. Die doel van hierdie toetse is om die verplasingsgedrag en die beton verbindingsgedrag onder seismiese las te bepaal.

'n Liggewig skuimbeton eindige element materiaalmodel en eindige element simulasie van beide skuiftoetse word geskep. Verdere sensitiwiteitstudies word uitgevoer om die afhanklikheid van die boustelsel se berekende gedrag te bepaal van varierende verbindingskoppelvlak wrywing, trek-en-druksterkte, en verbinding dwarsstaaf dikte. Die doel van hierdie numeriese analise is om inligting te verskaf rakende die falingsmeganismes in die voorafvervaardigde muurmontering.

Die resultate van die fisiese toetse dui daarop dat die muur se kapasiteit om dwarsskuif te weerstaan, noemenswaardig affekteer word deur veranderinge in die aantal dwarsstawe in die horisontale verbindings. Die waargenome energiedissipasie in die sikliese toetse dui daarop dat die dwarsstaaf verbindingsaantal en -plasing ook die verplasingsmeganismes van die muur beïnvloed, en die waargenome krake dui aan dat die in-vlak gedrag van die muurpanele struktureel geskik is.

Die eindige element resultate beklemtoon die individuele nie-lineêre verplasingsbereike voor die uiteindelike glipfaling in die horisontale verbindings. 'n Normaliseringstudie toon dat hierdie verplasingsbereike in dieselfde relatiewe gebiede in beide die fisiese toetse en numeriese simulasies voorkom.

'n Analitiese model word voorgestel, wat fokus op die resultate van die sensitiwiteitstudie wat die noemenswaardige effek wat verandering in die wrywing en dwarsstaaf-deursnee het op die uiteindelike kapasiteit van horisontale verbindings, beklemtoon. Hierdie eienskappe word gesien as instrumenteel tot duktiele faling oor groot verplasings. Hierdie analitiese model toon dat die skuifkapasiteit van hierdie verbindings die laterale weerstand van die voorafvervaardigde mure bepaal.

Daar word tot die gevolgtrekking gekom dat die ontwerp vir die voorgestelde voorafvervaardigde boustelsel suksesvol energiedissipasie tot gevolg het, met dien verstande dat verbindings sorgvuldig ontwerp word om bros faling te voorkom. 'n Verdere gevolgtrekking is dat gewapende liggewig skuimbetonmure 'n duktiele en voorspelbare reaksie het, wat faling onder dwarsbelasting toon wat die vereiste seismiese aksie van die streek van belang oorskry.

Acknowledgements

Even though this thesis is my own work, it would not have been possible without the support and assistance of a few key individuals. I am incredibly grateful for the opportunity to study further and would like to thank the following faculty staff members, friends and family for their involvement:

- To my industry contacts: Mr Thomas Swana of UkuZwana Project Management Solutions (Pty) Ltd., Mr Walter Botes of Cape Concrete Works and Mr Gustav Kroeger for their respective contributions to the field of foamed concrete construction and their advise on this project. More specifically, Mr Thomas Swana for his prototype foamed concrete building design.

- Mr Arthur Layman, Ms Natalie Scheepers and Mrs Olivia van Wyk for your efficient administration, for dealing with my frustrations over the last few years and for your warm and welcoming hearts.

- The structural and concrete laboratory staff and in particular: Mr Johan van der Merwe and Mr Deon Viljoen for their expert advice on my test setup and friendly conversations in between. To Dr Stephan Zeranka, for his meticulous planning and help with the complex laboratory test setup.

- To the foamed concrete team and fellow members of the Centre for Development of Sustainable Residential Infrastructure.

- To my co-supervisor and friend: Mr Tata van Rooyen for his passion for foamed concrete and support during this thesis

- To my office colleagues and friends: For the two-year journey we have had and for helping me define "complimentary studies".

- To my incredible supervisor Prof Gideon van Zijl: For his astounding work ethic, his passion for students and his great sense of humour.

- To my parents and family: To my dad, an engineer by experience who inspired me to take my passion further. To my mom, for her love, support and prayers. To my brother, for always being proud of me.

- To my beautiful wife Lauren: For her continued love, support and hard work that inspired me to give this thesis my best effort.

Dedications

This thesis is dedicated to my Lord and Saviour, Jesus Christ.
"Unless the Lord builds the house, the builders labour in vain.- Psalm 127:1

Contents

List of Figures

List of Tables

Nomenclature

Abbreviations

AAC	Autoclaved Aerated Concrete
ACI	American Concrete Institute
a/c	Ash-Cement Ratio
ASTM	American Society for Testing and Materials
BE	Beam-End
BFGS	Broyden-Fletcher-Goldfarb-Shanno Algorithm
c/c	Centre-to-centre
CEB	Comity Euro-International de Beton
CMOD	Crack Mouth Opening Displacement
CoV	Coefficient of Variation
EN	European Design Codes
FE	Finite Element
FEA	Finite Element Analysis
FEM	Finite Element Model
LSB	Limited-slip-bolted
LVDT	Linear Variable Differential Transformer
LWFC	Lightweight Foamed Concrete
LWAC	Lightweight Aggregate Concrete
MTM	Materials Testing Machine
NZS	New Zealand Standards
NWC	Normal Weight Concrete
PST	Physical Scale Test

PO	Push, Pull-Over
PST	Physical Scale Test
PPC	Pretoria Portland Cement
PO	Pull-out
RC	Reinforced Concrete
S/C	Sand-Cement Ratio
SLS	Serviceability Limit State
SABS	South African Bureau of Standards
SANS	South African National Standard
TPBT	Three Point Bending Test
ULS	Ultimate Limit States
UTT	Uniaxial Tensile Tests
w/a	Water Ash Ratio
w/c	Water Cement Ratio
w/s	Water Sand Ratio

Variables

A	Cross-sectional Area of Specimen
A_A	Accidental Action
A_E	Seismic Action
A_e	Element Area
A_s	Area of Tension Reinforcement
$A_{s,w}$	Area of Outer Vertical Wall Reinforcement
a_v	Joint Shear Span
a_g	Gravitational Acceleration
b	Effective Width
B_b	Percentage Redistribution
c_r	Coefficient for Aggregate Interlock
C_R	Empirical Coefficient
C_x	Anchor Edge Distance

d	Effective Depth
d_0	Original Diameter
d_a	Anchor Head Width
d_w	Wall Effective Depth
E	Young's Modulus of Elasticity
f_{bu}	Ultimate Anchorage Bond Strength
f_{ck}	Concrete Compressive Cylinder Strength
f_{ct}	Concrete Tensile Cylinder Strength
f_{cm}	Average Value of Concrete Compressive Strength Results
f_{cu}	Concrete Compressive Cube Strength
f_{cub}	Concrete Compressive Cube Base Strength
$f_{i,max}$	Maximum Force
F_s	Applied Force
F_h	Horizontal Splitting Force
F_v	Applied Vertical Force
f_s	Stress in Reinforcement Bar
f_t	Concrete Tensile Strength
f_u	Ultimate Strength of Reinforcement Bar
f_y	Yield Strength of Reinforcement Bar
G	Permanent Action
G	Shear Modulus of Rigidity
G_f	Mode-I Fracture Energy
h	Crack Bandwidth
h_e	Element Size
K_n	Normal Stiffness
K_s	Shear Stiffness
L	Length of Bar
l	Anchorage Length
L_0	Original Gauge Length

L_c Parallel Length

l_c Characteristic Length

M Design Moment

Q Variable Action

$RD_{f,c,a,s}$ Relative Density of Foam, Cement, Ash and Sand

s_{max} Reinforcement Slip, Maximum

S_0 Original Cross-sectional Area of Parallel Length

$std(f_c)$ Standard deviation of Concrete Compressive Strength Results

S_x Anchor Spacing

$Sd(T)$ Design Response Spectrum

T_f Tensile Force Resistance

t_t Shear Traction

U_i Dissipated Energy

u_i Specific Energy

V Design Shear Force

V_e Volume of Element

$V_{F,max}$ Dowel Action Force Resistance

v Design Shear Stress

v_c Shear Resistance

$V_{Rd,s}$ Nominal Shear Resistance for a Group of Anchors

V_f Foam Volume

V_w Shear Force in Wall

x Section Natural Axis Depth

x_c Cement Content

z Section Lever Arm

$z_{0.05}$ 5 Percentage Point of the Random Variable

α Reinforcement Inclination Angle

α_b Binder Ratio

α_w Wedge Angle

γ	Partial Factor
γ_c	Material Factor for Concrete
γ_m	Material Factor for Reinforcement
κ_1	Interaction Effectiveness Factor
κ_2	Interaction Coefficient for Flexural Resistance
μ	Coefficient of Static Friction
μ_{duct}	Structural Ductility Factor
ν	Poisson's Ratio
ω_{cr}	Principle Crack Width
ψ	Combination Factor
Ψ	Reduction Factors
ρ_t	Design Target Plastic Density
ρ_{dry}	Cured Dry Density
σ	Stress
σ_1	Principle Stress
σ_a	Upper Stress
$\sigma_{a,m}$	Measured Stress Corresponding to Nominal Upper Stress, σ_a
σ_b	Lower Stress
σ_d	Design Bond Stress
σ_p	Applied Nominal Pre-load Stress
$\sigma_{p,m}$	Measured Stress Corresponding to Nominal Preload Stress, σ_p
τ_a	Shear Resistance, Adhesion
τ_{Rdi}	Shear Resistance, Design Limit
τ_u	Shear Resistance, Ultimate
$\triangle u_t$	Shear Slip
$\triangle u_y$	Displacement Amplitude y
ε	Strain
ε_1	Total Principle Strain
$\varepsilon_{1,e}$	Elastic Principle Strain

$\varepsilon_{a,3}$ Average Strain at Maximum Stress on Loading Cycle 3

ε_{cr} Principle Crack Strain

$\varepsilon_{p,2}$ Average Strain at Minimum Stress on Loading Cycle 2

Subscripts

ave Available

c Concrete

hor Horizontal

max Maximum

min Minimum

$prov$ Provided

req Required

s Steel

Chapter 1

Prelude

This chapter presents an introduction on the thesis to justify the research work. After providing background information the reader is given a brief summary of the thesis scope and objectives that this work has set out to achieve. Finally the research limitations are explained and a brief chapter outline is provided.

1.1 Background

Current residential housing systems in the Western Cape, South Africa mainly make use of concrete block or unreinforced masonry (URM) construction for low-rise residential infrastructure (Figure (1.1)). These buildings have often been quickly assembled and are seismically susceptible as quality control remains a challenge with this cost effective and widely available construction method.

Reinforced masonry construction with explicit detailing and concrete infill of masonry walls is an improvement to URM construction. This construction method is however labour intensive and requires a complicated and costly detailed design. As a result of these challenges many low-rise residential buildings are built without earthquake protection and are at risk of collapsing should a seismic event occur (Hancilar *et al.*, 2010).

Lightweight Foamed Concrete (LWFC) has been successfully utilised non-structurally to provide thermal insulation in wall panels, in the form of a void filler for restoring level ground in Geotechnical and mining applications as well as in highway construction (Jones and McCarthy, 2005; Kearsley, 1996). Likely advantages for the structural use of LWFC are listed below:

- Lighter weight construction leads to reduced gravitational acceleration forces for seismic design and reduced transport costs.

- Thermal superiority to masonry construction and improved climate, comfort level for inhabitants.

- Noted acoustic insulation for increased comfort.

- Fire risk reduction as a property of insulating walls.

- Higher quality buildings due to controlled factory production.

1

- Quicker assembly time due to large precast LWFC panels.

- Overall lower cost over construction lifetime due to heating, cooling costs.

It has been noted by Jones and McCarthy (2005) that LWFC has significant potential to be used as a competitive structural material provided that a revised structural system is created to take into account the difference in mechanical behaviour of LWFC.

Figure 1.1: *Typical unreinforced masonry low-rise residential building in the Cape Flats of South Africa (De Beer, 2016)*

Reinforcement bond effectiveness in LWFC is an example of a weak mechanical behaviour and is significantly lower than normal weight concrete (NWC). It was successfully tested by De Villiers (2015) who determined that LWFC is not yet capable of replicating the bond strength of NWC and that material properties or system design modification will be required (De Villiers *et al.*, 2017).

The existing insulating properties of LWFC make it an ideal building material for residential construction. The possible advantages of a successfully implemented LWFC structure would make it a preferable building material to reinforced masonry construction once these positive material properties are harnessed and differing mechanical behaviour is accounted for in appropriate structural design (Oginni, 2015; Narayanan and Ramamurthy, 2000).

LWFC incorporated into a reinforced concrete building system has the potential to make a great contribution in the area of residential infrastructure and high-density low-rise housing.

1.2   Thesis Scope

The focus of this research is regarding the structural behaviour of a proposed LWFC building system.

This project aims to move forward with the current knowledge on specific mechanical properties of LWFC such as the compressive and tensile strength, limited reinforcement

bond, Young's modulus and fracture energy, and aims to understand the structural behaviour of a LWFC builing.

The investigation focusses on developing a method of construction using LWFC wall panels and testing the material and construction method under seimic load with verification via finite element modelling. The overall aim is to contribute to the development of a reinforced LWFC building system and the codification of LWFC structural design.

1.3 Research Objectives

The structural use of LWFC is still in it's infancy with research studies focussing currently on either material development and mechanical properties or localised failure under axial load. The plan to move beyond micro testing and investigate overall structural behaviour of LWFC in pre-cast concrete construction is the goal of this project. Itemised in the following list are the further objectives to achieve this goal.

(i) Establish the main hindrances to utilising LWFC in structural engineering applications in the South African construction industry.

(ii) Formulate a non-linear material model for the numerical analysis of LWFC.

(iii) Develop a structural system for construction of low to medium rise residential infrastructure using LWFC.

(iv) Test a proposed LWFC structural system for equivalent quasi-static seismic loading.

(v) Propose a reinforced LWFC wall design guideline for future incorporation into a design guideline for the structural use of LWFC.

1.4 Research Limitations

The mechanical connection boxes at the vertical joint between wall panels are based on a design developed by Cape Town based precast concrete manufacturer Cape Concrete CCW (2017). As no other connection of this type exists, it is considered that this is the current "best practice" for the connection of LWFC wall panels.

The research of this thesis is limited to testing LWFC walling systems and not a global full-scale structure. The design considered in this research therefore is focused on load bearing LWFC walls, making use of existing NWC hollow-core flooring and neglecting the design of spanning LWFC members for flexural strength.

These initial tests are limited to in-plane loading via cyclic (equivalent quasi-static) and push-over testing as per JRC Policy Report: *Design guidelines for connections of precast structures under seismic actions* (Negro and Toniolo, 2012) in contrast to site specific seismic time-history analysis to obtain a better comparable benchmark for the structural system.

The detailed design of the monolithic connection between the top of LWFC panels and spanning hollow-core floor slabs is out of the scope of this thesis. For understanding on the strengths and limitations of monolithic hollow-core connections the reader is directed to the literature of Fenwick *et al.* (2010) and Jensen *et al.* (2007).

1.5   Draft Chapter Overview

The first chapter of this thesis introduces the research goal and objectives. The second, literature review chapter evaluates the task at hand and attempts to provide the reader with background information to contextualise the research. Experimental design chapter three outlines the physical testing regime and laboratory setup required. This chapter further explains likely characteristic tests for clarification and justification of test results. The fourth chapter explains the numerical analyses and finite element (FE) test parameters to simulate the physical tests of chapter three. The FE material model development is elaborated alongside preliminary FE test results at the end of chapter four. The fifth, results chapter will give a thorough overview of both the physical test, finite element and characteristic test results.

Chapter six gives a summary of the preceding chapters and the influential parameters of the sensitivity study. It is concluded with a section on analytical design for lateral resistance of precast, reinforced LWFC walls.

Chapter seven concludes the report, containing a conclusion of the test data and interpretation as well as a section regarding recommendations for future research. This final section provides the reader with an understanding of the successes and challenges of the research and recommends future research areas for investigation.

Chapter 2

Literature Review

This chapter unpacks current literature on lightweight foamed concrete (LWFC) to give a basis for further research and development. References are made to the current mix design, uses and successful applications of LWFC as well as providing an idea of the current research gaps and weaknesses to using LWFC in the place of normal weight concrete (NWC). Thereafter the reader is given a brief introduction to seismicity in South Africa and the requirements for a new structural system in a seismic region. The chapter is finally concluded with a section on precast concrete, the proposed construction method for LWFC.

2.1   Lightweight Foamed Concrete

2.1.1   Introduction

Lightweight foamed concrete is comprised of cement, fly ash and water and makes use of a stable, slowly degenerating, low density foam in place of conventional concrete aggregate. This addition of the substantially lighter foam content leads to a low density "concrete" with microscopic air voids forming.

The motivation for creating LWFC for structural purposes is to exploit the low thermal inertia and insulation properties, as well as the self-compacting nature of the material. The lighter mass of the structure, $800 - 1600 \ kg/m^3$ for LWFC in contrast to $2400 \ kg/m^3$ for normal weight concrete (NWC) leads to lower inertia for seismic accelerations during an earthquake and also makes it possible for entire walls to be made as a single uniform precast panel with the likelihood of better quality control and scalable factory production (Kearsley, 1996).

It is important to add that LWFC is different from Lightweight Aggregate Concrete (LWAC) and Autoclaved Aerated Concrete (AAC), which have been proven to be structurally sound with reference in both BSI (2004) and fib Model Code (2010). Autoclaving is an energy intensive process and lightweight aggregate is not widely available in South Africa, thus LWFC as a structural material is being explored. LWFC if not yet accepted as a structural material as no official design codes or guidelines exist for its use. Concerns mentioned by Jones and McCarthy (2005) are that the flexural strength and reinforcement bond of LWFC still requires a better understanding of the mechanical properties of the material and that a direct substitution for its NWC counterpart is ill-advised.

De Villiers *et al.* (2017) further explored the bond and structural mechanics of LWFC but concluded that both the fracture energy and bond behaviour of LWFC is significantly lower than NWC, requiring material refinement before advanced structural testing.

2.1.2   Mixing of LWFC

Mixing of LWFC begins with the formation of a base mixture where water is slowly added to dry ingredients of cement, sand or fly ash - a waste product from coal electricity production. Large stockpiles of this waste material exist in North and central South Africa.

The addition of fly ash as a cement extender was tested by Kearsley and Wainwright (2001), as well as incorporated in the mix design procedure of Jones and McCarthy (2005). Kearsley and Wainwright (2001) concluded that up to two-thirds replacement of cement with fly-ash is possible; noting a slight reduction in early-age strength, and an improvement of long-term strength of LWFC (Van Rooyen, 2013; Jones and McCarthy, 2005; Kearsley and Wainwright, 2002). More benefits of fly ash include a potential decreased heat of hydration and a decrease in overall cost of construction, which render fly-ash a staple ingredient in a LWFC mix.

Preformed foam is created under pressure, with a 1 : 40 (by volume) mixture of hydrolysed protein foaming agent and water. Sulphate powder is added to the amount of 1.25 *g* per litre of the mixture. The mixture is aerated to form a stable foam at a target density of $75g/l$ (Kearsley and Mostert, 2003).

The foam and the base paste mix, i.e. water, cement and fly ash (and/or fine aggregate) are prepared separately, after which they are combined and further mixed to disperse the foam in the composite. It is important to add enough water to form a homogeneous paste mixture and allow for cement hydration, without the hydration process re-claiming moisture from the foam itself, thereby counteracting the density reduction of the foam (Kearsley and Wainwright, 2001). Whereas water plays an important role in strength in NWC; the foam and the eventual air voids it creates are of most significance in LWFC.

The mixing process of LWFC requires a "folding-in" of the foam into the denser base mix to prevent foam degeneration. This process of adding foam can be performed in a step-wise manner with additional foam added to achieve a target plastic density, the main influence of ultimate compressive strength of LWFC, which reduces with a reduction in density (Kearsley and Wainwright, 2001; Jones and McCarthy, 2005).

2.1.3   Compressive Strength

In NWC the compressive strength is governed by the water to cement ratio (w/c). In LWFC w/c is of less importance and air void content, and thus the composite density, dominates the compressive strength (Kearsley and Wainwright, 2001).

It was determined by Jones and McCarthy (2005) that the ultimate compressive strength f_{cu} of LWFC is directly related to its dry density, reducing with a reduction in density. This was later confirmed by Kearsley and Wainwright (2001) through physical tests. A dry density of 1400 kg/m^3 (target casting density of 1550 kg/m^3) will give the lower limit of structurally viable LWFC according to (Jones and McCarthy, 2005).

Kearsley and Wainwright (2001) found that f_{cu} of LWFC is only marginally affected by the percentage cement replaced by fly-ash granted that the target dry density is achieved.

It was further reported that the fly ash grading had a negligible effect on the ultimate strength.

The base mix compressive strength before foam addition f_{cub} (MPa) is given by equation (2.1). In this equation t is the time in days since casting and W/C is the effective water-cement ratio determined via equation (2.2), which also incorporates the ash-cement ratio a/c (by weight) and actual water cement ratio w/c. The cementing efficiency k is determined via equation(2.3) and gives reference to the work of Smith (1967). However it moves past the assumption of a constant cementing efficiency and shows a less conservative yet positive improvement of k over time (Kearsley and Wainwright, 2001) .

$$f_{cub} = 88.04 + 6.569ln(t) - 130.5(W/C) \tag{2.1}$$

$$W/C = (w/c)\left[\frac{1}{1 + k(a/c)}\right] \tag{2.2}$$

$$k = \left(0.457 + 0.00315\left(\frac{t}{a/c + 1}\right)\right)^2 \tag{2.3}$$

Thereafter Kearsley and Wainwright (2001) developed Equation (2.4) to predict long term compressive strength of LWFC by combining Equations (2.3), (2.2) and (2.1). Equation (2.4) was plotted against time for different target densities by De Villiers (2015) to show the predicted increase in compressive strength for fly-ash replacement of cement.

$$f_{cu} = 1.172f_{cub}(\alpha_b)^{3.7} \tag{2.4}$$

Where:
α_b is the binder ratio

Choosing to add fly-ash instead of adding fine sand to the LWFC doubled the compressive strength of the material at 56 days, prompting the mix design in Section (2.1.2) and a recommendation that the test age for LWFC be 56 days to allow for fly-ash strength development(Jones and McCarthy, 2005). Further, to significantly increase compressive strength Jones and McCarthy (2005) explain that w/c could be reduced through the development of specialised admixtures that are compatible with foamed concrete.

2.1.4   Tensile Strength

Jones and McCarthy (2005) performed split cylinder tensile strength tests on LWFC mixes both with sand and fly-ash addition. The improved tensile strength of the sand mixes was assumed to be a result of the improved shear capacity between the larger sand particles compared with that of the paste. The tensile to compressive strength relationship was therefore lower for the LWFC with fly-ash inclusion than both the NWC and LWAC mixes at the same compressive strength. This can be seen in Figure (2.1) where the results of Jones and McCarthy (2005) are plotted against known relationships for NWC (Equation (2.5)), (Oluokun, 1991)) and LWAC (Equation (2.6), (FIP, 1983)) concretes.

$$f_{ct} = 0.2(f_{cu})^{0.7} \tag{2.5}$$

$$f_{ct} = 0.23(f_{cu})^{0.67} \tag{2.6}$$
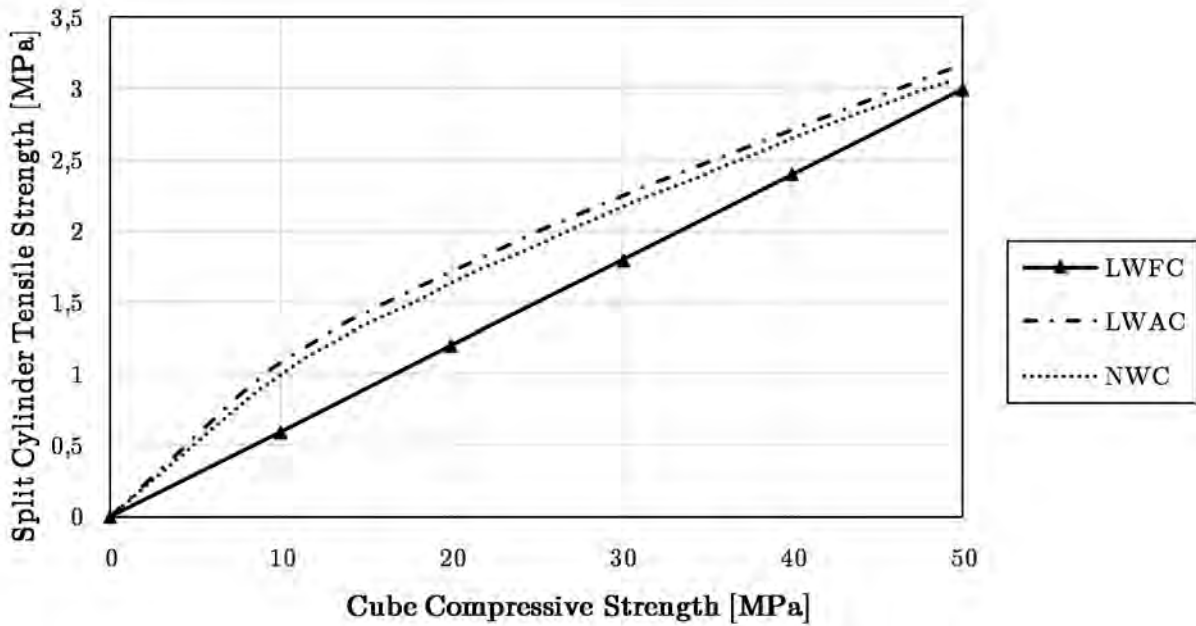
Figure 2.1: *Relationship between the concrete compressive cube strength and split cylinder tensile strength of LWFC obtained by Jones and McCarthy (2005) and the same relationship for LWAC (FIP, 1983) and NWC (Oluokun, 1991) (De Villiers, 2015; Jones and McCarthy, 2005).*

As seen in Figure (2.1) the compressive strength of LWFC is comparable to that of its NWC and LWAC counterparts. However the tensile strength and relationship between tensile and compressive strength are distinctly lower. De Villiers *et al.* (2017) was able to improve this relationship slightly. The authors postulated that adding either coarse aggregate or fibre reinforcement might lead to comparable tensile strength.

2.1.5 Young's Modulus

In Figure (2.2) the Young's modulus (E) of De Villiers *et al.* (2017) with fly-ash replacement LWFC are compared with the LWFC of Jones and McCarthy (2005) (Equations (2.7) and (2.8)) with reference to NWC and LWAC. It is seen in Figure (2.2) that the mechanical properties of LWFC are lower than their NWC and LWAC counterparts. In this figure Equations (2.9) and (2.10) are plotted from fib Model Code (2010) §5.1.7.2, equations 5.1-21 and 5.1-22.

$$E = 0.99 f_c^{0.67} \tag{2.7}$$

$$E = 0.42 f_c^{1.18} \tag{2.8}$$

$$E_{ci} = E_{c0} \alpha_E \left(\frac{f_{cm}}{10} \right)^{\frac{1}{3}} \tag{2.9}$$
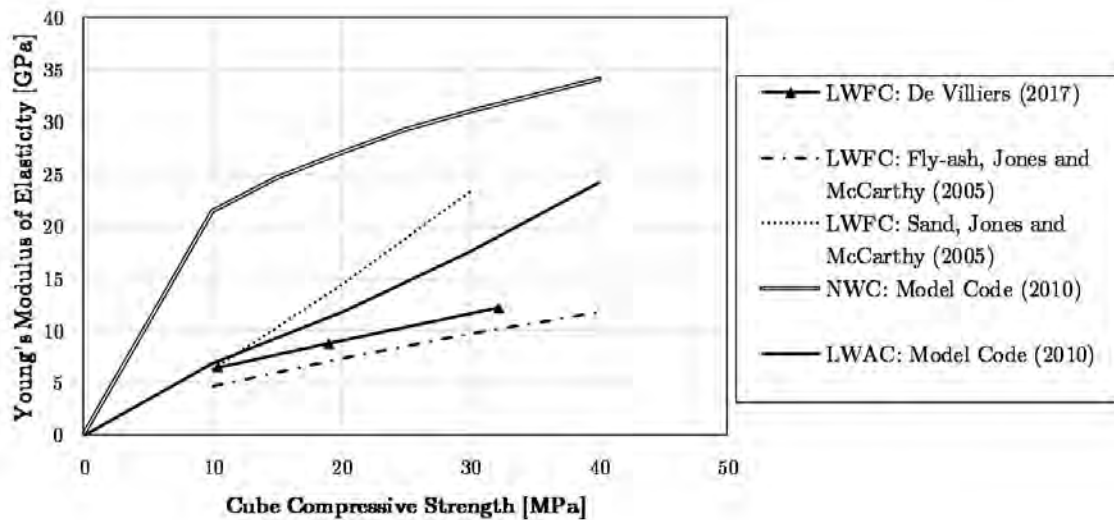
Figure 2.2: *Young's Modulus Comparison between NWC (fib Model Code, 2010), LWAC (fib Model Code, 2010) and LWFC (De Villiers et al., 2017; Jones and McCarthy, 2005)*

$$E_{lci} = \eta_E E_{ci} \qquad (2.10)$$

Where:

$\eta_E = \left(\frac{\rho}{2200}\right)^2$
$\alpha_E = 1.0$
f_{cm} is the median compressive strength
f_c is the 100 mm cube strength

Considering Figure (2.2), it is notable that the Young's modulus values for LWFC of De Villiers *et al.* (2017) and Jones and McCarthy (2005) are similar, but both slightly lower than the LWAC projections of fib Model Code (2010). Although LWFC and LWAC have lower Young's moduli than NWC, the similarity in LWFC and LWAC Young's moduli makes the former a viable structural material (De Villiers, 2015).

Jones and McCarthy (2005) and De Villiers *et al.* (2017) conclude that the direct substitution of NWC for LWFC of the same compressive strength is not advised, as it will be unsafe for structural design; citing the reduced tensile splitting strength. Jones and McCarthy (2005) do propose that the structural use of LWFC is a "realistic proposition", but will require new design methods.

2.1.6 Reinforcement Bond

Research on reinforced LWFC was conducted by De Villiers *et al.* (2017). Pull-Out (PO) and Beam-End (BE) bond tests were performed on LWFC of varying densities, rebar diameters and embedded lengths to obtain the bond stress (σ_d). The LWFC specimens were fully characterised and compared to the NWC results of Wittmann (2002) as a reference. The mix design and characteristic test results are summarised in Table (2.1).

Leonhardt and Mönnig (1977) suggest a physical measure of design bond stress as the average bond stress when the bar has a free-end slip of 0.1 mm. The free-end is as depicted

Table 2.1: *Mix design and characteristic test results of De Villiers* et al. *(2017), citing Wittmann (2002) for *NWC results.*

Concrete	**12F**	**14F**	**16F**	***NWC**
Target Casting Density [kg/m^3]	1200	1400	1600	2366
Base Mix Density [kg/m^3]	1881	1881	1881	2366
CEM II-52.5 [kg]	447.2	526.73	606.2	336.2
Fly-ash, Class S [kg]	447.2	526.73	606.2	0
Coarse aggregate [kg]	0	0	0	1000
Sand [kg]	0	0	0	835
Water [$Litre$]	277.3	326.6	375.9	195
Foam [$Litre$]	377	266.3	155.5	0
Compressive strength, fcu [MPa] (cube)	10.41	19.1	32.26	38.66
Coefficient of Variation (CoV) [%]	0.057	0.053	0.105	0.038
Young's Modulus, Ec [GPa]	6.46	8.75	12.15	*38.0
CoV [%]	0.03	0.001	0.022	0
Indirect Tensile strength, ft [MPa]	1.31	2.14	3.63	*1.9
CoV [%]	0.061	0.062	0.092	0
Fracture energy, Gf [N/m]	4.67	5.72	7.32	*123.55
Characteristic Length, lc [mm]	17.58	10.93	6.75	*1300

by De Villiers *et al.* (2017) as the end of either the BE or PO tests to which no tension is applied. Figure (2.3) compares the calculated bond stress results for both the BE and PO LWFC tests with NWC results from SANS (2000) and BSI (2004).

De Villiers *et al.* (2017) derived from these tests that the PO design bond stress of LWFC varied linearly with compressive strength and the BE tests did not, flattening with an increase in f_{cu}. The authors ascribed this difference to the splitting susceptibility of stronger and more brittle concrete, which corresponds with the behaviour of the NWC models. As this test is a closer simulation of the bond behaviour seen in structural systems, De Villiers *et al.* (2017) recommend that the non-conservative BE test σ_d values be used.

In Figure (2.3) the σ_d range $1.59 \sim 1.94$ MPa for the LWFC BE test is lower than for NWC as determined from SANS (2000) and BSI (2004). The design bond stress of a 1200 kg/m^3 ($f_{cu} \approx 12$ MPa) LWFC is unlikely to allow for adequate structural behaviour, as it is below the minimum value prescribed in EN 1992-1: 2004 BSI (2004) (De Villiers *et al.*, 2017).

Basing structural viability on design bond stress, De Villiers (2015) recommends that the mix design 14F in Table (2.1) with target casting density of 1400 kg/m^3 be utilised for further research, as higher density mix ($16F$, recommended density according to Jones and McCarthy (2005)) led to brittle failure, internal cracks and premature bond deterioration, while lower density $12F$ led to a weak material that had inadequate mechanical structural bond resistance (De Villiers, 2015).
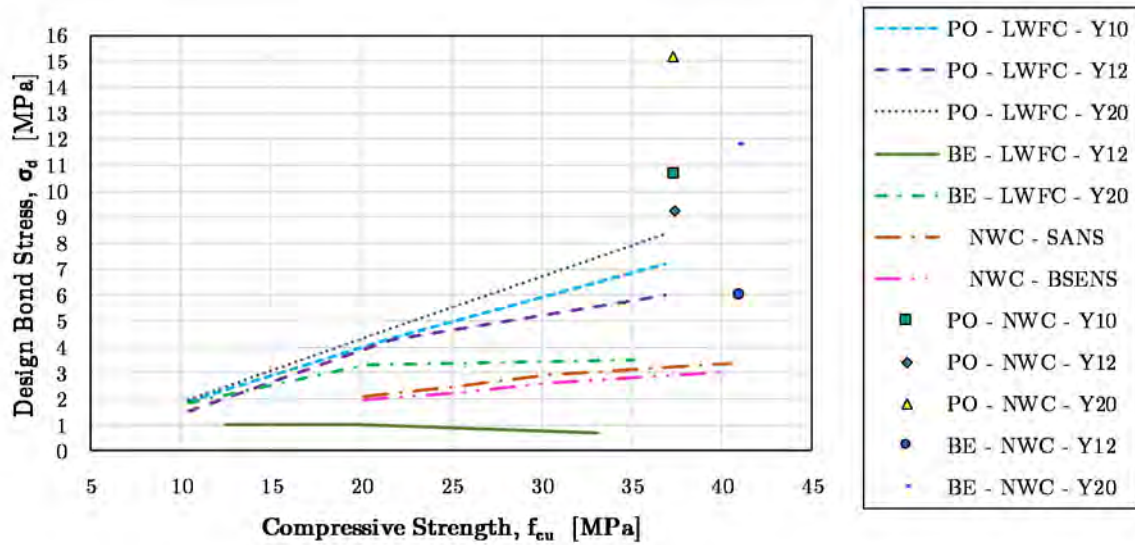
Figure 2.3: *Design bond stress (σ_d) results of De Villiers* et al. *(2017) and NWC equivalents from BSI (2004).*
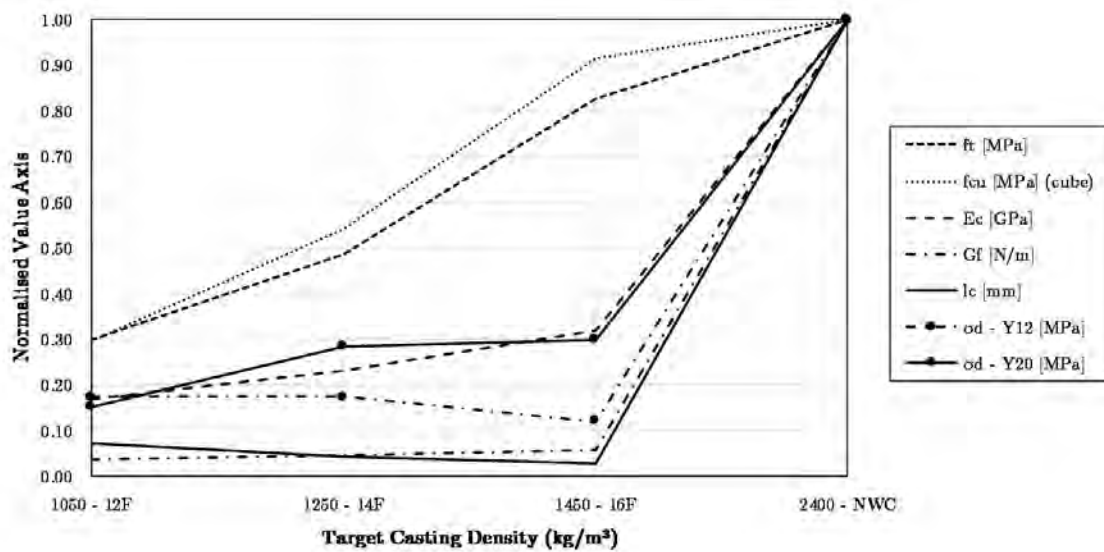
Figure 2.4: *Normalised characteristic test values and design bond stresses for BE tests for Y12 and Y20 rebar as determined by De Villiers* et al. *(2017); showing relative scale of the LWFC test results and shortcomings per mix and material property.*

Reduced E and low fracture energy (G_f) results are cited by De Villiers *et al.* (2017) to be two of the main causes of weak bond in LWFC when compared to NWC. The authors claim further that both E and G_f may control the bond in reinforced LWFC as expressed in characteristic length scale l_c given by Equation (2.11) - referred by Wittmann (2002) as "...a measure of the brittleness of the material...". Normalised characteristic test results in Figure (2.4) give scale to the significantly lower E and G_f of LWFC when compared to NWC. An improvement of bond is now thought to be related to an improvement of the characteristic length of LWFC and in turn an improvement of E and G_f.

$$l_c = \frac{G_f E}{(f_t)^2} \tag{2.11}$$

De Villiers (2015) ultimately concludes that LWFC is not yet fit for structural application and proposes that the following improvements be made:

- Improve the compressive strength of LWFC at lower densities, possibly with lightweight aggregates.

- With reference to the large BE tests conducted: Improve the shear resistance of LWFC with adequate steel detailing.

- Improve the bond capacity by decreasing the brittle behaviour of LWFC at higher densities, possibly with the incorporation of polypropylene fibres to increase the characteristic length l_c.

2.1.7   Fibre Reinforcement

Polypropylene fibres have aided in the production of LWFC. Research regarding these potential benefits is outlined in this section.

Compressive Strength

Kearsley and Mostert (2003) researched the effect of synthetic fibres on the impact resistance and crack formation of LWFC by adding 1.5 kg/m^3 (0.165 %), 3.0 kg/m^3 (0.33 %) and 4.5 kg/m^3 (0.5 %) of 6 mm long chopped polypropylene micro fibres. They established that an increased fibre volume was not sufficient to improve the compressive strength (f_{cu}) or E of LWFC, even though it improved the overall load carrying capacity of the concrete in compression, resulting in improved ductility at higher fibre contents. The fibres were also seen to reduce shrinkage cracks, a positive improvement for durability of LWFC as anticipated by De Villiers *et al.* (2017).

Jones and McCarthy (2005) used longer (19.2 mm) polypropylene fibres at 0.25 % (2.275 kg/m^3) and 0.5 % (4.55 kg/m^3) by mix volume and improved the compressive and flexural strength as well as the Young's modulus of fly-ash inclusive LWFC. This contrasted with the strength reduction observed by Kearsley and Mostert (2003). The largest strength improvement and also the upper optimum dosage for workability was found to be 0.5 % fibres by volume and a 1400 kg/m^3 target plastic density.

Bond

After experiencing increased cracking deformation and deflection in BE testing of LWFC in comparison to NWC it was hypothesised by Jones and McCarthy (2005) that both the addition of fibres or provision of tensile reinforcement in the beam specimens would reduce deflection and possibly allow for the material to be utilised as a structural replacement for NWC (Jones and McCarthy, 2005).

Polypropylene fibres of length 6 mm, 12 mm and 20 mm were used by El Zareef and Schlaich (2008) to improve the tensile strength of LWFC and improve overall reinforcement bond behaviour. It was found that only the longer 20 mm fibres increased the bond stress at the reinforcement interface while all Polypropylene fibres reduced the reinforcement slip at the maximum bond stress. This leads to an improved crack width control - a critical factor for fracture energy (G_f) calculations via the wedge splitting test (Brühwiler and Wittmann (1990)). This work when compared to Kearsley and Mostert (2003) indicates that the fibre length and fibre dosage is critical to improving both the mechanical characteristics, as well as the bond of LWFC.

Strength at Elevated Temperature

Mydin and Soleimanzadeh (2012) researched the effect of Polypropylene fibres on LWFC as well as the variation of flexural resistance of LWFC at normal environmental and elevated ($600°C$) temperatures. A broader sample range and volume percentage addition of fibres were tested. The objective of the study was to examine the pore structure and flexural strength of LWFC with Polypropylene fibre by mix volume ratios of 0.1 %, 0.2 %,0.3 %,0.4 %, 0.45 % and 0.5 % over a range of temperatures to find the optimum fibre content ratio for maximum flexural strength. It was determined by Mydin and Soleimanzadeh (2012) that the addition of up to 0.4 % of Polypropylene fibres enabled the concrete to resist higher temperatures better than plain, control LWFC and was considered the upper optimum dosage.

Tensile Strength/Ductility

Hadipramana *et al.* (2013) studied the effect of Polypropylene fibres in LWFC. Tests were conducted on two LWFC mixes with chopped Polypropylene micro fibres. The fibres were 12 mm in length and 22 μm in diameter and added in 0.25 kg/m^3 (0.0274 %) and 0.33 kg/m^3 (0.036 %) doses. Similarly to Rasheed and Prakash (2016), the target densities were 1400 kg/m^3, 1600 kg/m^3 and 1800 kg/m^3. The compressive and tensile splitting strengths of LWFC were tested beyond 28 days and up to 60 and 90 curing days. At 28 curing days the higher 0.33 kg/m^3 (0.036 %) fibre dosage resulted in a compressive strength (f_{cu}) of 14.8 MPa in comparison to the control LWFC without fibres which had a maximum compressive strength of 6.2 MPa. Interestingly the splitting tensile strength (f_{ct}) had a far lower strength increase with fibre addition from 4.27 MPa to 4.7 MPa. After 90 curing days it was then noted that the compressive strength increased by 12 % and the tensile strength by 28 % which shows a continuation of the cement hydration process in LWFC (Hadipramana *et al.*, 2013). The authors finally concluded that the bond and influence of polypropylene fibre addition in LWFC is similar to that of NWC and that mechanical anchoring of the fibres and bridging forces limited crack propagation.

Fracture Energy

Following the work of De Villiers *et al.* (2017), a comprehensive research project was embarked on at the University of Stellenbosch on behalf of the Technische Universität Dresden to determine the optimum mix design and polypropylene fibre dosage for 1400 kg/m^3 dry density LWFC. The variables in the mixes were: a) sand/cement ratio of 1 or 0 b) fibre length of 12 mm or 24 mm and c) fibre dosage of 0.2 %, 0.35 % and 0.5 % resulting in a comparison of 12 different mixes (Figure (2.5)). The Young's modulus and fracture energy (via both the notched beam three-point-bending (JCI, 2003) and wedge splitting tests (Brühwiler and Wittmann, 1990)) were tested at 28 days while each mix was also tested for its density, compressive and tensile strength at 14 and 28 days. Considering the variation in results, mix 8 (E_c = 8.16 GPa, f_{ct} = 1.76 MPa, f_{cu} = 12.48 MPa, $G_{f,beam}$ = 69.32 N/m and $G_{f,wedge}$ = 18.2 N/m) was selected as optimal, presenting a good balance between comparative strength and workability at this density (Grafe, 2017).
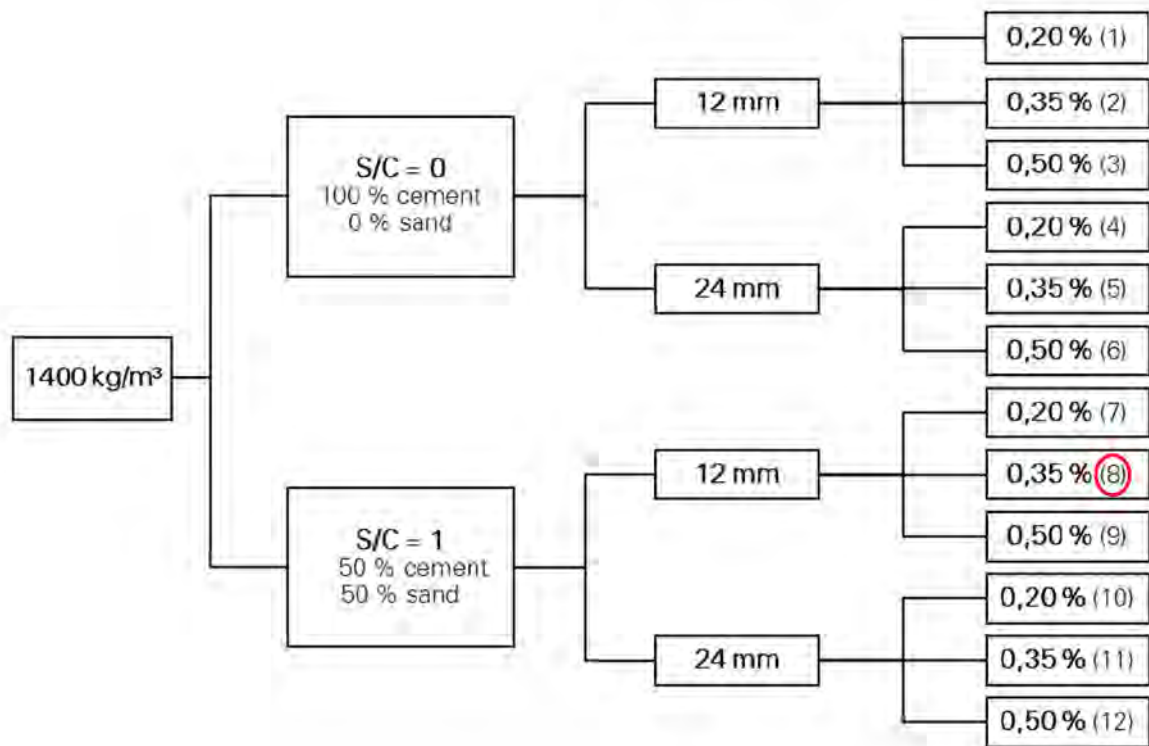
Figure 2.5: *Mix design variation for optimal fibre dosage by Grafe (2017), determined from this selection to be mix 8 in the figure.*

A final conclusion from the work of Grafe (2017) was that the hypothesis of De Villiers *et al.* (2017) has merit and that adding an optimal dosage of Polypropylene fibres does indeed lead to an increase in fracture energy (Van Zijl *et al.*, 2017).

2.1.8   Fracture Energy

It was determined by De Villiers (2015) that the low fracture energy may be responsible for the poor bond strength of conventional steel reinforcement with LWFC. The reason for this conclusion was the low fracture energy value measured by De Villiers *et al.* (2017) which had a substantial influence on the characteristic length (l_c) of the material

Hillerborg *et al.* (1976) developed the characteristic length as a material property indicator of ductility where low length values indicate brittle concrete behaviour. The brittle LWFC l_c value of 10.93 mm determined by De Villiers *et al.* (2017) is in stark contrast to the 1300 mm length calculated for NWC by Wittmann (2002) in Table (2.1).

Kozlowski *et al.* (2015) determined the fracture energy and mechanical properties of notched and un-notched LWFC beam specimens of varying densities via three-point-bending tests. The mix design differed from those of De Villiers *et al.* (2017) as it did not contain fly-ash and fibres - a recommended improvement. Nevertheless, fracture energy and tensile strength f_t were reported to increase with an increase in density. Their highest density LWFC tested (1024 kg/m^3) is the closest to 1050 kg/m^3 dry density mix 12F of De Villiers *et al.* (2017) and resulted in G_f of 4.94 N/m at a compressive strength of 5.9 MPa, similar to the results shown in Table (2.1).

The study by Grafe (2017) at Stellenbosch University for the optimal fibre dosage made use of the hypothesis of De Villiers *et al.* (2017) that an improvement of fracture energy is required for adequate structural mechanical bond of reinforcement in LWFC. Fracture energy of the 12 mix designs in Figure (2.5) was tested via both the notched beam three-point-bending (JCI, 2003) and wedge splitting tests (Brühwiler and Wittmann, 1990). A large discrepancy between the two test methods on the same mix was seen where for the optimal Mix 8 (Figure (2.5)) $G_{f,beam} = 69.32$ N/m was significantly larger than $G_{f,wedge} = 18.2$ N/m. This increase could be attributed to the difference in tensile force application method between $G_{f,beam}$ and $G_{f,wedge}$.

2.2 Seismicity in South Africa

South Africa is susceptible to moderate earthquakes with a peak ground acceleration (a_g) of $0.15 \cdot g$ where gravitational acceleration $g = 9.81 m/s^2$ in the South Western portion of the Western Cape province in South Africa, in particular Cape Town and its surrounding metropolitan area (SANS 10160-4:2017,(SANS, 2017)). The seismic hazard map in Figure (2.6) indicates this distribution and also distinguishes between these intra-plate fault originating earthquakes and the mining induced seismic action in the Central and North-Eastern regions of South Africa (Singh *et al.*, 2009).

The first South African Seismic Code in 1989 (SANS 10160-4:1989) instituted rules for seismic design. All buildings constructed after this code was introduced were expected to be designed for at most a peak ground acceleration of $0.1 \cdot g$ m/s^2. The maximum value, a slight reduction of the $0.15 \cdot g$ m/s^2 in Figure (2.6), has since been a required design load. This maximum value is prescribed for the South Western Cape of South Africa and is noted in the current South African Seismic Code (SANS 10160-4:2017, (SANS, 2017)) (Retief and Dunaiski, 2009).

For the work of this thesis and the aim to construct reinforced LWFC buildings in South Africa, a seismically sufficient design will be required that complies with SANS 10160-4:2017 (SANS, 2017) where the vertical distribution of seismic load over the height of a building through the equivalent static lateral force procedure is accounted for (Retief and Dunaiski, 2009).
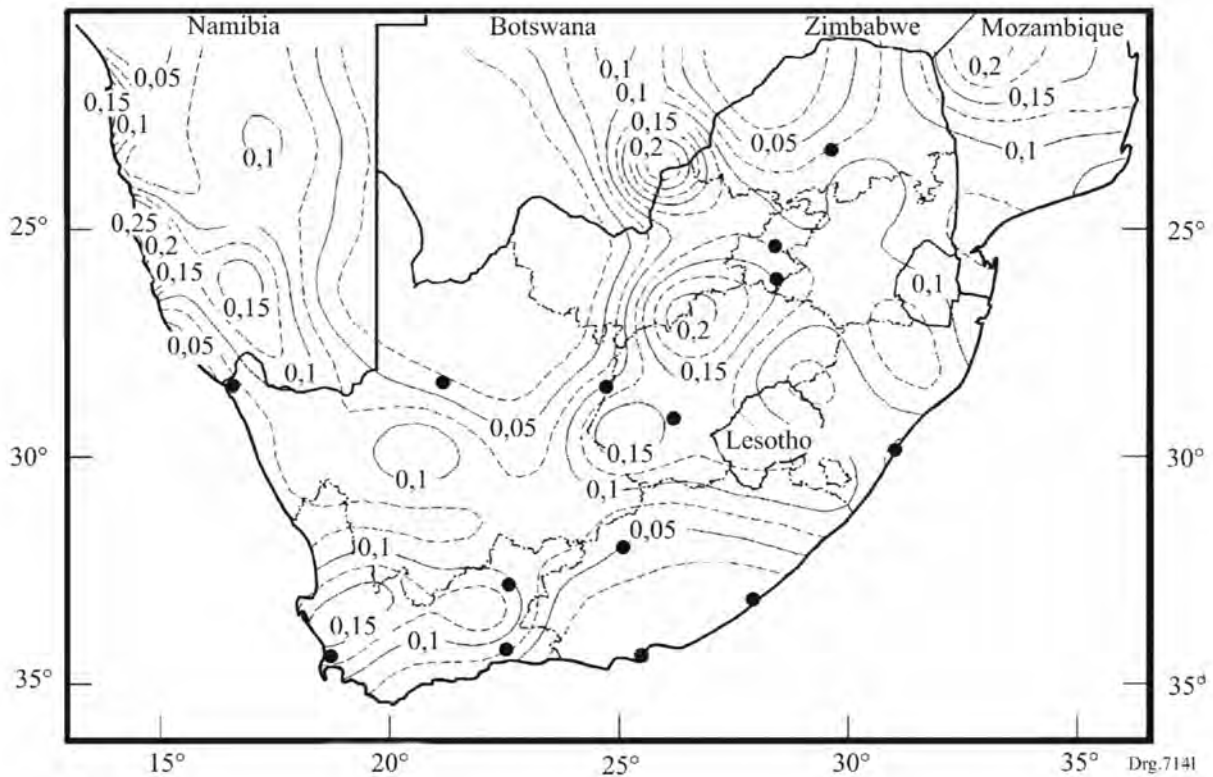
Figure 2.6: *Seismic hazard zones of South Africa,* 10 % *exceedance in 50 years, nominal peak ground acceleration* (a_g)*, taken from SANS 10160-4:2017 (SANS, 2017).*

2.3   Precast Concrete

Reduction in construction time, on site labour and high level quality control are three of the advantages of precast concrete construction, in contrast to on-site, cast-in-situ construction where complete concrete elements are made in factories and transported to building sites for assembly. Precast construction has been increasingly used by designers but only codified more formally in the 1990's (Park, 1995; Bull *et al.*, 1999).

2.3.1   Precast Concrete Under Seismic Loads

The challenge for seismic design of precast structures either by moment resisting frames or structural, jointed wall systems is finding cost-effective and practically efficient means of "...connecting the precast elements together to ensure adequate stiffness, strength, ductility and stability" (Park, 1995).

Seismic loads can contrast greatly to conventional design loads, which generally are far larger and affect the whole structure. Initial capacity design made use of linear-elastic structural analysis to determine design forces on concrete elements, with the plan to design the members to be "strong enough" to resist these forces. The problem with this method was however that the post-elastic behaviour was unknown and a "matter of chance" as failure could occur at any point in the structure where the shear force or flexural capacity was exceeded, leading to calamitous collapse of the building (Park, 2002).

Considering this, the design seismic force is related to the achievable structural ductility factor, μ_{duct} Formula (2.12). Δ_{max} is defined as the peak horizontal displacement that can be applied on a structure during multiple seismic load cycles without significant loss of

strength. Δ_y is defined as the horizontal displacement at "first yield" assuming elastic behaviour of the cracked structure (Park, 2002). According to NZS (1995) and Park (2002), precast structures are either designed as "limited-ductility" or as elastically responding structures requiring ductility factors of $2 \leq \mu_{duct} \leq 3$ or $\mu_{duct} = 1.25$ respectively.

$$\mu_{duct} = \frac{\Delta_{max}}{\Delta_y} \tag{2.12}$$

The rational seismic design approach is to choose the most appropriate mechanism for post-elastic deformation and then design the structure so as to ensure that yielding will only occur in this manner during a major earthquake (Park, 1995). This ductility approach can be expanded for the use of precast elements where likely brittle connections can be improved to remain elastic during a major seismic event (Park, 1995).

2.3.2 Precast Concrete Connections

Precast concrete structural wall construction is usually categorised by the type of connection between the individual elements as either a "jointed" or a "monolithic" wall system. Monolithic systems make use of "strong" connections where the elastic limit of the connections is not exceeded while "jointed" connections are designed as ductile where energy is dissipated at the connection and contributes to the building's global ductility (Bull *et al.*, 1999). Monolithic precast structural wall systems are designed in the same way as cast-in-place concrete construction (Park, 1995).

According to Sauter (1984) there are three types of connections between precast concrete elements. "Dry" connections make use of embedded steel members, anchored and either bolted or welded together on-site. Post-tensioning of precast elements with tendons crossing joints have also been successfully employed. The most popular type of connections however are "wet" joints, poured in-situ with dowels and reinforcement. These wet, cast-in-place or monolithic connections are preferred.

"Jointed-wall" connections can be further separated into where the connections take place and what portion of the structure they join. These two connections can be seen in Figure (2.7) where horizontal connections connect the "top and bottom" of panels and vertical connections bridge the "left and right" (Bull *et al.*, 1999). The reader is directed to Seifi *et al.* (2016) for a recent compilation of various jointed connections in current buildings in New Zealand following a review of precast concrete connections after the Canterbury 2010/2011 earthquakes. Jointed-wall construction through "tilt-up" manufacturing of concrete walls has become popular for low-rise office blocks and apartment buildings where entire wall panels are cast alongside the floor slab of the structure and lifted by cranes after gaining sufficient strength for manoeuvrability. Thereafter the walls are connected to surrounding structural elements via various connection methods such as bolted or welded steel plates as well as angle brackets or lapped reinforcement splices (Park, 1995).

The research of Pall *et al.* (1980) gives a good understanding of one type of jointed-wall connection and how ductility is added. The successful development of Limited-Slip-Bolted (LSB) connections (Figure 2.8) which do not move under serviceability conditions but have capacity for movement under seismic load. They argue that the overall energy dissipating capability of the structure is key to the successful implementation of a precast concrete building with mechanical connections (Pall *et al.*, 1980).
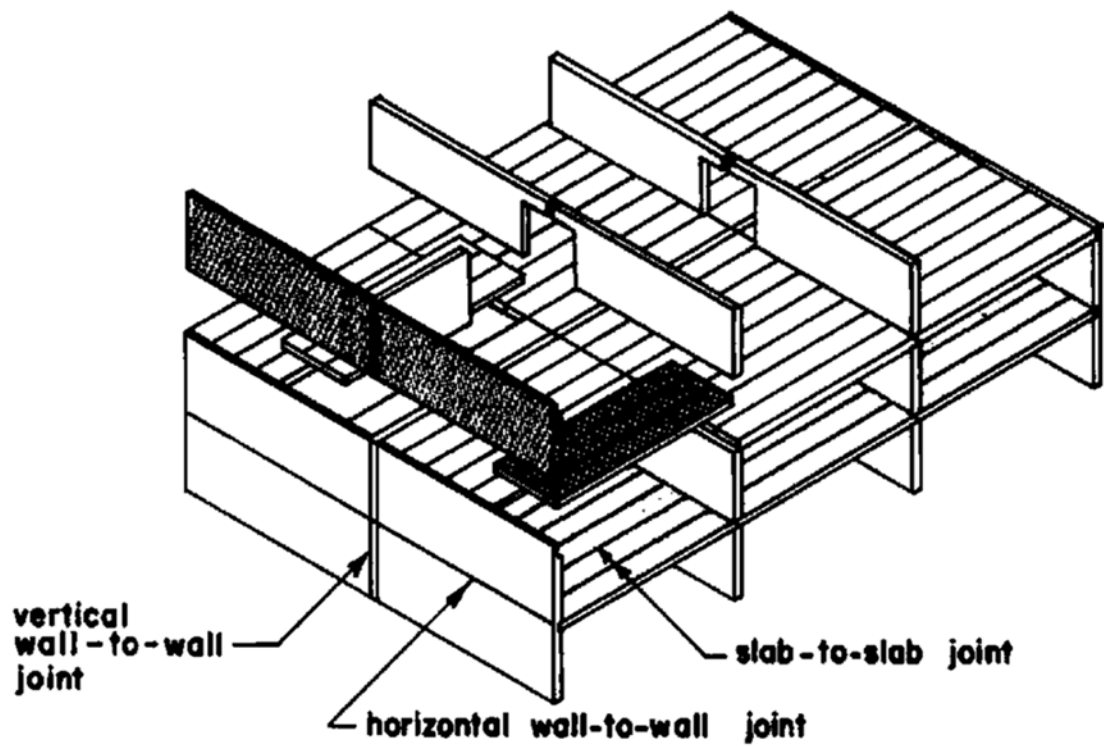
Figure 2.7: *Types of joints in large panel buildings: Vertical and horizontal connections (Pall et al., 1980)*
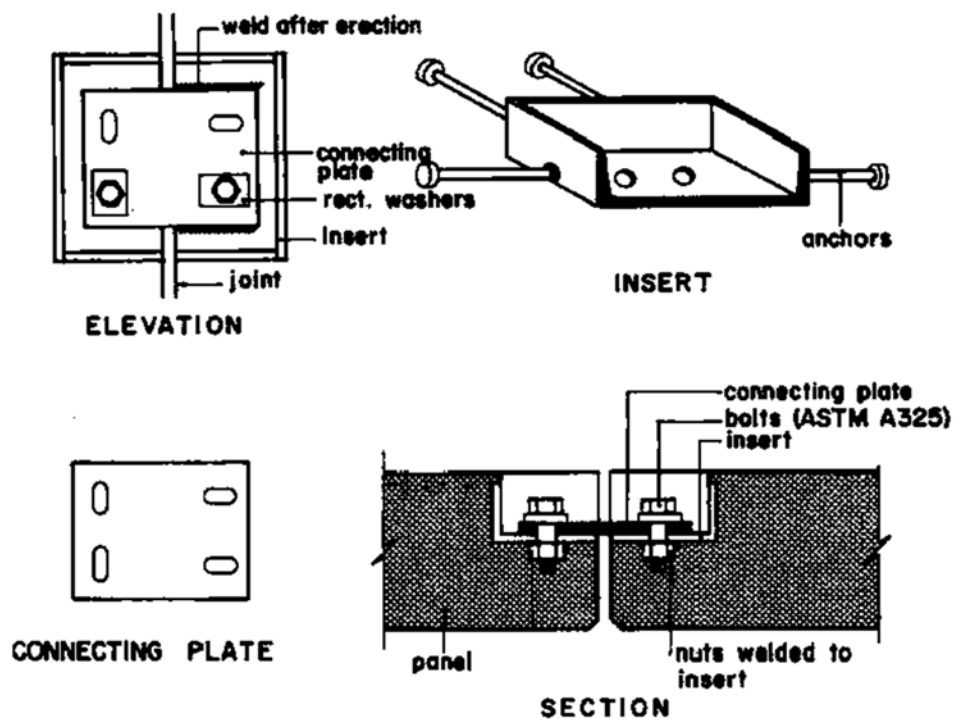
Figure 2.8: *Typical details of LSB bolted connections: Simple wall-wall joint (Pall et al., 1980)*

The overall energy dissipating ability of a structure is difficult to quantify and compare with the stringent ductility requirements of current seismic codes. Connections between precast panels therefore need to be placed and designed so as to maximise their potential for energy dissipation while ensuring that they are of adequate strength (Pall *et al.*, 1980).

Bull *et al.* (1999) §4.7.2 acknowledges in conclusion that "...a very cautious approach be taken to the design of jointed panel precast system" and in the case of the New Zealand seismic code (NZS (1995)), the response of jointed panel construction contrasts greatly to the basis of the code and will require a design procedure based upon experimental test data as well as a detailed theoretical analysis.

2.3.3 Precast Concrete Connection Testing

Test methods for precast concrete connections under seismic load are prescribed according to Negro and Toniolo (2012) "Annex A - Protocol for connection testing". Initially, monotonic loading (push-over) test force-displacement diagrams are used to assess the ductility of the connection and determine the loading parameters of subsequent cyclic testing. Thereafter the cyclic response is obtained through application of the load history in Figure (2.10).
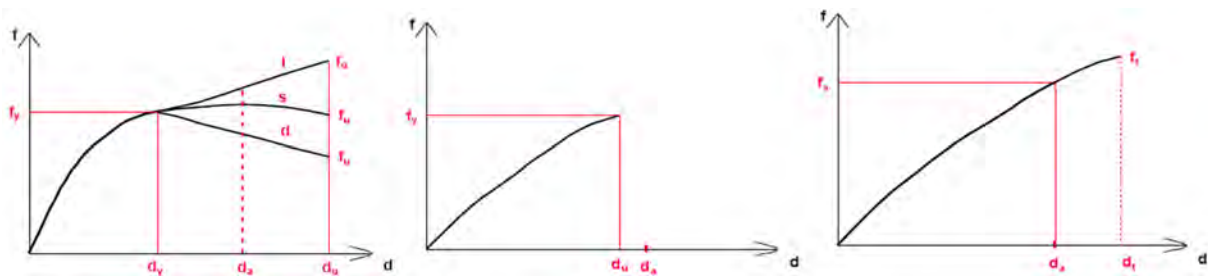
Figure 2.9: *Monotonic force-displacement diagrams for varying connection behaviour* **Left:** *Ductile,* **Centre:** *Brittle and* **Right:** *Over-resisting (Negro and Toniolo, 2012)*
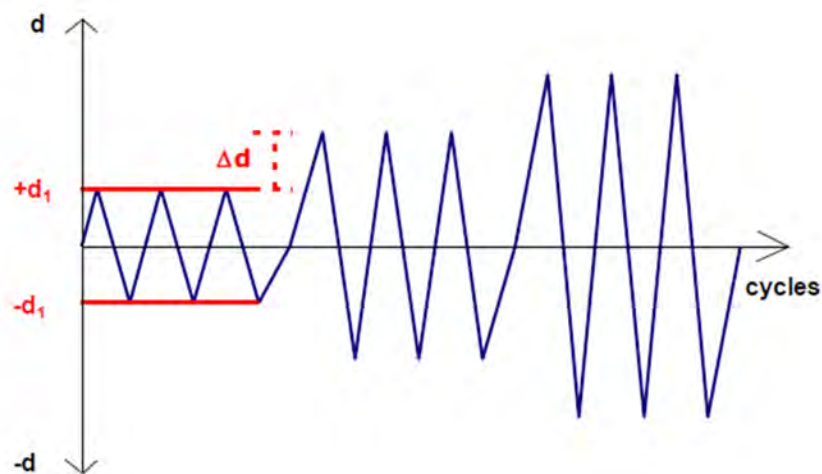
Figure 2.10: *Cyclic displacement history diagram (Negro and Toniolo, 2012)*

In Figure (2.10) "groups of three cycles of the same amplitude are performed step-wise until failure with successive amplitude incremental increases Δd equal to d_1, obtained

from the monotonic loading test results as the lessor displacement limit of d_y (Yielding), d_a (Allowable serviceability), d_t (Test limit) or d_u (Ultimate)" in Figure (2.10). From the cyclic tests one is able to determine the energy dissipation of the connection. The reader is directed to Negro and Toniolo (2012) Annex A for the detailed, stepwise energy dissipation calculation procedure.

2.3.4 Precast Concrete Walls

It is understood that concrete walls are useful lateral force resisting elements due to their deflection limiting, high stiffness and overall retaining of structural integrity of a building after heavy winds or earthquakes. It is also understood that cast-in-place walls generally provide the best earthquake resistant structural system (Bull *et al.*, 1999).

Advancements in efficient precast walling by Crisafulli *et al.* (2002) indicate that lightly reinforced precast concrete wall panels can provide sufficient resistance against lateral forces in low-rise buildings. The design details claim that multiple wall panels can provide adequate seismic resistance if designed for nominal elastic or limited ductility response where the seismic forces are approximately double the forces of fully ductile design Park (1995).
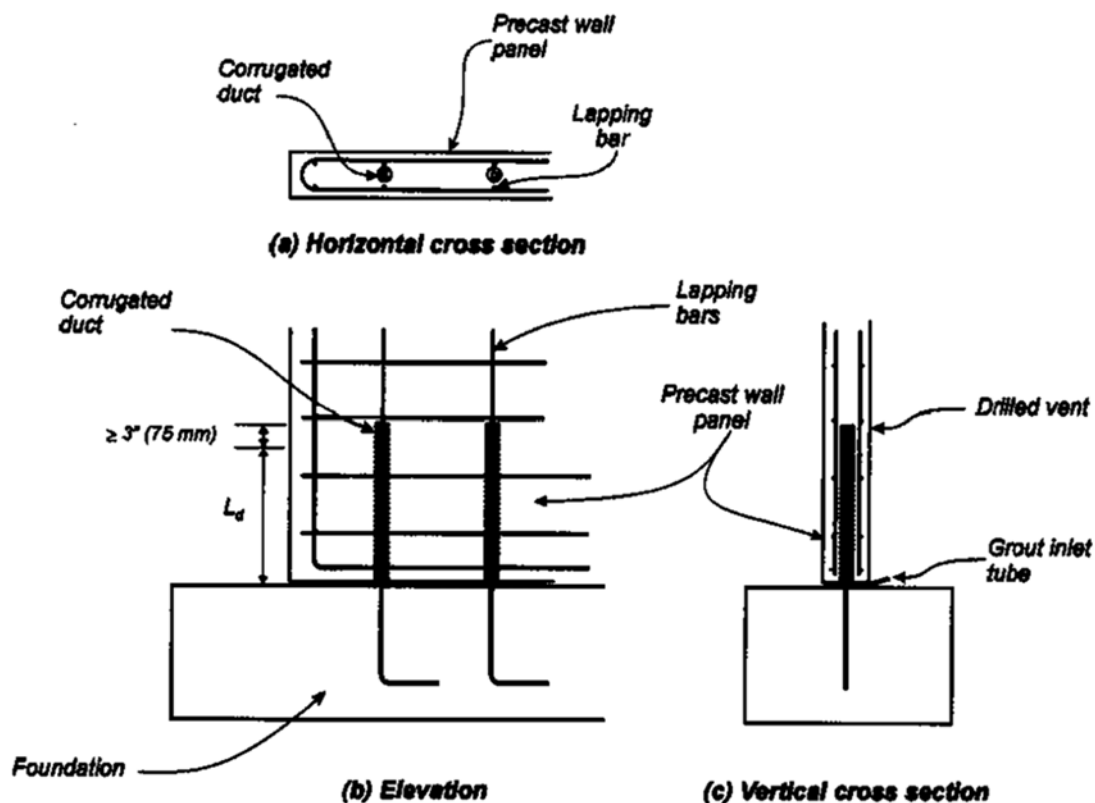
Figure 2.11: *Lightly reinforced wall panel to foundation connection detail proposed by (Crisafulli* et al.*, 2002)*

In this system proposed by Crisafulli *et al.* (2002) the precast concrete wall panels are grouted into the precast wall panel that is lowered on top of it and anchored in corrugated steel ducts with adequate anchorage (Figure (2.11)). The system is lightly reinforced with less reinforcement across the grouted connection than longitudinal reinforcement within

the panel. Through this design a limited ductility response is ensured as the flexural strength of the wall-foundation beam connection is less than the cracking moment of the wall panel itself. Hence the plasticity is localised at the connection, unable to spread through and damage the wall panel (Crisafulli *et al.*, 2002).

This useful property of connections failing before global panel failure was identified by Pall *et al.* (1980) who refer to panellised and jointed structures that withstood earthquakes in the then Soviet Union, Cuba, Romania and Japan. In these cases the brick and concrete framed buildings sustained considerable damage while the panellised structures developed minor cracks at their connections.

Chapter 3

Global Experimental Design

This chapter explains the experimental design for the thesis. The concrete mix designs for both LWFC and NWC are initially explained. Details of the Physical Scale Test(s) (PST) are summarised according to the connections, applied load, laboratory setup and tested wall specimens. Thereafter, the material characterisation tests for compressive strength and Young's modulus are detailed in the last section.

3.1 Concrete Mix Design

3.1.1 Lightweight Foamed Concrete

The lightweight foamed concrete used in this study comprised of four main ingredients: namely water, cement, fly-ash and polypropylene fibres. The mix design used is reliant on the work of Kearsley and Mostert (2005) who based their design of LWFC on a target plastic density, through which they obtained the water/cement and sand/cement ratios. Their work is summarised by Equations (3.1) and (3.2) for the mix design while Equation (3.3) gives a useful estimate of target casting density required for a desired dry density. Unfortunately Equation (3.3) is not directly applicable to the mix design used for this work due to the limited dry densities from which it has been derived. It nevertheless does provide a useful estimate of a required target casting density, $\rho_{dry} = 1600$ for $\rho_{dry} \approx 1449 [kg/m^3]$, recommended by Jones and McCarthy (2005) as a optimal density for structural LWFC.

The ribbon mortar mixer used in this study can be seen in Figure (3.1). This mixer was chosen for its mixing action of "folding" the foam into the base mix with minimal damage to the foam.

To calculate the mix design quantities Equations (3.1) and (3.2) are solved simultaneously. Mix volumes used for this study can be seen in Table (3.2) while relevant mix design ratios and densities for LWFC are shown in Table (3.3). The base density ρ_b is the density of the wet and dry ingredients before foam addition.

$$\rho_t = x_c + x_c \left(\frac{w}{c}\right) + x_c \left(\frac{a}{c}\right) + x_c \left(\frac{s}{c}\right) + x_c \left(\frac{a}{c}\right)\left(\frac{w}{a}\right) + x_c \left(\frac{s}{c}\right)\left(\frac{w}{s}\right) + RD_f \cdot V_f \quad (3.1)$$

$$1000 = \frac{x_c}{RD_c} + x_c\left(\frac{w}{c}\right) + \frac{x_c\left(\frac{a}{c}\right)}{RD_a} + \frac{x_c\left(\frac{s}{c}\right)}{RD_s} + x_c\left(\frac{a}{c}\right)\left(\frac{w}{a}\right) + x_c\left(\frac{s}{c}\right)\left(\frac{w}{s}\right) + V_f \quad (3.2)$$

Where:

ρ_t is the design target plastic density $[kg/m^3]$
x_c is the cement content $[kg/m^3]$
$\frac{w}{c}$ is the water/cement ratio
$\frac{a}{c}$ is the ash/cement ratio
$\frac{s}{c}$ is the sand/cement ratio
$\frac{w}{a}$ is the water/ash ratio
$\frac{w}{s}$ is the water/sand ratio
V_f is the foam volume $[l]$
RD_f is the relative density of foam
RD_c is the relative density of cement
RD_a is the relative density of ash
RD_s is the relative density of sand

$$\rho_t = 1.034 \cdot \rho_{dry} + 101.96 \quad (3.3)$$

Where:

ρ_{dry} is the cured dry density $[kg/m^3]$

Figure 3.1: *Dry ingredients in 70 L paddle mortar mixer*

Cement

The cement used was South African manufactured Pretoria Portland Cement, (PPC) OPC 52.5N CEM II portland cement (PPC (2017)) conforming to SANS 50197-1:2013 (SANS (2013)).

Fly-ash

Based on the advantages mentioned in Section (2.1.3) the use of fly-ash was considered a requirement for structural LWFC. The fly-ash used in this study was a single batch of Ulula Class-S fly-ash (Ulula Ash (Pty)Ltd (2016)) classified according to SANS 50450-1:2014 SANS (2014). Understanding the work of Kearsley and Mostert (2005) and their conclusion of a 75 % optimum ash replacement as well as other reinforced concrete durability concerns, a decision was taken to use a 2 : 1 fly-ash replacement of cement; double the ratio used by De Villiers *et al.* (2017).

Polypropylene fibres

As per the recommendation of Jones and McCarthy (2005) and in contrast to the work performed by De Villiers *et al.* (2017), SAPY Corehfil^{TM} polypropylene fibres were added to the LWFC mix. The aim of this was to reduce micro cracks and improve the tensile behaviour of LWFC. The fibres of Table (3.1) were added in accordance with the findings of Grafe (2017) at a dosage of 0.45% by volume to the mix. This fibre volume was conservatively higher than the optimum 0.35% fibre dosage of the same fibres chosen by Grafe (2017). This dosage was chosen to increase LWFC strength and durability in line with current research at Stellenbosch University.

Table 3.1: *SAPY Corehfil^{TM} polypropylene fibre properties (SAPY (2016))*

Properties	SAPY Corehfil ^{TM} Polypropylene fibres
Density $[kg/m^3]$	910
Melting Point $[°C]$	160
Fibre Diameter [µm]	40
Fibre length $[mm]$	12
Fibre colour	Natural (White)

3.1.2   Normal Weight Concrete

The NWC panels for this research followed on the work and testing method of De Beer (2016). The same high-strength NWC concrete mix design was therefore chosen for these panels. The mix design is indicated alongside the LWFC mix quantities in 3.2. This self-compacting concrete mix required a superplasticizer for adequate flowability. MAPEI Dynamon SP1 superplasticizer was added to the dry ingredients soon after the water was added. It was added up to a maximum of 0.8 % mix volume depending on flowability until a 600 *mm* slump-flow was achieved.

Table 3.2: *Mix volumes utilised for this study detailing both LWFC and NWC for ground and floor-slab panels per cubic metre.*

Concrete:	LWFC	NWC
Target Casting Density $[kg/m^3]$	1600	2400
Base Mix Density $[kg/m^3]$	1705	N/A
CEM II-52.5 $[kg]$	371.8	378
Fly-ash, Class S $[kg]$	743.7	122.5
Coarse aggregate $6-9\ mm$ $[kg]$	0	769.5
Polypropylene Fibre $[kg]$	4.095	0
Sand $[kg]$	0	972
Water $[Litre]$	479.7	180
Foam $[kg]$	4.819	N/A
Super Plasticiser $[kg]$	0	7.56

Table 3.3: *Mix design ratios utilised for LWFC production in this study according to Kearsley and Mostert (2005)*

Relative density of the cement (RD_c)	3.15
Relative density of the ash (RD_a)	2.2
Density of the fibre (RD_{fibre}) $[kg/m3]$	910
Relative density of the foam (RD_f)	0.075
ash/cement ratio $(\frac{a}{c})$	2.0
water/cement ratio $(\frac{w}{c})$	0.43
water/ash ratio $(\frac{w}{a})$	0.43
effective water/cement ratio $(\frac{w_{eff}}{a})$	1.29

3.2   Physical Scale Tests

3.2.1   Design Basis

The underlying basis of the experiments to follow rely on a proposed design for a LWFC structure or pilot building. The basic structure detailed geometrically in Figures (3.2) and (3.3) was drafted by a local engineer and businessman with an interest in LWFC construction. The design is part of a project proposal and has not yet been tested or built, but serves as the starting point for this investigation.

For this investigation the $7.2m$ long wall panels of Figure (3.2) are constructed out of two $3.6m$ connected precast LWFC wall panels. The vertical connections are designed to be mechanically bolted while the horizontal connections are dowel connected with low shrinkage grout; recommended as common pre-cast concrete connection practice by Seifi *et al.* (2016) and shown in Figure (2.11). These load bearing LWFC walls surround the structure and are the author's structural system.
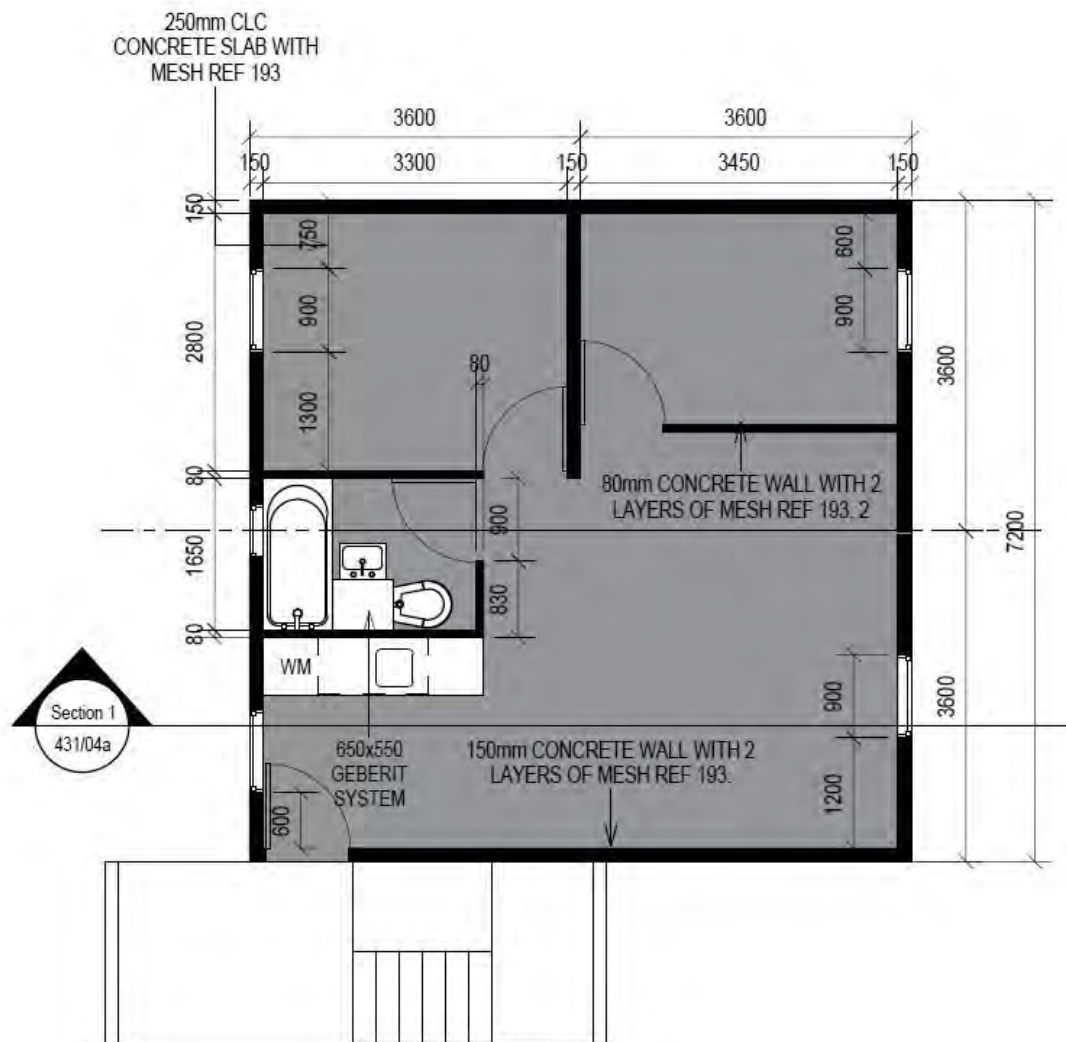
Figure 3.2: *Pilot building floor plan showing layout of major walls for the second floor*

The method of precast construction is aimed to be employed as it is believed that the controlled factory production will guarantee that the material property benefits of LWFC are realised. Additionally, precast LWFC walling will result in efficient time saving and ultimately a favourable cost comparison. In this system high quality full-scale wall panels are transported to site and erected on top of an in-situ cast and cured NWC ground-floor slab, complete with protruding dowel anchors and embedded ducts in the LWFC panels. Before placing the wall panels the slab perimeter is levelled with a standard mortar and dampcourse layer. Thereafter the panels are placed and grouted on the protruding rebar and subsequently mechanically connected to one another at their vertical connections.

This process is a LWFC adaptation of the lightly reinforced NWC precast wall panel system suggested by Crisafulli *et al.* (2002) (Section (2.3.4)), altered slightly to include the mechanical or jointed vertical connections. Soon after placing and connecting the walls to the floor slab, precast hollow-core floor panels are spanned between the recently erected LWFC walls to form the first floor. These floor panels will be connected to the top of the wall panels via a reinforced and grouted monolithic connection for seismic performance, however this detailed design is out of the thesis scope and the reader is directed to Fenwick

et al. (2010) and Jensen *et al.* (2007) for further information. This design is repeated for floor two and the roof slab of Figure (3.3).

Full structural detailing of the wall panels is completed in the factory where electrical ducting and reinforcement steel are fixed alongside water pipes to coincide with the global structural design. The aim of this construction method is to allow the contractor to construct multiple low-rise residential units simultaneously where alternative wall and floor panel sets are placed and grouted together. Apart from the time-benefit of precast construction further anticipated cost reductions are lower on-site labour costs where now unskilled workers are up-skilled as they form part of the controlled manufacturing process in factories.
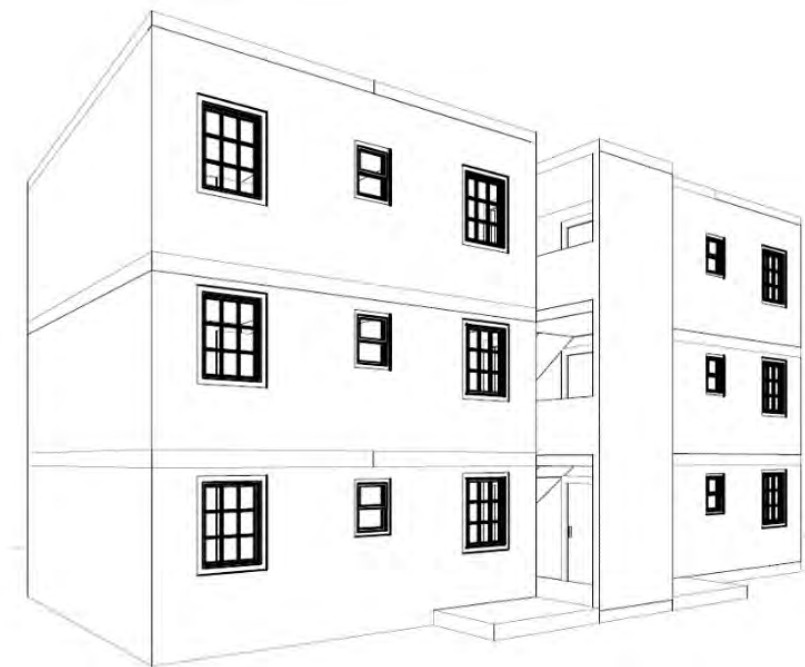
Figure 3.3: *Precast LWFC building concept and perspective view*

For this study the implications of a laboratory test environment limited the scale of the wall, and resulted in an approximately 1 : 3 scale wall being constructed. The dimensions of the walls and NWC panels can be seen in Appendix (B). A ground floor wall is selected with the highest vertical self-weight load of the low-rise building above; further explained in Section (3.2.3). Two mesh Ref.193 reinforcement layers were prescribed by the engineer for the LWFC panels in the proposed building design and have been included in the scale tests.

3.2.2 Connection Design

The precast wall designed in this research can be seen during assembly in Figure (3.4) where the two walls are placed between NWC panels. The vertical connection between the two wall panels and horizontal connections between the LWFC wall panels and the NWC floor panels are detailed in this section.
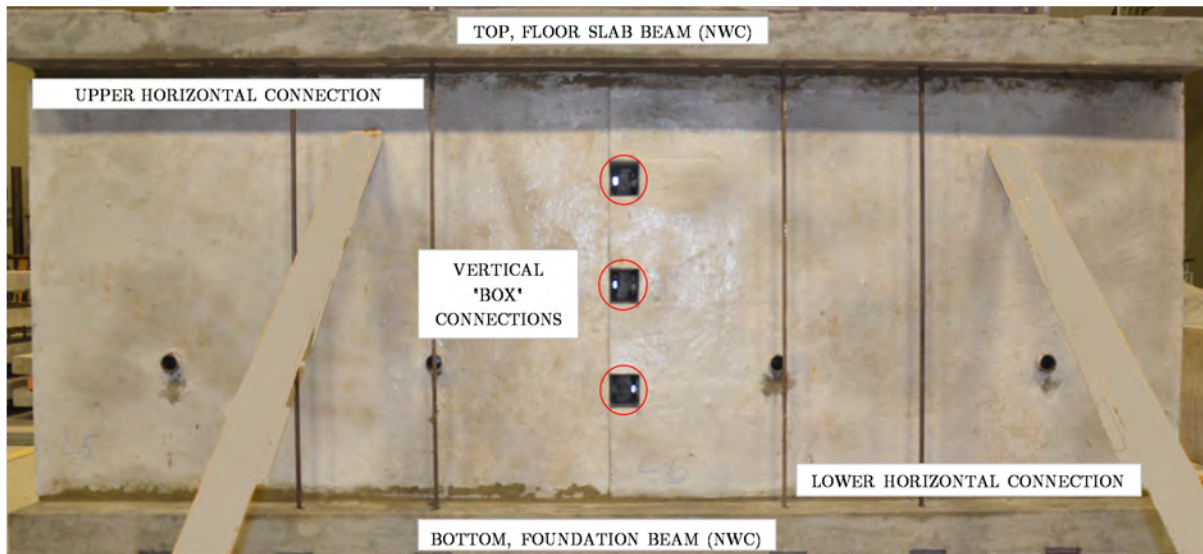
Figure 3.4: *Assembled walls showing vertical "box" and horizontal "dowel" connections*

Vertical Connection

A jointed connection was chosen for the vertical connection of the two LWFC panels as it was believed by the author that this would be a practical solution for precast assembly. Ultimately the design of the connection and its placement at the centre of the wall panels is to develop a connection that can create a completely flush connection between the two panels. This to ensure that maximum frictional resistance between the panels is achieved without adding any eccentricity at the connection.

Interested in the structural use of LWFC, Cape Town based precast concrete contractor Cape Concrete Works (CCW) (CCW (2017)) have already built LWFC trial buildings utilising a construction method similar to the one proposed in this thesis. They have developed a mechanical connection box made from welded steel plate, $M16$ bolts and lifting anchors connected to embedded reinforcement. The vertical connections between wall panels in this thesis were based on this design. Figure (3.5) shows the connection box with lifting anchors placed horizontally and bolted to the steel connection box. The exact dimensions of the connection box can be seen in Appendix (A).

The box is designed to be placed into a recess created in the precast panel where the lifting anchor is embedded. After placing the box in the recess (See Figure (3.7)), the adjoining panels are fastened together with bolts. The two sides of the box are slotted to allow for slight adjustment where the anchors embedded in the panel are not perfectly aligned. Figure (3.6) shows the box in place in one half of the vertical wall before connecting.
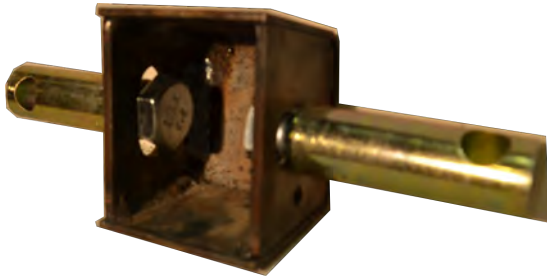
Figure 3.5: *Vertical connection box showing attached lifting anchors embedded in concrete*

Figure 3.6: *Vertical connection box showing slotted holes for adjustment and unfastened M16 bolt*

Figure 3.7: *Connection box in moulded recess of LWFC panel, showing place for two additional connection boxes as well as embedded lifting anchors on this* 1 : 3 *scale wall*

Horizontal Connection

A monolithic connection was chosen for the horizontal connection between the foundation ground-slab and LWFC wall panels, symmetrically mirrored for the floor-slab connection. The rationale behind this design was replicating the horizontal connection design of Crisafulli *et al.* (2002) in a laboratory environment where a symmetrical connection (with grouted rebar facing opposite directions) simplifies concrete form-work. Two NWC panels were required to provide rigid connections to the 500 *mm* thick reinforced concrete (RC) laboratory strong floor, as if the wall was being tested on site and grout connected to a large ground-slab below and hollow core floor-slab above. The layout and spacing of the connecting bolts were both dictated by shear force application on the LWFC panels as well as the available structural steel H254x254x89 beams through which the forces were applied (Figure 3.8).

Two high-strength NWC panels were cast for this purpose and can be seen in Figure (3.9). Each panel was cast with 10 voids for connection and lifting points, 8 Class 8.8 bolts for shear transfer and 6 grout ducts through the panel for grouted rebar connection of 3 per LWFC panel. The reinforcement steel (rebar) can be seen in Figure (3.11) while the grouting process is shown in Figure (3.10), a portion of the panel in Figure (3.4). The reinforcement layout of the NWC panel can be seen in Figure (3.12) where both flexural steel (required for manoeuvring the panel alone) and shear rebar surrounding the cast
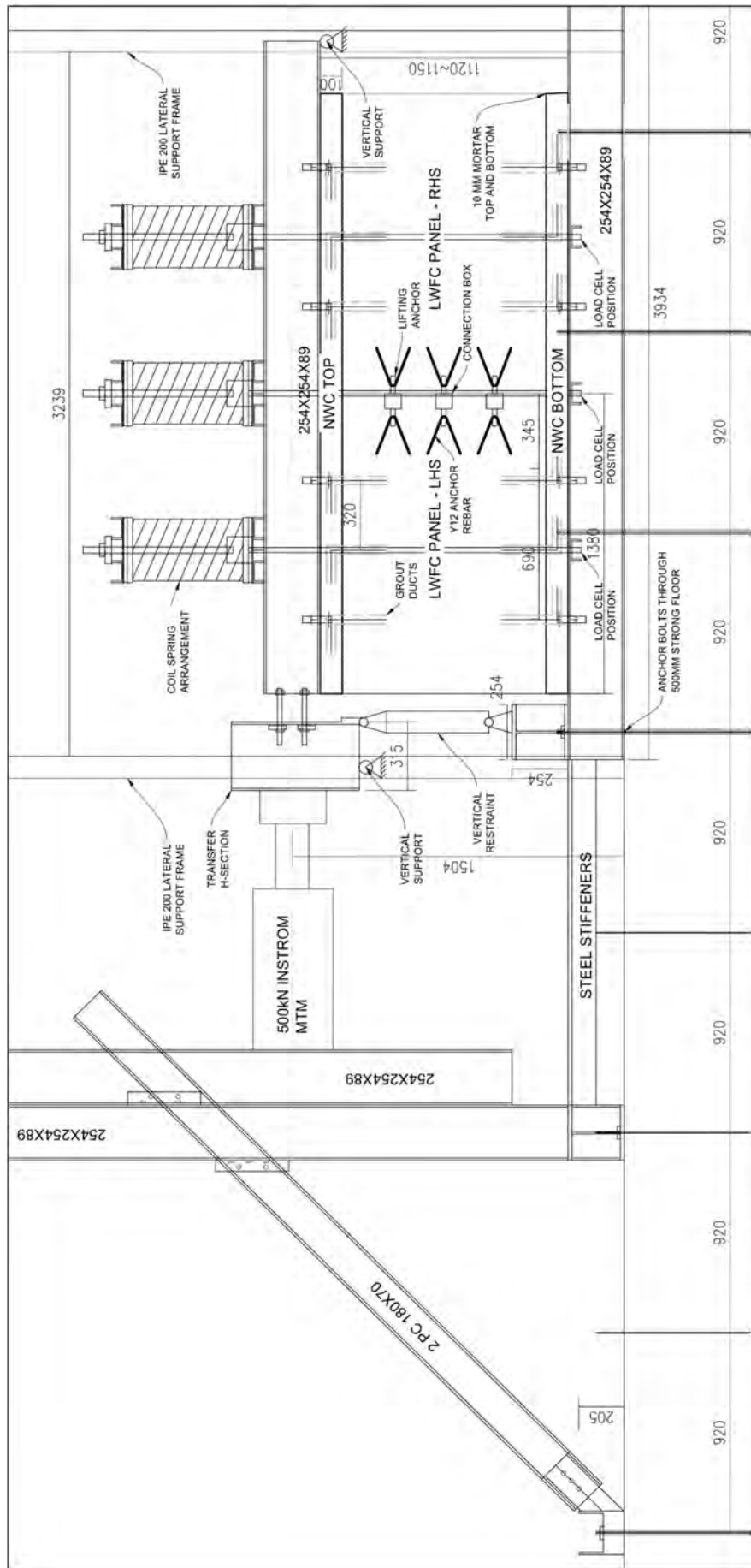
Figure 3.8: *Physical scale test laboratory setup drawing (Units in millimetres).*

voids has been placed. The design of these NWC panels is a expansion on the work of De Beer (2016).

Grouting of the lower connection between the "ground-slab" lower NWC panel and LWFC panels was performed by pouring SikaGrout® 212 (Sika (2016)) through a partially filled 40 *mm* pipe, the same pipe used for the grout ducts. It was essential that the grout was sloppy, yet within the water specifications (Sika (2016)) to make sure that it flowed easily and did not block the tube which could trap air and result in inadequate bond of the grout and reinforcement. This grouting method can be seen in Figure (3.13). Grouting of the upper connection between LWFC panels and "floor-slab" was considerably simpler and required a slightly less watery grout. It was again important to make sure that no air voids were trapped in the tube; the method can be seen in Figure (3.10).

Due to the shear dominant lateral testing performed (outlined in Section (2.3.3)) it was decided that corrugated grout ducts which were unobtainable could be substituted with conventional 40 *mm* drainage pipe. This white pipe in Figure (3.14) which would behave similarly to the corrugated ducts in shear but would have reduced tensile stiffness due to a drastically reduced bond to the concrete within which it was cast. It was believed that this reduced tensile resistance would not be exposed in the laboratory test configuration (Figure (3.8)). It is however still advised by the authors that corrugated grout ducts of Crisafulli *et al.* (2002) and Seifi *et al.* (2016) are used for general construction using this proposed structural system.
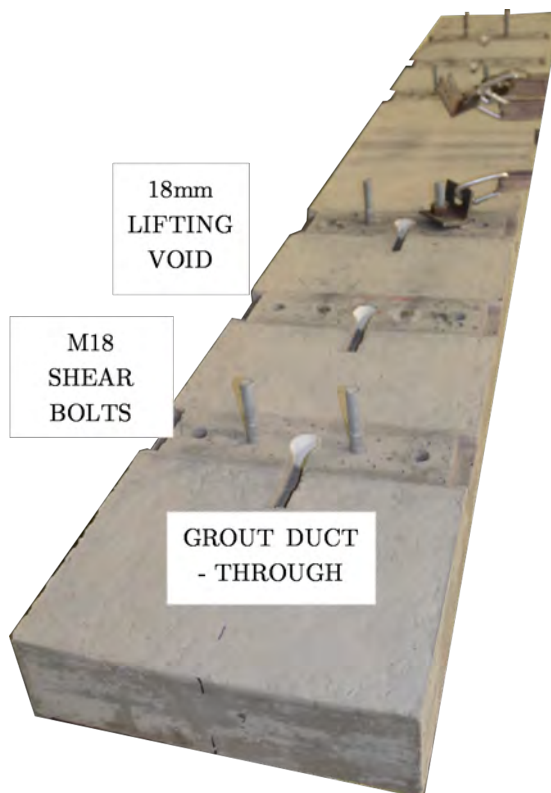
Figure 3.9: *NWC panel showing lifting voids, shear transfer bolts and grout ducts*

Figure 3.10: *Grout process for "floor-slab" connection showing relevant details*
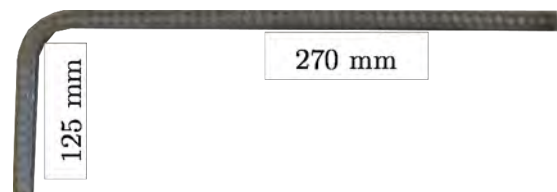
Figure 3.11: *Hand-bent Y12 rebar at grouted connection*

Figure 3.12: *NWC mould and rebar before casting*

Figure 3.13: *Grouting of lower grout connection between wall panels and "ground-slab"*
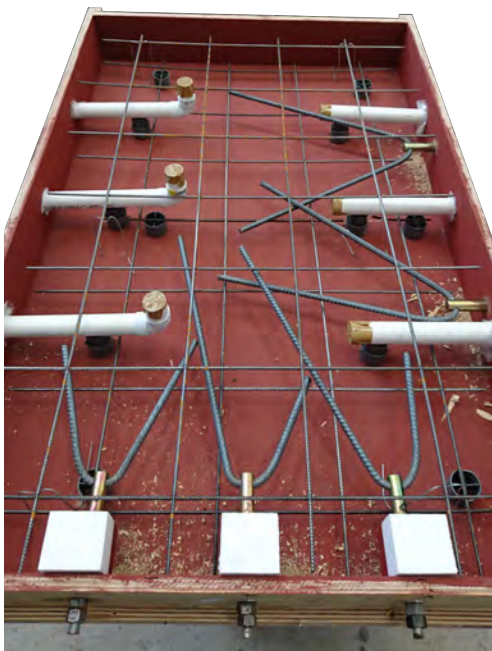
Figure 3.14: *LWFC mould showing 16 mm anchor bolts, 12 mm rebar, 40 mm grout ducts and wooden void spacers*

Figure 3.15: *Flat casting and poker vibration of LWFC panel showing Y12 anchor rebar as well as mesh Ref. 193*

3.2.3   Seismicity and Applied Loads

Seismic Base Shear

The applied vertical and lateral loads were calculated as per South African standards SANS 10160-2:2011 (SANS, 2011b), SANS 10160-1:2011 (SANS, 2011a) and SANS 10160-4:2017 (SANS, 2017) and utilised densities obtained through testing of cast concrete cube specimens (Section (3.3.1)). The major load on the structure for the prescribed push-over tests of Negro and Toniolo (2012) is the vertical live and self-weight loads of the structure. This sustained vertical load was determined in accordance with 10160-4:2017 (SANS, 2017) where load combination factor Ψ reduces the imposed "live" load factor from the ultimate limit state (ULS) value of $1.0 - 1.6$ in SANS 10160-1:2011 (SANS, 2011a) by $\Psi = 0.3$ to accommodate a major seismic load. The theory for this reduction is based on it being an unlikely for the ultimate live load in the structure due to occupancy to occur simultaneously with an earthquake. A summary of the calculations is presented in Table (3.4), the reader is directed to SANS 10160-4:2017 (SANS, 2017) §8.0 for the calculation procedure of sustained vertical load. Seismic loads are referenced under the accidental limit state ACC in SANS 10160-1:2011 (SANS, 2011a) §7.3.5.

As per the equivalent static lateral force procedure outlined in SANS 10160-4:2017 (SANS, 2017) the sustained vertical load was apportioned to the different levels of the structure to obtain the vertical distribution of base shear in proportion to mass of the elements. The vertical load on the ground floor was considered to be the self-weight of the LWFC walls while the first floor and second floor slabs were considered to support both the walls on them and the loads on the hollow-core floor slabs that bear on them. This load was then reduced slightly for the roof slab in accordance with SANS 10160-2:2011 (SANS, 2011b) which was at its own height level. The assumptions and results of this analysis are shown in Table (3.5). It must be noted that these results have been scaled in height and respective floor area by $1:3$ for the physical scale tests.

Table 3.4: *Summary of seismic design calculations for nominal sustained vertical loads W_n and lateral forces F_{xn} of scaled LWFC pilot building according to SANS 10160-4:2017 (SANS, 2017)*

Loads and Assumptions						**SANS 10160-4 Ref.**
LWFC Panel (Exterior)	1400	kg/m^3	*Reference peak ground acceleration, ag, Zone 1*	0.10	m/s^2	Fig. 1
LWFC Panel (Interior)	1450	kg/m^3	*Behaviour factor, q*	2.00		Table 4
Roof Dead Load	0.83	kg/m^2	*Building height, ht*	2.94	m	Sketch
Hollowcore Slab	2.6	kg/m^2	*Lwi/ht*	0.90	m	
Imposed Vertical Loads, Q_{ni}: SANS 10160-2: Table 1			*Effective shear wall area, Ac*	0.84	m^2	eq. 13
Domestic Dwelling	1.5	kPa	*CT*	0.08		eq. 12
Roof	0.25	kPa	*Period of Vibration, T*	0.18	S	eq. 11
Wall Length	2.76	m	*Ground Type*	4		Table 1
Wall height, l:	0.92	m	*S*	1.35		Table 2
Wall width (Exterior), h:	0.15	m	*TB*	0.20		Table 2
Wall width (Interior), h:	0.08	m	*TC*	0.80		Table 2
Floor Area	7.62	m^2	*TD*	2.00		Table 2
Wall Perimeter:	11.04	m	*Therefore T<= TB*			
Gravitational acceleration, g	9.81	m/s^2	*Design response Spectrum, Sd(T)*	0.16		eq. 2

Table 3.5: *Distribution of base shear calculated in Table (3.4) according to the relevant height levels of the prototype building and scaled* $1:3$ *according to laboratory restrictions.*

Bearing Wall: Seismic Loads at Each Level

Level	Nominal self-weight load, Gn [kN]	Load Combination Factor, ψ (SANS 10160-1)	Imposed vertical Load, Qn [kN]	Total sustained vertical load [kN]	
Ground	20.9	0.3	11.4	24.4	(Walls Only)
1st Floor	40.7	0.3	11.4	44.2	(Walls and Floor)
2nd Floor	40.7	0.3	11.4	44.2	(Walls and Floor)
Roof	6.3	0.3	1.9	6.9	(Roof Only)

Nominal sustained vertical load, Wn (eq. 9)	119.6	[kN]
Seismic base shear force, Vn (eq. 10)	19.4	[kN]

Now for Vertical distribution of base shear force:

Level	Weight [kN]	Height [m])	$w_x h_x$	C_{vx} (eq. 15)	Lateral Force, F_{xn} [kN] (eq. 15)
Ground	24.4	0.0	0.0	0.0	0.0
1st Floor	44.2	0.9	21.5	0.1	2.0
2nd Floor	44.2	1.8	78.0	0.4	7.1
Roof	6.9	2.6	113.3	0.5	10.3

Laboratory Vertical and Lateral Loads

In order to realistically simulate the physical scale tests it was essential to apply a self-weight load on the wall that would simulate the wall being a part of a larger building and in this case the lowest storey of a three-storey low-rise residential building. The sustained vertical loads calculated via SANS 10160-4:2017 in the previous section were applied to the tested walls via compressed springs.

It was assumed that the hollow-core floor slab spanned in one direction between two of the four LWFC walls where a single pair of walls did not support any floor or roof loading. These walls under reduced load were not considered.

The gross sustained vertical load per metre of wall during a seismic event was determined to be approximately 15 kN/m. This load was then reduced to account for the self-weight of the wall and the self-weight of the experimental setup of springs and structural steel sections (Section (3.2.4)) used to apply the load. The final load was determined per spring and load cell combination to be 4.3 kN for each of the six springs. The flow of this load distribution can be seen in Table (3.6).

Table 3.6: *Calculation of sustained vertical load per spring on LWFC wall for physical scale tests*

Load Element			From Seismic Calculations		
Roof	1.25	kN/m	*Roof*	6.89	kN
Wall	2.21	kN/m	*Wall*	24.35	kN
Floor	3.59	kN/m	*Floor*	19.81	kN
Wall	2.21	kN/m	**Where:**		
Floor	3.59	kN/m	*Wall Perimeter*	11.04	m
Wall	2.21	kN/m	*Single wall length*	2.76	m
Total a)	15.04	kN/m			
Less					
Springs	2.41	kN			
H Section	2.62	kN			
Top Concrete	2.40	kN			
Equals					
Per Spring	4.29	kN			

The lateral load was chosen in accordance with the JRC scientific and policy report: Design guidelines for connections of precast structures for push-over and cyclic testing (Negro and Toniolo (2012)), previously explained in Section (2.3.3).

The lateral load was applied via displacement control through the 500 kN Instron MTM Figure (3.8). It was essential for this machine that the load be applied without any bending moment or shear force on the load actuator or attached load cell. To ensure this the load

was applied from the load cell via a threaded bar, end-plate and structural steel section on top of the wall. This attachment was in contrast to rigidly connecting the Intron MTM and load cell to the transfer H-section and created a fail-safe to protect the Instron MTM. This load transfer mechanism can be seen in Figure (3.16) and is drawn to scale in Figure (3.8).

3.2.4   Laboratory Setup

The laboratory setup was similar to the masonry pull-over shear wall tests of De Beer (2016) conducted at Stellenbosch University structural engineering laboratory. The structural laboratory has a 500 mm thick RC strong floor to which a structural steel "meccano set" can be bolted in various arrangements. The lateral load was applied through a 500 kN Instron MTM, as can be seen in the lab setup Figure (3.8) where the physical test arrangement is shown. In this figure it is important for the reader to note:

1. The placement of the wall and shear bolts protruding from the NWC panels that are bolted into $254 \times 254 \times 89$ structural steel sections above and below the wall;

2. The anchor bolts through the strong floor at 920 mm centres;

3. The coil spring arrangements atop the wall to apply vertical load;

4. The load cells (LC) at the end of vertical 24 mm class 8.8 threaded bars attached to the coil springs;

5. The vertical roller supports on either end of the setup (Figures (3.16) and (3.17));

6. The load-transfer H-section at the end of the 500 kN Instron MTM;

7. The lateral support frames for safety and prevention of out-of plane motion on either side of the wall.

The horizontal support frames were placed as a safety measure due to the top-heavy coil spring arrangement. Each frame supports a bearing that secures the load spreader beam for out-of-plane movement but allows adequate vertical displacement, shown in Figures (3.16) and (3.17). As a further precaution to limit the displacement of the wall to only the applied lateral load and anticipated vertical deflection, a vertical support was placed underneath the wall on the far side Figure (3.17). This support limited the vertical displacement to upwards only, as expected. A pinned vertical support beneath the transfer H-section can also be seen in Figure (3.8), placed to prevent any damaging vertical displacement of the Instron MTM or attached 500 kN load cell.

Six $200 - 500$ kN load cells were used to monitor the sustained vertical load applied to the wall as per Section (3.2.3). The load cells were attached to parallel beams, also anchored to the laboratory strong floor alongside the wall ((d) in Figure (3.21)). Before the displacement was applied the springs were tensioned by hand via nuts tightened around the threaded rod through the springs (Figure (3.18)) according to the tensile load of 4.29 kN (Table (3.6)).
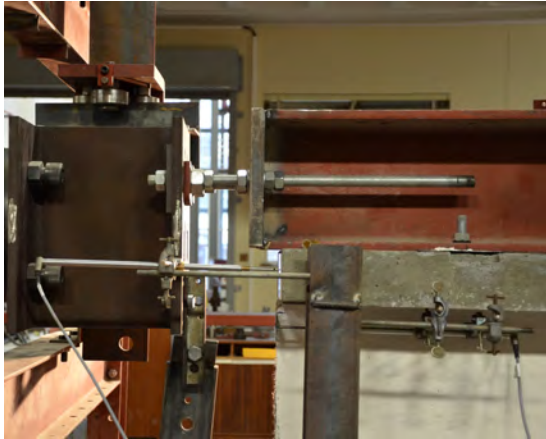
Figure 3.16: *Lateral support at load application point showing load application mechanism*
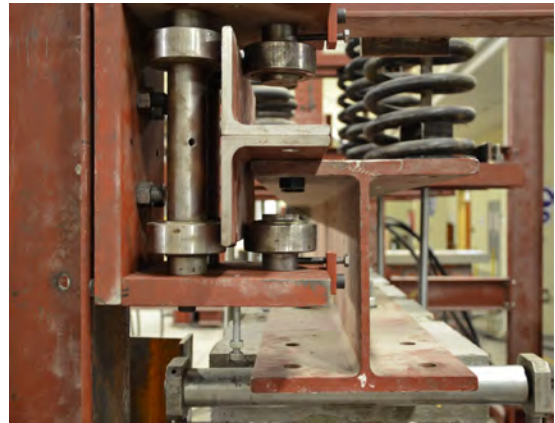
Figure 3.17: *Lateral and vertical support at unloaded end*

Figure 3.18: *Physical scale test laboratory setup for vertical load springs showing the left lateral support frame and pinned vertical support in part*

Boundary Conditions and Free-body Diagram

A simplified free-body force diagram is presented in Figure (3.19). The shear force is applied through the Instron MTM, transferred through the rigid steel beam via shear bolts to the NWC panel and applied via grouted rebar (horizontal connection) to the LWFC panels below. A rigid base connection is assumed as the lower NWC panel is attached to the laboratory strong floor via tension rods. Vertical force is applied through compression of the springs and monitored by load cells below. Displacement is expected at the horizontal and vertical connections as indicated by the black arrows.
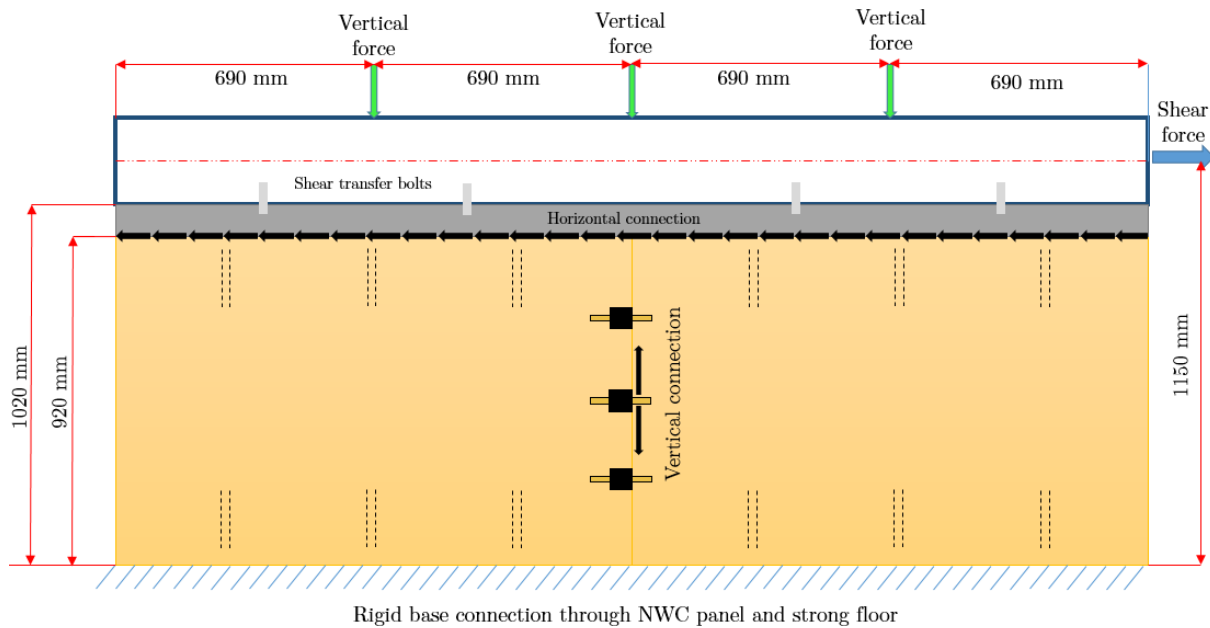
Figure 3.19: *Physical scale test free-body force diagram*

In the tests conducted by De Beer (2016) it was seen that the connection to the laboratory strong floor was not as rigid as initially assumed and slipping of the displaced wall was observed. After this observation the decision was made to pull the wall through "pull-over" in contrast to standard "push-over" testing, justified by the symmetrical wall design and homogeneous material properties. Additionally this slippage would be reduced by the force loop of the wall test setup, comprising of: the pulling force of the Instron MTM, the resistance of the rigidly bolted vertical steel frame, the steel stiffeners on the floor connecting the rigid beam beneath the wall to the meccano set and finally the shear forces within the LWFC wall itself. A schematic of the loop is shown in Figure (3.20), extracted from Figure (3.8).

Data Collection

All of the test data was obtained through displacement measuring LVDT's and load cells (LC). Data from the LC's and LVDT's was collected at a rate of 5 Hz by a computer through a Spider 8 data logger system to which the Instron MTM's load and displacement were also connected. On the opposite side of the wall the displacement and cracking movement was monitored with a high resolution camera at 12-15 photographs per minute. Figure (3.21) details the placement of eleven LVDT's used as well as further lab setup

Figure 3.20: *Physical scale test force loop to limit slip via pull-over testing*

components. A closer view of the NWC left horizontal top LVDT can also be seen in Figure (3.16).
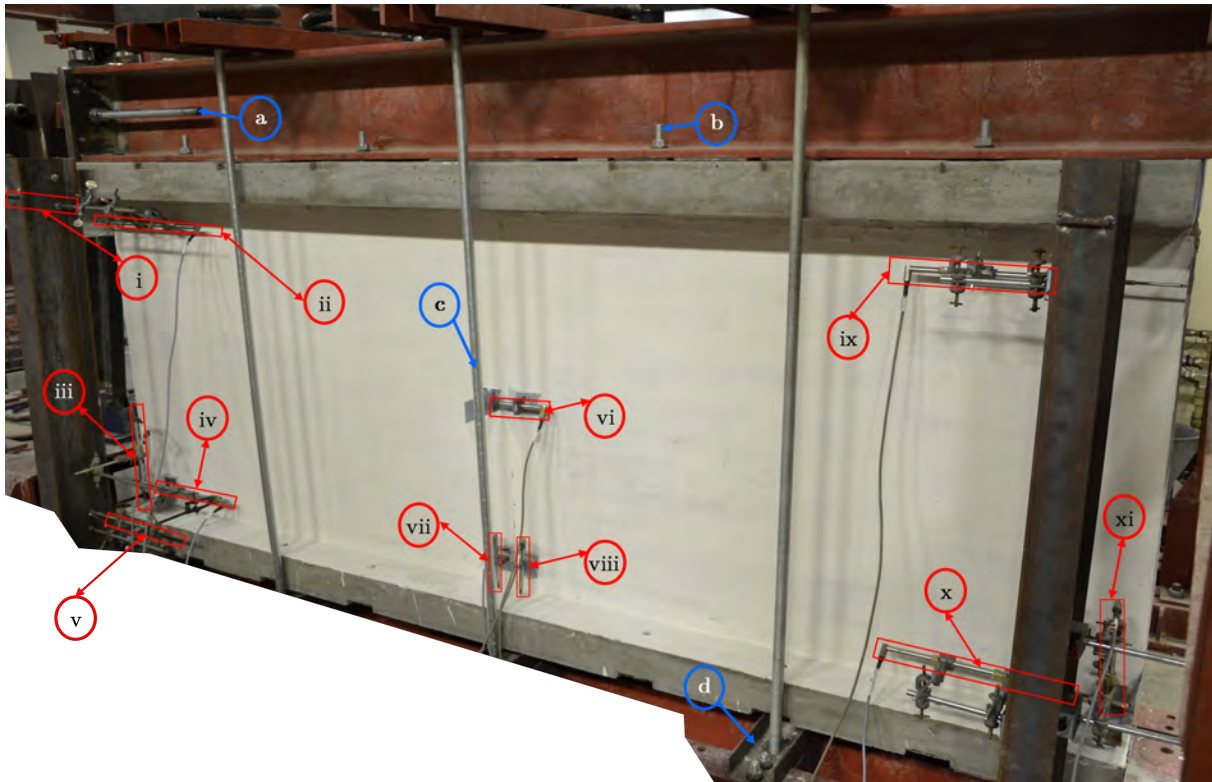
Figure 3.21: *LVDT placement and further lab setup details: (a) Lateral load transfer bar, (b) M18 Shear transfer bolts, (c) 24 mm threaded bar for vertical load application (d) LC positioning bracket as used by (De Beer (2016)), (i) NWC left horizontal top LVDT, (ii) LWFC left panel horizontal top LVDT, (iii) LWFC left panel vertical LVDT, (iv) LWFC left panel horizontal bottom LVDT, (v) NWC left horizontal bottom LVDT, (vi) LWFC vertical connection horizontal displacement LVDT, (vii) LWFC left panel vertical connection vertical displacement LVDT, (viii) LWFC right panel vertical connection vertical displacement LVDT, (ix) LWFC right panel horizontal top LVDT, (x) LWFC right panel horizontal bottom LVDT, (xi) LWFC right panel vertical LVDT*

3.2.5   Test Specimens

Physical Scale Test 1

The initial physical scale test (PST 1) was conducted as monotonic pull-over with maximum vertical load imposed by the coil springs. The horizontal connections were both grouted with the maximum six connections per LWFC panel, three horizontal connections with each NWC panel at the horizontal connections. Three anchored boxes were used for vertical connections as shown schematically in Figure (3.22).
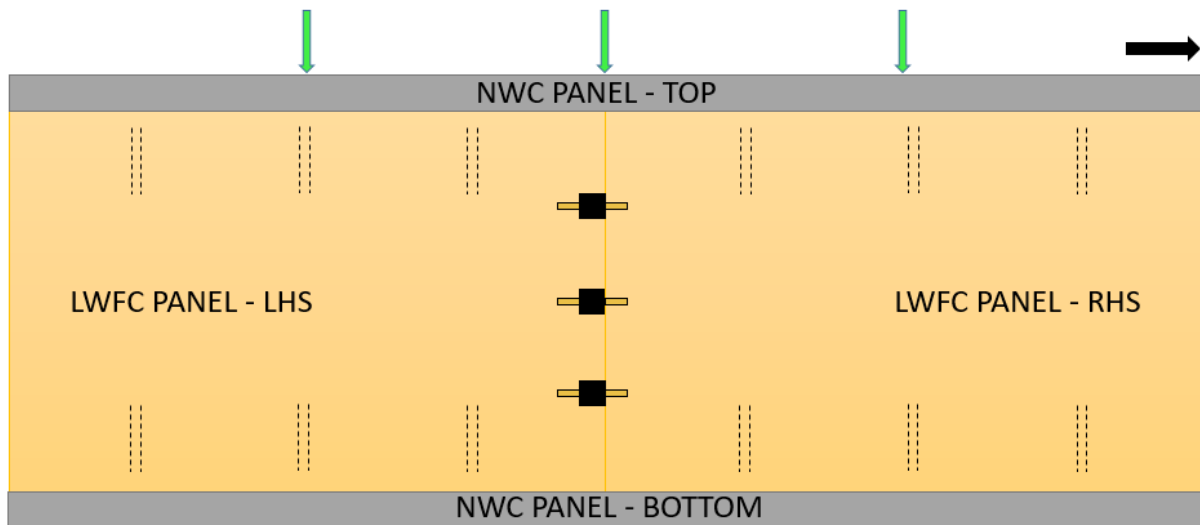
Figure 3.22: *Physical scale test 1 showing pull-over load and connection placement. Three vertical connection boxes and six horizontal grouted rebar per LWFC panel are indicated.*

Physical Scale Test 2

PST 2 made use of the force displacement results of PST 1 to apply a quasi-static seismic, cyclic load test to a similarly connected and loaded wall. This test was performed in accordance with JRC scientific and policy report: Design guidelines for connections of precast structures for push-over and cyclic testing (Negro and Toniolo (2012)), previously explained in Section (2.3.3).

The schematic diagram of PST 2 is shown in Figure (3.23) and differs from PST 1 with regard to load direction where now a load in both left and right horizontal directions has been applied.
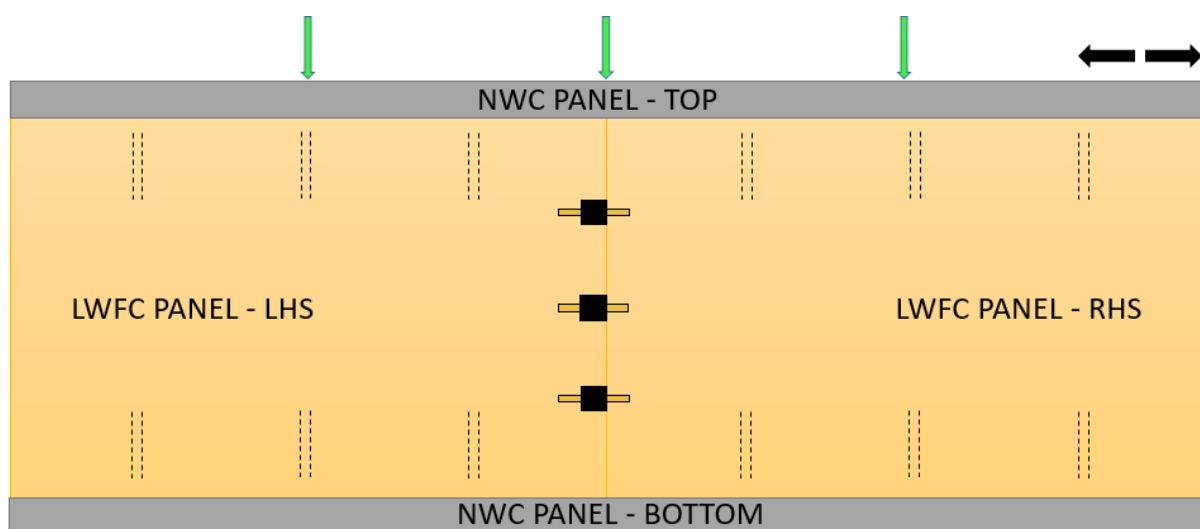
Figure 3.23: *Physical scale test 2 showing cyclic load and connection placement. Three vertical connection boxes and six horizontal grouted rebar per LWFC panel are indicated.*

Physical Scale Test 3

Final physical scale test, PST 3, was conducted as quasi-static pull-over with maximum vertical load imposed by the springs, a repeat of PST 1. The horizontal connections were however reduced from six to four grouted rebar per LWFC panel to gain an understanding on how the amount of grouted rebar along the horizontal connection influences the wall capacity and connection behaviour. Three anchored boxes were again used for vertical connections and can be seen in Figure (3.24).
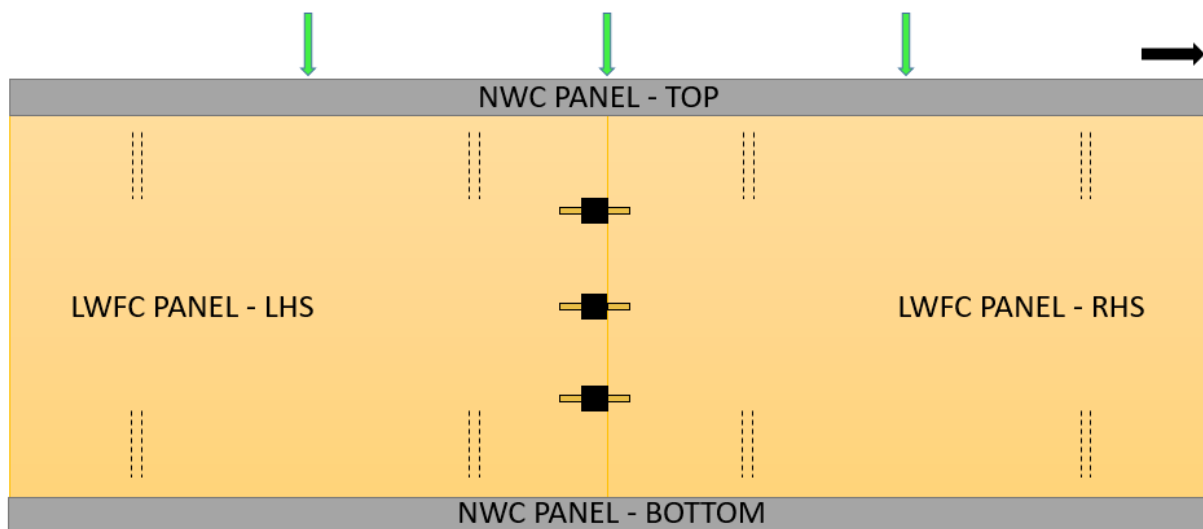
Figure 3.24: *Physical scale test 3 showing pull-over load and connection placement. Three vertical connection boxes and four horizontal grouted rebar per LWFC panel are indicated.*

3.3 Characterisation Tests

Material characterisation tests were conducted for the LWFC and NWC used in this study to establish the material properties for modelling of concrete as well as quality control and material improvement. The maximum mix volume for the LWFC mixer in Figure (3.1) for this particular mix was empirically found to be approximately 53 *litres*. Each of the six LWFC panels constructed required four 53 *l* mixes of the same mix design in Table (3.2) for the 1.38 *m* long, 0.92 *m* tall and 0.15 *m* thick panel of approximately 190 *l* volume. Twelve 100 *mm* cube specimens were cast for each of the four mixes and tested for compressive strength at 7, 14, 21 and 28 (56) days to monitor the strength development. Due to the limited mixer capacity LWFC cylindrical specimens (100 *mm* diameter, 200 *mm* high) cylinders were only cast from the final mix of the last constructed panel to determine the Young's modulus of this LWFC.

The compressive strength of the NWC panels was also monitored via twelve 100 *mm* cube specimens, cast for each of the six 115 *l* panels cast according to the NWC mix design in Table (3.2).

3.3.1 Compressive Strength

A uni-axial compression test was performed according to the specifications laid out in SANS 5863 (SANS, 2006) to determine the compressive strength. The test apparatus was a

Contest Grade A compression testing machine, operated at a force control of 180 kN/min as prescribed in SANS (2006) for 100 mm cube specimens. The compressive strength (f_{cu}) was therefore calculated according to Equation (3.4).

$$f_{cu} = \frac{F_s}{A} \qquad (3.4)$$

Where:
F_s is the maximum load applied [N]
A is the specimen cross-sectional area normal to the applied load [mm^2]

3.3.2   Young's Modulus

Due to there being no prescribed South African National Standard for the determination of Young's modulus of hardened concrete, the Eurocodes were consulted and the procedure outlined in EN 12390-13:2013 BSI (2013) was followed. Cylindrical specimens of diameter 100 mm and 200 mm height were cast and tested at 28 days.

The first cylinder was crushed to obtain the cylindrical compressive strength f_{ck}, in contrast to utilising the compression cube strength f_{cu} and reducing it by a factor of 0.8 to obtain an approximate cylindrical compressive strength f_{ck}; as outlined in BSI (2013). This change provided accurate limits for the loading cycle required for Young's modulus testing as it was assumed that the reduction factor of 0.8 may differ for LWFC. The required stress limits σ_a (nominal upper), σ_b (nominal lower) and σ_p (nominal preload), in relation to f_{ck} are noted in Equations (3.5), (3.6) and (3.7) and are used to determine a safe elastic region within which to calculate the Young's modulus (Table 1 of BSI (2013)).

$$\sigma_a = \frac{f_{ck}}{3} \qquad (3.5)$$

$$0.10(f_{ck}) \leq \sigma_b \leq 0.15(f_{ck}) \qquad (3.6)$$

$$0.5 \; MPa \leq \sigma_p \leq \sigma_b \qquad (3.7)$$

The load was again applied via a Contest Grade A compression testing machine and the strains were measured over a gauge length of 70 mm via three equally spaced LVDT's held in place by a custom-made bracket (Figure (3.25)). The compressive force was accurately read by a 250 kN external load cell and was applied for three cycles where the limit stress σ_a (Equation (3.5)) was reached for each cycle. The Young's modulus was calculated according to Equation (3.8) through the determination of a stress-strain curve for the third load cycle of each cylinder. The applied load cycles can be seen in Figure (3.26).

$$E = \frac{\sigma_{a,m} - \sigma_{p,m}}{\epsilon_{a,3} - \epsilon_{p,2}} \qquad (3.8)$$

Where according to BSI (2013):
$\sigma_{a,m}$ is the measured upper stress of the third load cycle [MPa]
$\sigma_{p,m}$ is the measured nominal pre-load stress [MPa]

$\epsilon_{a,3}$ is the average strain at maximum stress on load cycle 3 $[mm/mm]$
$\epsilon_{p,2}$ is the average strain at minimum stress on load cycle 2 $[mm/mm]$
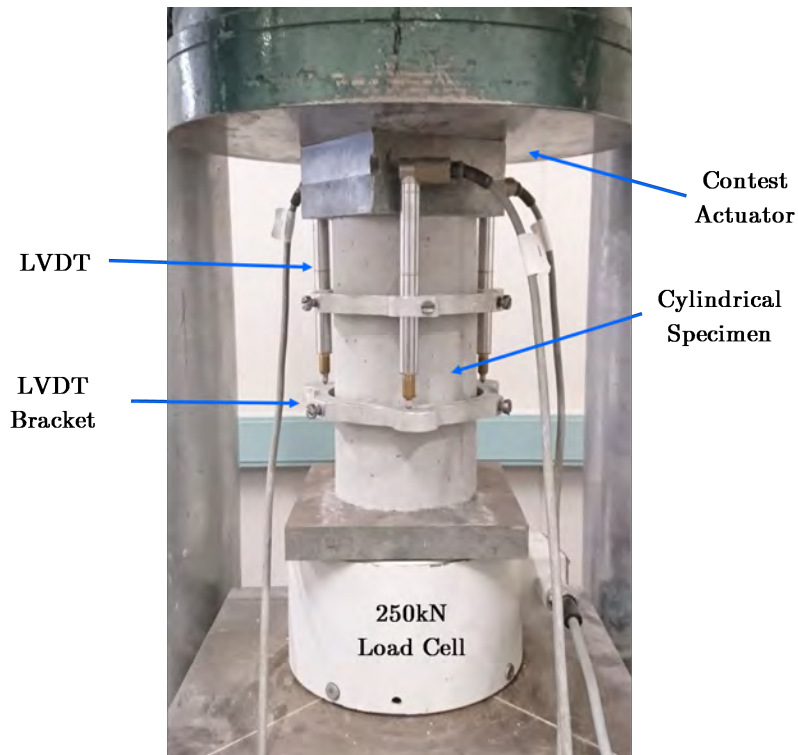
Figure 3.25: *Young's modulus test and Contest compression testing machine*
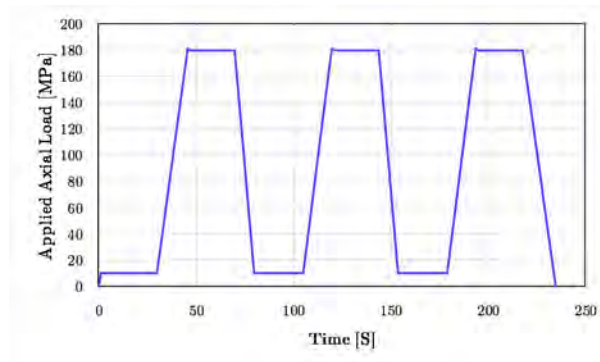
Figure 3.26: *Young's modulus test: The three load cycles applied to the specimen graphed for an idealised test result*

Chapter 4

Numerical Analysis

This chapter details the finite element (FE) numerical analysis of the physical scale tests conducted in this thesis. The development of a preliminary nonlinear LWFC material model is explained with reference to literature. The physical scale test (PST) FE model is explained and thereafter used via DIANA FEA package to replicate the pull-over testing referenced previously as PST 1 and PST 3. The chapter is concluded with a brief explanation of the analysis procedure used, the limitations of the FE model and details on the preliminary FE model test results and sensitivity study.

4.1   Introduction

Limited LWFC material testing on a variety of mix designs and ingredients has been conducted and explained in Section (2.1). As a starting point for the structural tests evaluated in this report, a nonlinear material model and subsequent FE analysis was conducted.

Series of material tests on LWFC conducted within the Stellenbosch University structural engineering research unit *Centre for Development of Sustainable Infrastructure* (CDSI) contributed to the understanding of the mechanical behaviour required to accurately develop this FE model. The conclusions, recommendations and material test results of Van Rooyen (2013), De Villiers *et al.* (2017), Grafe (2017) and Van Zijl *et al.* (2017), as well as the results of this research, were used to formulate this material model for the structural use of LWFC in South Africa.

It was important for the material model that the experimentally derived material properties used were all of the exact same material and mix design. For this reason the preliminary material model developed made use of the results of Grafe (2017). Grafe (2017), who conducted comprehensive tests on LWFC, provided accurate values of the fracture energy, and indirect tensile strength of LWFC. These two characteristic tests were not conducted for the mix design utilised for physical scale tests in this thesis. A summary of the material properties of the preliminary LWFC material is presented alongside the FE model parameters in Section (4.7).

The finalised material model and results of comparative FE tests required an updated material model. The numerical results in Section (5.3) are based on updated material

properties derived from characteristic tests conducted on the physical wall specimens. In the updated model the individually tested material properties of Young's modulus, density and compressive strength were updated, however the specific theory used for each material property remained the same as the preliminary FE model.

4.2 Preliminary Nonlinear LWFC Material Model

A nonlinear total strain rotating crack material model was utilised for the LWFC material model. This material model was chosen after considering the research of De Villiers (2015) who observed low fracture energy, brittle failure for reinforcement bond in LWFC. Replicating this brittle response as well as the flexural response observed by Jones and McCarthy (2005) necessitated a material model that allowed for cracking.

Another justification for this chosen material model is the reinforcement within the LWFC panels and the changing crack orientation near the reinforcement. For a rotating crack model the cracks are distributed or smeared over an area and they have an independent axis system, allowing a varied orientation (Feenstra *et al.*, 1991). The stress-strain relations are evaluated in the principle directions of the strain vector and are well suited to modelling reinforced concrete structures (DIANA FEA BV, 2016*c*).

4.2.1 Compressive Behaviour

As input for the compressive behaviour of LWFC in the material model, the Maekawa cracked concrete curves (Maekawa *et al.*, 2003) were seen to adequately replicate the compressive strain behaviour of Grafe (2017). The compressive curve plotted in Figure (4.1) against the stress-strain curves of the optimal Mix 8; selected by Grafe (2017) for the optimal mix design for fracture energy improvement of LWFC. This selection of the Maekawa curve is in contrast to the Thorenfeldt model (Thorenfeldt *et al.*, 1987) also available for the total strain rotating crack model in DIANA FEA (DIANA FEA BV, 2016*c*).

4.2.2 Tensile Behaviour

Uniaxial tensile tests (UTT) were performed and compared to the indirect tensile strength determined by Grafe (2017) for the tensile behaviour of LWFC to be incorporated in this nonlinear material model. The optimal LWFC mix 8 of Grafe (2017) was repeated and tensile "dog-bone" specimens were cast with a cross-sectional area of 40 $mm \times 80$ mm in the prismatic gauge area. Mesh reinforcement was placed at the center of the two larger ends of the specimen to help prevent failure outside of the 80 mm gauge length.

The tensile specimens were placed in hydraulic clamps of a 250 kN Zwick MTM and tested under displacement control of 0.1 mm/min until failure. The specimen and test setup are shown in Figures (4.2) and (4.3) respectively. Ultimately it was observed that the Hordijk tensile curve (Hordijk (1991)) fits the tensile response for the 1400 kg/m^3 dry density LWFC with polypropylene fibres. The Hordijk model was therefore selected for the nonlinear LWFC material model, now based on this direct tensile strength. Further details of these tests and the comparison between direct and indirect tensile strength can be read in Van Zijl *et al.* (2017). The DIANA application of the theory behind the Hordijk tensile curve (Hordijk, 1991) is detailed in §20.1.1.6 of DIANA FEA BV (2016*c*).
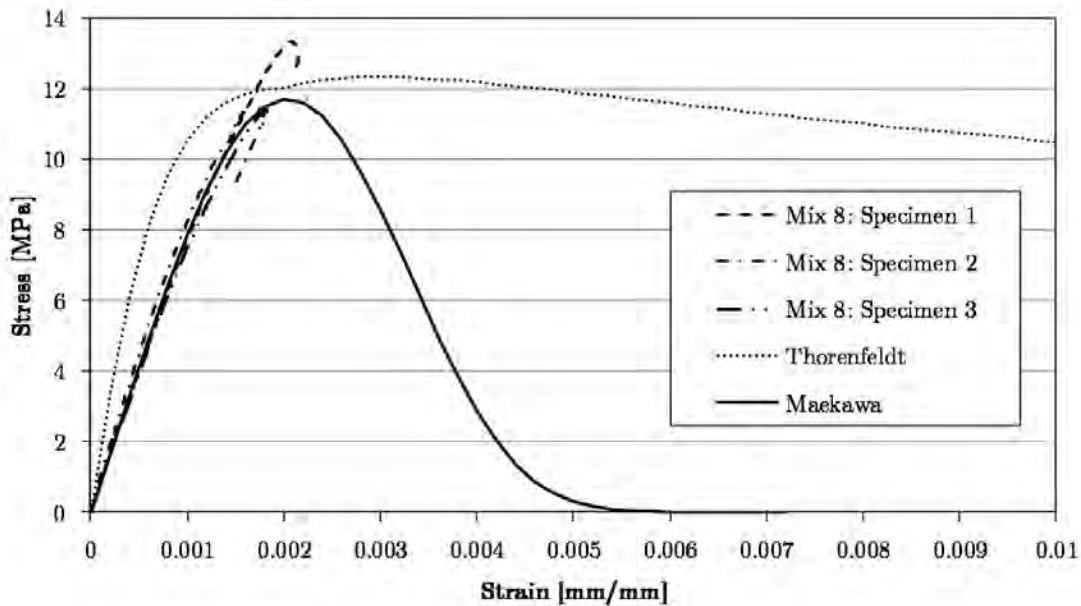
Figure 4.1: *Maekawa (Maekawa et al. (2003)) and Thorenfeldt (Thorenfeldt et al., 1987) compressive curve comparison with the results of Grafe (2017) in selection of the compression function for the LWFC nonlinear material model.*

A consideration for the final LWFC material model (5.2) was the relationship between indirect and direct tensile strength of LWFC. The results of this test and results of the comparative indirect tensile strength for LWFC of the same mix design, tested by Grafe (2017) as "mix 8", were compared and shown to be approximately 25 % less. The average direct tensile strength from the UTT was 1.41 MPa and contrasted with the indirect tensile strength of 1.76 MPa. This notable difference was factored into the final LWFC material model where the indirect tensile strength results of De Villiers *et al.* (2017) were reduced, leading to an increased characteristic length of the material.

Figure 4.2: *Notched dog-bone UTT specimen showing successful tensile crack and visible polypropylene fibres (circled).*
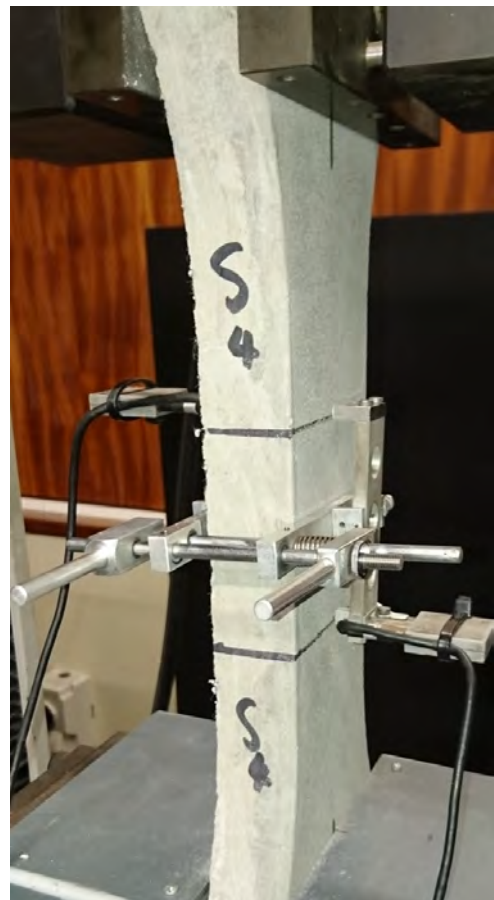
Figure 4.3: *UTT test setup showing extensometers at 80 mm gauge length and central 5 mm deep notch across both short sides of the cross-section*

4.2.3 Young's Modulus

The Young's modulus determination for nonlinear material input was based on the experimental method explained in Section (3.3.2). Tests were conducted according to the procedure outlined in BS EN 12390-13:2013 BSI (2013) on 100 mm diameter and 200 mm tall cylinders. The Young's modulus used in this material model was experimentally determined by Grafe (2017) according to this method.

4.2.4 Fracture Energy

Fracture energy is the amount of energy required to create one unit area of a crack, where the area of a crack is defined as the projected area on a plane parallel to the main crack direction (RILEM (1985)). Low fracture energy (G_f) and hence low characteristic length (l_c) was shown by De Villiers *et al.* (2017) to be the main reason for the poor bond performance of LWFC as explained in Section (2.1.8). Fracture energy was therefore considered an important material property for the nonlinear LWFC material model.

Fracture energy was determined by Grafe (2017) via two distinctly different yet valid methods. The Notched beam bending test developed through RILEM (1985) and codified in JCI (2003) contrasts with the wedge-splitting test of Brühwiler and Wittmann (1990) by applying tension across the crack opening indirectly through flexure rather than through a more direct splitting along a predetermined crack as indicated in Figure (4.7). It was seen in the results of Grafe (2017) that the fracture energy of the same mix varied considerably between the two test methods and at times a factor of ten difference between these tests was observed. This large variation in G_f between the results is thought to be attributed to the different manner in which the fracturing tensile force is applied and it is hypothesised that this is the reason for the larger notched-beam fracture energy.

Notched Beam Bending Test

The notched beam fracture energy test chosen by Grafe (2017) was the Japan Concrete Institute Standard (JCI-S-001-2003) *Method of test for fracture energy of concrete by use of notched beam* (JCI, 2003). It is a codified test based on the recommendations of FMC-50 RILEM (1985). For this crack mouth opening displacement (CMOD), closed-loop controlled test, the fracture energy of concrete is calculated from the load-CMOD curves resulting from the deflection of a beam of the dimensions described in Figure (4.4) under three-point-bending. The crack is formed on the tension (notched) side of the beam as the vertical load (applied on the un-notched side) and crack mouth opening displacement are monitored.

The JCI test relies on an elimination of torsion on the specimen to enable as close to a pinned three-point bending test (TPBT) as possible (Figure (4.5)). This was enabled by the test setup at the Stellenbosch University Structural laboratory as shown in the report of Grafe (2017) and in Figure (4.6). During these tests the vertical load was applied via a 2 MN Instron MTM to a notched beam of $100 \times 100 \times 500$ mm. Before testing a 30 mm deep, 3 mm wide notch was cut into the tensile face of the specimen at 28-day cured concrete strength to create a predictable fracture point. For further details of these tests the reader is directed to §7.5 of Grafe (2017).

An initial area of scrutiny for this test was the results of Grafe (2017) that showed the Load-CMOD curve plateauing but not rupturing completely at failure due to fibre
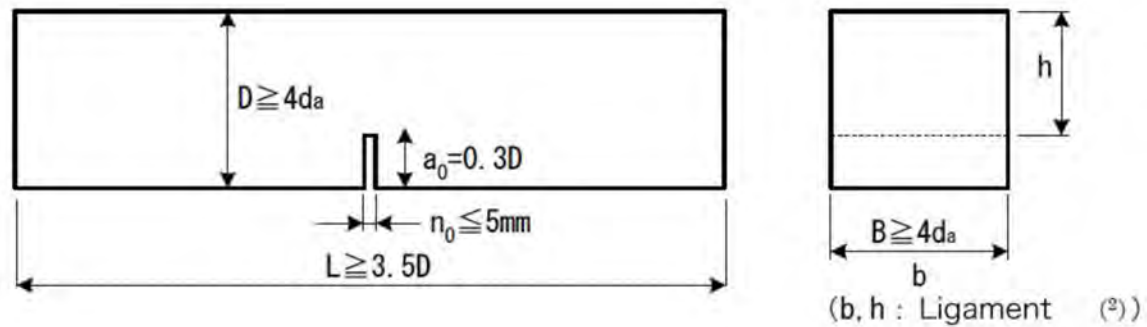
Figure 4.4: *Notched beam specimen dimensions as detailed in JCI (2003)*
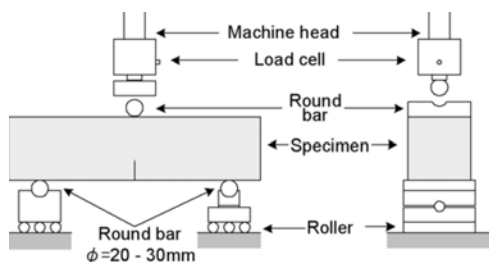
Figure 4.5: *Prescribed notched beam fracture energy test setup JCI (2003)*
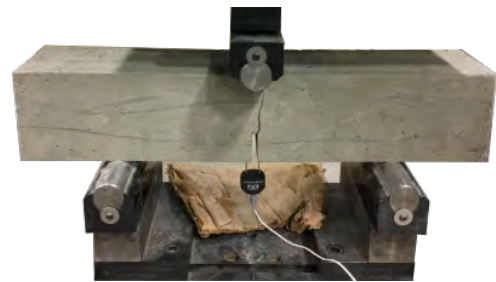
Figure 4.6: *JCI notched beam fracture energy test setup of Grafe (2017) noting the clip gauge monitoring the CMOD.*

bridging across the crack (Figure (4.10)); this required an approximate point at which to assume specimen failure. A practical rupture limit for the fracture energy, also termed the "practical zero" by Elices *et al.* (1992) was chosen by Grafe (2017) to be 0.75 *mm*.

Fracture energy of foamed concrete via notched beams was tested by Kozlowski *et al.* (2015), who concluded that fracture energy G_f increases with an increase in the density of foamed concrete and that the fracture energy ranged from $1.39 - 12.54$ *N/m* for low strength foamed concrete of densities between 488 and 1024 kg/m^3. These results are considerably less than the 69.32 *N/m* fracture energy determined by Grafe (2017) for denser (1400 kg/m^3) LWFC (Grafe, 2017). A further area of scrutiny is the effect of specimen dimensions on the test results, although opinion on this does vary (Elices *et al.*, 1992), it was deemed necessary to further investigate the notched beam fracture energy test results.

Wedge Splitting Test

The modified wedge splitting test was proposed by Brühwiler and Wittmann (1990) to be better than the stable notched beam test of FMC-50 (RILEM, 1985) for determination of specific fracture energy (G_f). In contrast to the notched beam fracture energy test, the vertical force in the wedge-splitting test is translated geometrically through wedges into a lateral, horizontal force via the Equation (4.1). By applying tensile stress directly across the crack it is assumed a closer test to the theoretical fracture energy based on uniaxial tensile tests where pure-tension is applied (Brühwiler and Wittmann, 1990). The wedge splitting test schematic can be seen in Figure (4.7) and the wedge splitting test execution

of De Villiers (2015) and Grafe (2017) can be seen in Figure (4.8)

$$F_h = \frac{F_v}{2 \cdot \tan(\alpha_w)} \tag{4.1}$$

Where:
F_h is the horizontal splitting force
F_v is the applied vertical force
α_w is the wedge angle
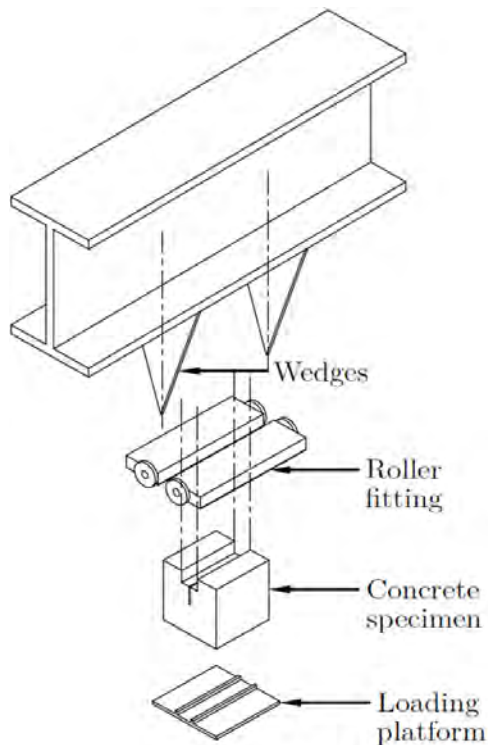
Figure 4.7: *Wedge splitting fracture energy test setup according to Brühwiler and Wittmann (1990)*
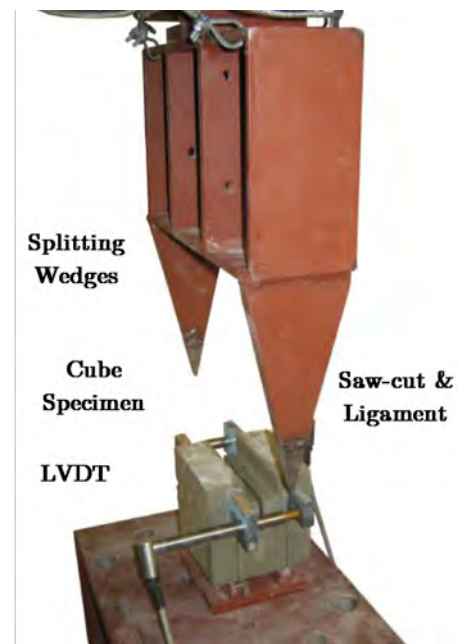
Figure 4.8: *Wedge splitting fracture energy test execution of De Villiers (2015) and Grafe (2017) on 100 mm cube saw-cut specimens.*

This fracture energy test method was used by De Villiers *et al.* (2016) to determine the fracture energy of LWFC. It was however challenging to obtain usable fracture energy data due to the increased brittleness of the fibre-less LWFC. Experimental repeatability was a challenge as complete splitting failure occurred before measurable crack opening displacement (COD) was measured and resulted in unusable data (De Villiers *et al.*, 2016). In comparison: with polypropylene fibre addition, the control of these wedge-splitting fracture energy tests was significantly improved and consistent results were produced by Grafe (2017).

The results of the wedge-splitting test for mix 8 of Grafe (2017), $G_f = 18.21$ *N/m* did however differ considerably from the notched beam TPBT. It was therefore decided that the notched-beam bending test would be simulated via DIANA FEA and make use of the preliminary LWFC material model in order to confirm the accurate fracture energy for the LWFC material model.

Modelled Fracture Energy

In order to confirm the fracture energy to be modelled for the physical scale tests, the notched-beam fracture energy test was modelled in DIANA to confirm the fracture energy output. This was a preliminary nonlinear LWFC material model where the previously mentioned material parameters of Grafe (2017) were input alongside the notched beam fracture energy of $G_{f,beam} = 69.32\ N/m$ to obtain a FE vertical force-CMOD curve.

The FE model shown in Figure (4.9) was modelled in DIANA FEA according to the specifications of JCI-S-001-2003 (JCI, 2003). A total strain rotating crack plane stress analysis was performed. To allow for a direct crack forming, a tension interface was created at the symmetrical centre of the beam. The analysis was modelled under CMOD displacement control along this interface. The vertical force and CMOD were noted and compared to that of Grafe (2017).

It was seen that the fracture energy which developed at the "practical zero" rupture point, chosen by Grafe (2017) to be 0.75 mm, compared favourably with the experimental data. Table (4.1) details the results of the four fracture energy specimens tested by Grafe (2017) for LWFC mix 8 and compared to the DIANA FEA results, including the necessary measurements of $W0$ & $W1$ used to calculate the fracture energy according to JCI (2003) §6.1. At this same practical zero point, the $G_f = 69.32\ N/m$ input leads to a $G_f = 63.2\ N/m$ output, increasing to $G_f = 65.9\ N/m$ if the practical zero point is extended to 0.942 mm for the FE simulation. A graph showing the variation of CMOD and vertical force used to calculate the fracture energy for both the experimental results and DIANA FEA is displayed as Figure (4.10).
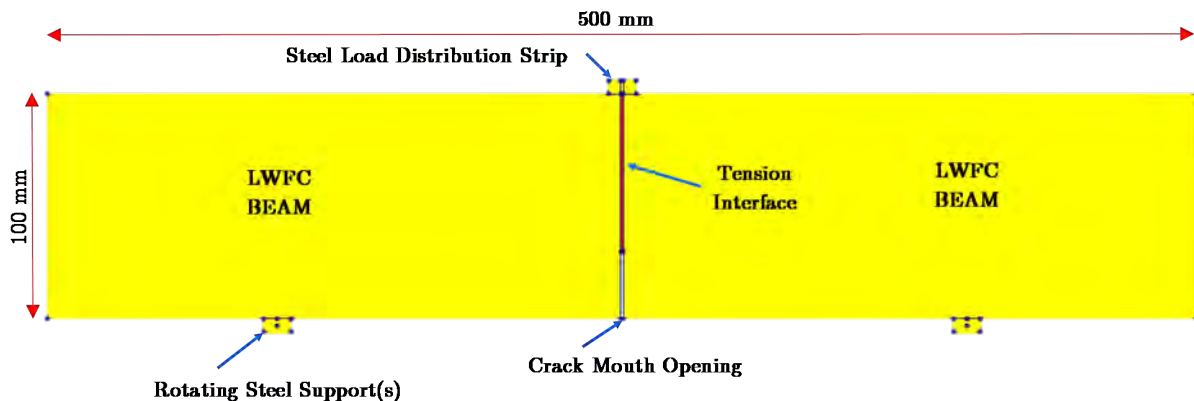
Figure 4.9: *DIANA FEA showing layout of FE model for notched-beam fracture energy.*

The numerically modelled load displacement curves in Figure (4.10) show similar overall load-CMOD behaviour but a different shape to those of the physical beams. The peak of the DIANA FEA curve was slightly lower than the experimental test specimen and decreased gradually in comparison to the initially steep softening physical test results. Another more significant difference between the two tests is the plateau of the physical test curves in contrast to the near-complete fracture of the FE model. It was hypothesised by Grafe (2017) that the plateau was due to polypropylene fibre bridging across the crack and this is likely to explain why this physical phenomenon is less apparent in the FE model where individual fibres were not modelled. Further refinement of this FE model

Table 4.1: *Results of the four fracture energy specimens tested by Grafe (2017) for LWFC mix 8 compared to the DIANA FEA notched beam test results, including the necessary measurements of W0 & W1 used to calculate the fracture energy according to JCI (2003) §6.1.*

Specimen	W0	CMODc	W1	GF
	$[Nmm]$	$[mm]$	$[Nmm]$	$[N/m]$
1	662	0.75	25	74
2	576	0.75	25	65
3	620	0.75	25	70
4	598	0.75	24	68
Average	614	0.75	24.7	69.3
Diana, Beam	557	0.75	25	63.2
Diana, Wedge	145	0.39	12.8	17.3
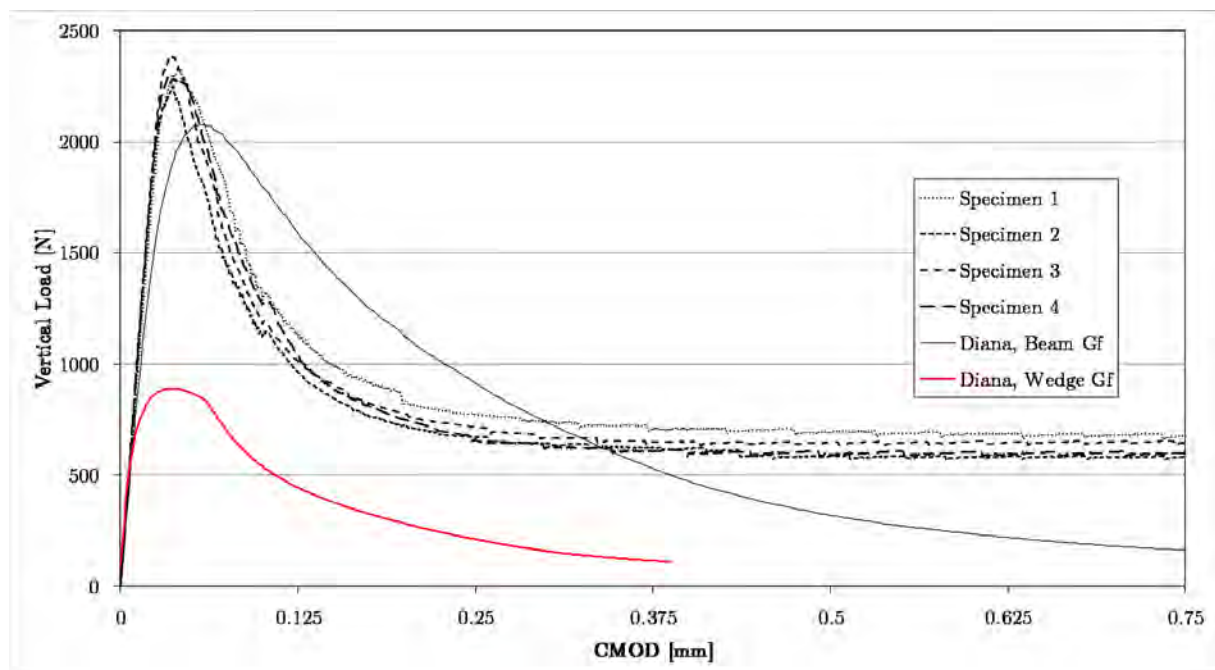
Figure 4.10: *Notched beam fracture energy comparison between Grafe (2017) and DIANA FEA*

through evaluation of the roller support, friction behaviour is required for a better fracture energy test comparison.

A comparative analysis was made where the wedge-splitting $G_f = 18.12 \ N/m$ and reduced tensile strength were input into the FE model to show the reliability of the FE model and it's sensitivity to G_f. The results of this comparative analysis were favourable and the output of $G_f = 17.3 \ N/m$ in Table (4.1), graphed in red on Figure (4.10) gives greater confidence in the notched beam fracture energy results. The FE model was seen to be sensitive and accurately created a lower fracture energy vertical load - CMOD curve for the reduced fracture energy material.

Chosen Fracture Energy

In conclusion it was seen in Table (4.1) that the overall output of the DIANA FEA and the notched-beam fracture energy compared favourably. In this LWFC nonlinear material model it was therefore decided that the notched beam fracture energy of $69.32 \sim 70 \ N/m$ determined by Grafe (2017) would be used.

4.3 Zero-tension Interface

At both the vertical connection between the two LWFC panels as well as the horizontal connections between the LWFC and NWC panels, a zero-tension high-friction interface was modelled. This interface, outlined in red in Figure (4.18) and shown schematically in Figure (4.19) was placed in the model to ensure that only frictional forces were allowed between the panels and that tensile forces were carried across the connection through the reinforcement bars.

A Coulomb friction interface as described in §9.4.1 and detailed in §26.4.1 of DIANA FEA BV (2016c) was implemented. The 2D line interface element and degrees of freedom are shown in Figure (4.11) from §12.2.7 of DIANA FEA BV (2016b) where the lines represent the inter-facial edges of the respective concrete specimens.
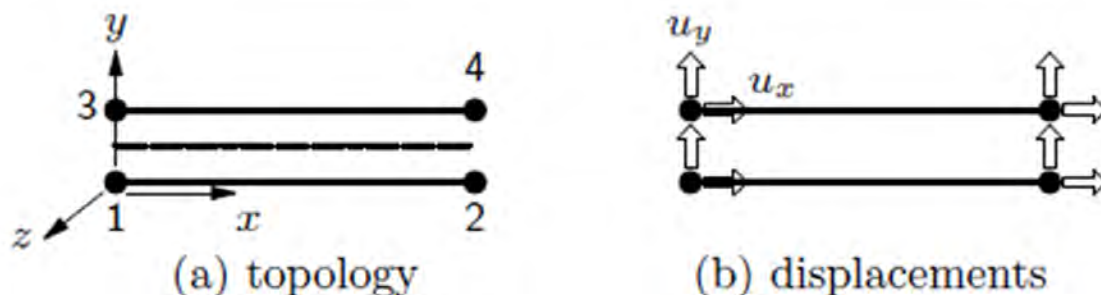
Figure 4.11: *Line interface utilised for zero tension property between concrete elements showing (a) Element topology and (b) Displacement degrees of freedom (DIANA FEA BV, 2016*b*).*

As input for the interface material model the normal (K_n) and tangential, shear (K_s) elastic stiffnesses were calculated according to Equations (4.2) and (4.3) where the stiffnesses are related to a spring stiffness across the interface (Fine Software, 2017). The shear modulus

of elasticity is related to the Young's modulus and Poisson's ratio through Equation (4.4) in McNaught and Wilkinson (1997) and the thickness (t) of interface contact area was taken as the wall thickness of the physical scale tests, $0.15\ m$. The calculated stiffness values are shown alongside the friction factors for the zero-tension interface in Table (4.3).

$$K_n = \frac{E}{t} \tag{4.2}$$

$$K_s = \frac{G}{t} \tag{4.3}$$

Where:
t is the assumed thickness of the interface contact area
G is the shear modulus of rigidity
E is the Young's modulus of elasticity

and

$$G = \frac{E}{2 \cdot (1 + \nu)} \tag{4.4}$$

Where:
ν is the Poisson's ratio of the material

4.4   Normal Weight Concrete Material Model

The material model for the normal weight concrete panels was based upon the fib Model Code for Concrete Structures, C40 (fib Model Code (2010)). The mix design of the NWC panels can be seen in Table (3.2) and the concrete model properties were chosen accordingly. The cement type chosen was normal hardening CEM II 52.5N in combination with a quartzite aggregate; similar to the cement and aggregate used for the physical tests.

Compressive strength and density, listed in Table (4.2) and determined as per Section (3.3.1) were the only characterisation tests performed for the six NWC panels (N1-N6). It was on this basis that the C40 NWC material model was selected. The remaining material properties were as the DIANA FEA default. The reader is directed to the DIANA Material Library §12.1.2 for further explanation on the implementation of this model code material in DIANA FEA DIANA FEA BV (2016c).

4.5   Rebar Mesh - Von Mises Plasticity model

A Von Mises plasticity model was chosen for the steel mesh reinforcement within the LWFC panels. Two layers of Mesh Ref.193 steel (E&OE (2017)) were simulated in the plane stress model as seen in Figure (4.19). The diameter of each mesh strand was $5.6\ mm$, formed of high yield ($520\ MPa$) steel and placed in a $200 \times 200\ mm$ grid. The reinforcement bars of $24.63\ mm^2$ cross-sectional area were doubled and formed a single layer for the 2D analysis. The square mesh was shorter than the wall panels in all directions by a

Table 4.2: *NWC characteristic compressive test results and densities for the six NWC panels.*

NWC Panel	Compressive Strength, fcu $[MPa]$	Density, p $[kg/m^3]$
N1	37	2010
N2	60	2271
N3	47	2180
N4	57	2221
N5	54	2243
N6	54	2257
Avg.	52	2197
Std. Dev.	7	82
C.o.V	14%	4%

conservative 25 mm. This ensured that the forces were initially transferred to the concrete before being resisted internally by the reinforcement.

The Von Mises plasticity model was chosen not to have plastic hardening and the values for Young's modulus and yield stress were kept the same as the Vertical and Horizontal connections, noted in Table (4.3). The values of Young's modulus ($E = 215\ GPa$) and yield stress ($\sigma_y = 520\ MPa$) were subsequently confirmed via tensile tests and the results are available in Section (5.2.2).

4.6 Bond-slip Reinforcement Material Model

The reinforcement perpendicular to the connection interfaces was modelled as bond-slip reinforcement. Apart from being evaluated specifically at the interface, the bond-slip rebar incorporated an additional interface material model, attached to the existing Von Mises plasticity model for reinforcement steel. DIANA FEA Material Library §9.3 and §26.3 detail the available non-linear relationships between shear traction t_t and shear slip $\triangle u_t$ (DIANA FEA BV, 2016*c*). For LWFC it was therefore necessary to look at the bond-slip results of De Villiers *et al.* (2017) to determine which of the bond-slip interface material models, indicated in Figure (4.12), would be most appropriate.

Figure (4.13) shows the comparison between the cubic, power law and Shima bond-slip models with reference to the conservative bond-slip results of De Villiers *et al.* (2017). The multi-linear bond-slip model was neglected in this analysis as it was seen to give unrealistic values. The cubic bond-slip model by Doerr (Dörr (1980)), of DIANA FEA BV (2016*c*)) §26.3.1, was ultimately selected with the slip parameters outlined in Table (4.3). It was a best fit to the bond-slip peak observed in the BE bond-slip tests of De Villiers *et al.* (2017).

Due to the applied lateral load at the highest point of the wall, dowel action at the reinforcement-LWFC interface was expected. It was therefore essential that the bond-slip reinforcement could provide information beyond pure axial forces and deformation. The reinforcement was therefore modelled as a circular beam of 12 mm diameter for the Y12 reinforcement. This geometric specification was important for the model where the axial orientations across the vertical and horizontal connections were specified as required in §15.7 of DIANA FEA BV (2016*b*).
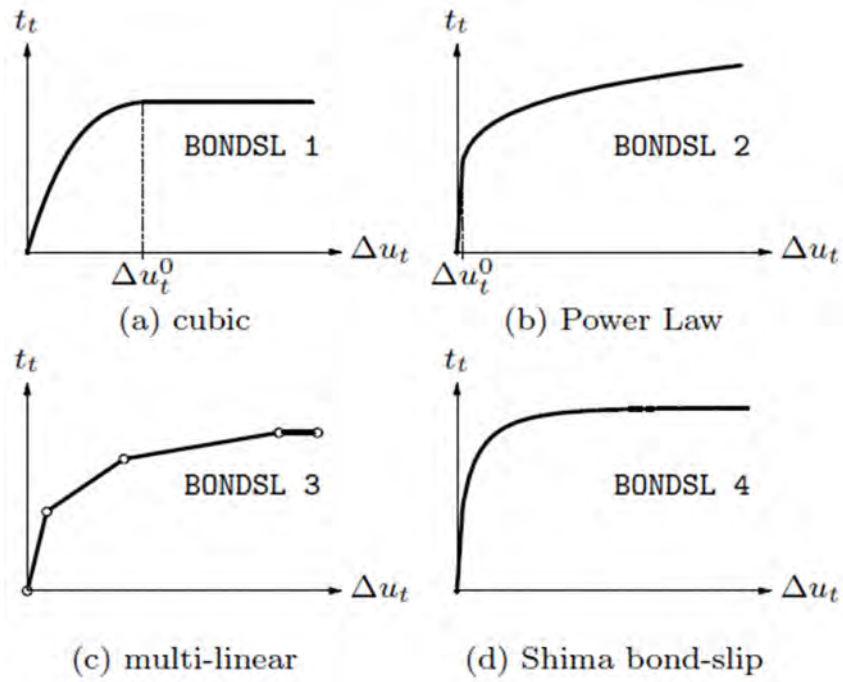
Figure 4.12: *Available bond-slip material models in DIANA FEA BV (2016c)*
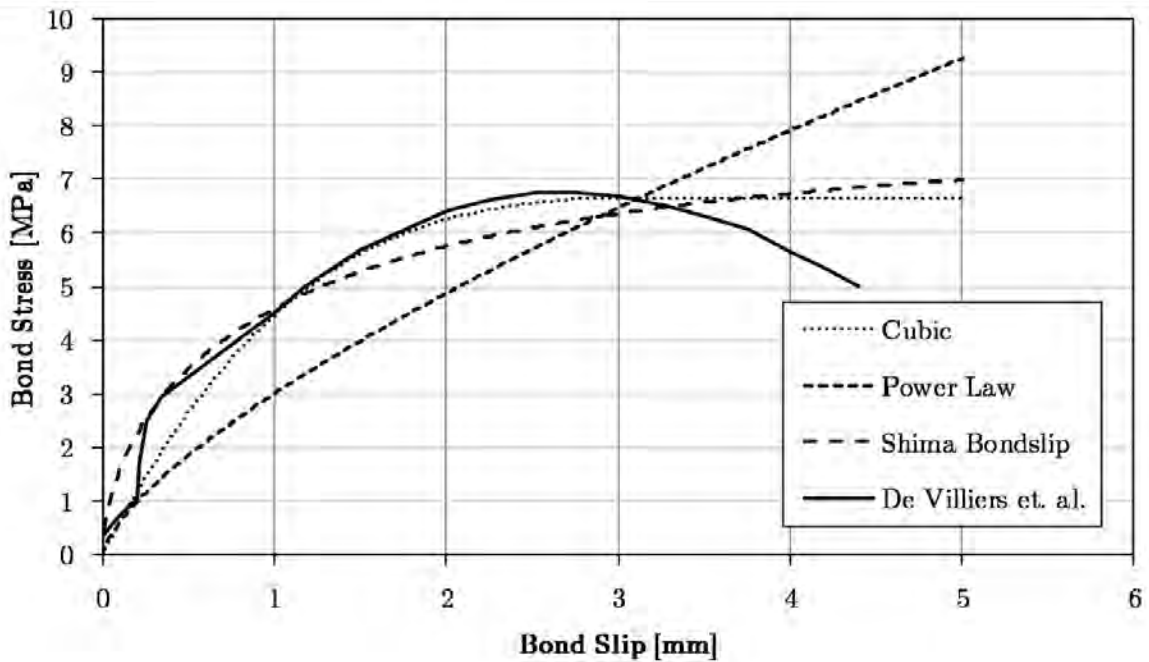
Figure 4.13: *Bond-slip model comparison with BE bond-slip tests of De Villiers* et al. *(2017)*

4.7   FE Model Parameter Summary

The material properties used to define the preliminary nonlinear LWFC material model, the reinforcement and relevant connection interfaces are summarised in Table (4.3). The updated material properties for LWFC used in the final FE models are shown in Table (5.2).

Table 4.3: *Finite element material model properties utilised for the preliminary FE model (DIANA FEA BV (2016c)).*

LWFC Panel: Total strain rotating crack model			
Young's Modulus,E [GPa]	8.16	Fracture Energy, G_f [N/m]	69.3
Poisson's Ratio, ν	0	Density, ρ [kg/m^2]	1400
Tension: Hordijk		**Compression: Maekawa**	
Tensile Strength, f_{tu} [MPa]	1.41	Compressive Strength, f_{cu} [MPa]	12.5
Horizontal and Vertical Connections: Von Mises Plasticity Model			
Young's Modulus, E [GPa]	210	Yield Stress, σ_y [MPa]	520
Steel Density, ρ [kg/m^3]	7850	Hardening Function	None
Horizontal and Vertical Connections: Bond-slip Interface			
Area, A [mm^2]	113.1	Y12 Rebar, Diameter [mm]	12
Normal Stiffness Modulus [N/m^3]	$1.3392e10$	Shear Stiffness Modulus [N/m^3]	$1.3392e9$
Bond-slip Interface Failure Model			
Parameter C, [N/m^2]	$3.5e9$	Shear slip at start [m]	0.0028
Grid Reinforcement			
Bar Diameter x [m]	0.0112	Bar Diameter y [m]	0.0112
Bar spacing x [m]	0.2	Bar spacing y [m]	0.2
Horizontal and Vertical Connections: Frictional Interface Material Properties			
Interface Type	2D Line	Opening Model	Gapping, brittle, zero tension
Normal Stiffness Modulus [N/m^3]	$5.44e10$	Shear Stiffness Modulus [N/m^3]	$2.72e10$
Coulomb Friction model at connections			
Cohesion [N/m^2]	0	Friction Angle [deg]	45
Dilatancy Angle [deg]	0		

4.8   Preliminary FE model

Before finalising the physical test, a preliminary FE model was constructed that made use of the the preliminary nonlinear LWFC material properties developed in Section (4.2). These preliminary LWFC material properties and simpler FE model were based entirely on the theoretical work of Grafe (2017) and De Villiers *et al.* (2017).

The meshed and unmeshed configuration of the model is shown in Figures (4.14) and (4.15). At this point the physical test setup was not finalised and it was important to understand the expected test results. Thus, no allowance was made for the physical test setup where the lateral load was applied via structural steel section and the self-weight of the wall.

For this preliminary model the entire three storey weight was applied as a distributed load at the top of the wall and the lateral pull-over load was applied as a distributed displacement across this surface.
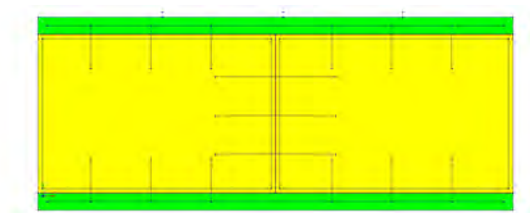
Figure 4.14: *Initial FE model: un-meshed*
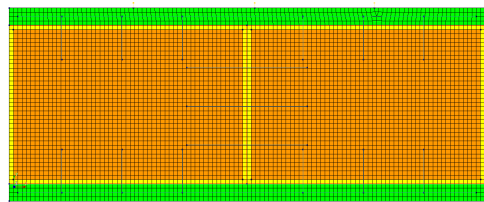
Figure 4.15: *Initial FE model: meshed*

The comparative results of the global displacement for both the models of PST 1 and PST 3 are shown in Figure (4.16). These initial results show only a single "failure" of the model, where the substantial peak drop in the graph is the point at which slip failure is observed at the top horizontal connection. The abrupt stoppage of the load curve and plateau for both FE models is due to the limited 4 *mm* displacement applied to the wall.

After analysing the physical tests in Section (5.1) it was seen that two distinct failure regions occurred where initial lifting and rotation was followed by slip at the top horizontal connection. An improved FE model that would allow for both these failure mechanisms was therefore required. Updated LWFC properties, measured from characteristic testing as well as the exact laboratory setup were therefore used to gain more convincing numerical simulation results in the following section.
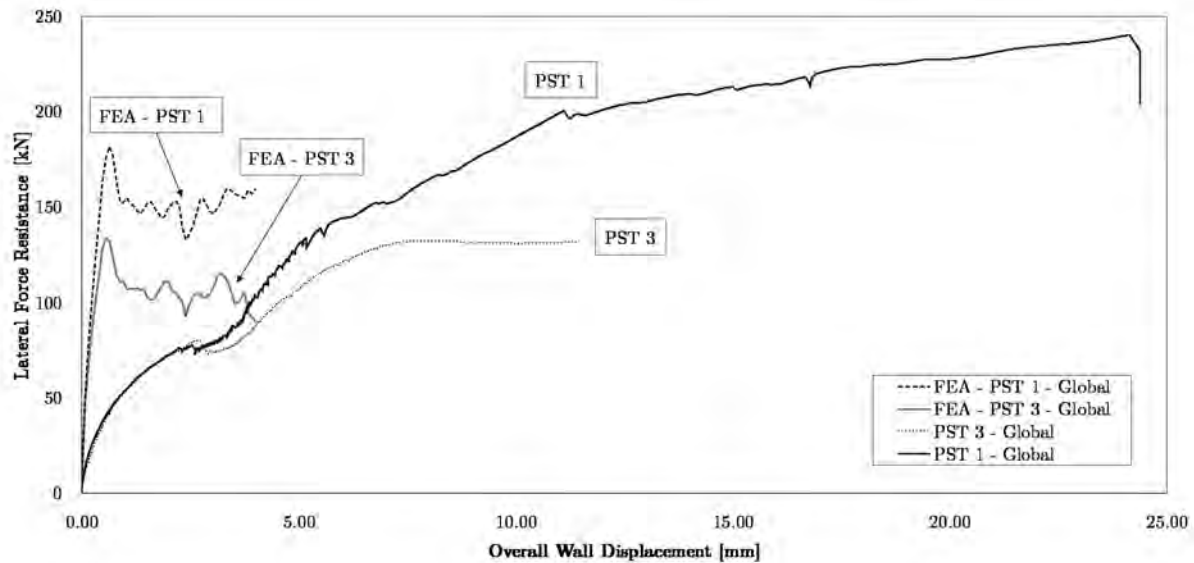
Figure 4.16: *Initial numerical model analysis results for global displacement of PST 1 and PST 3*

4.8.1   Preliminary FE Model: Results

Preliminary FE test results were gained from the developed FE model and were taken into consideration for the physical tests and test setup. Through these preliminary models, the behaviour of the connections and expected deflection was better understood prior to testing. This also provided a limit for maximum expected horizontal force at pull-over of approximately 200 kN, used for control and sanity checks during the physical tests.

The preliminary models did not include the full test setup of springs and structural steel member and therefore differ in magnitude and shape to the force-displacement curves explained in Section (5.3).

The preliminary FE model helped confirm the method of load application in the physical tests. In the FE model the lateral displacement was applied as a distributed load across the top of the wall and full load transfer was observed in contrast to shearing or local failure.

4.8.2   Preliminary FE Model: Sensitivity Study

A sensitivity study was conducted to gauge the effect of global connection configuration on the force-displacement response of the preliminary FE model. The top and bottom horizontal connections varied between 6 and 4 grouted rebar and there were a maximum of three connection boxes, simplified by bond-slip rebar, across the vertical connection. The test matrix combinations are summarised in Table (4.4) and the force-displacement curves are plotted against the output of PST 1 and PST 3 in Figure (4.17).

The results of Figure (4.17) indicate the general trend in response for both PST 1 and PST 3 and their FE model equivalents. For these models a decrease in horizontal connection number leads to a decrease in stiffness and a lower peak lateral force resistance.

The reduction of vertical connection boxes leads to an increase in the lateral force resistance and contrasts with the hypothesis: a less connected wall is weaker. A possible reason for this result is that the wall is still well connected at the horizontal connections and

Table 4.4: *Structural sensitivity connection test matrix*

		Horizontal Connection Rebar, H	
		6	**4**
Vertical Connection Boxes, V	**3**	6H 3V	4H 3V
	2	6H 2V	4H 2V
	0	6H 0V	4H 0V
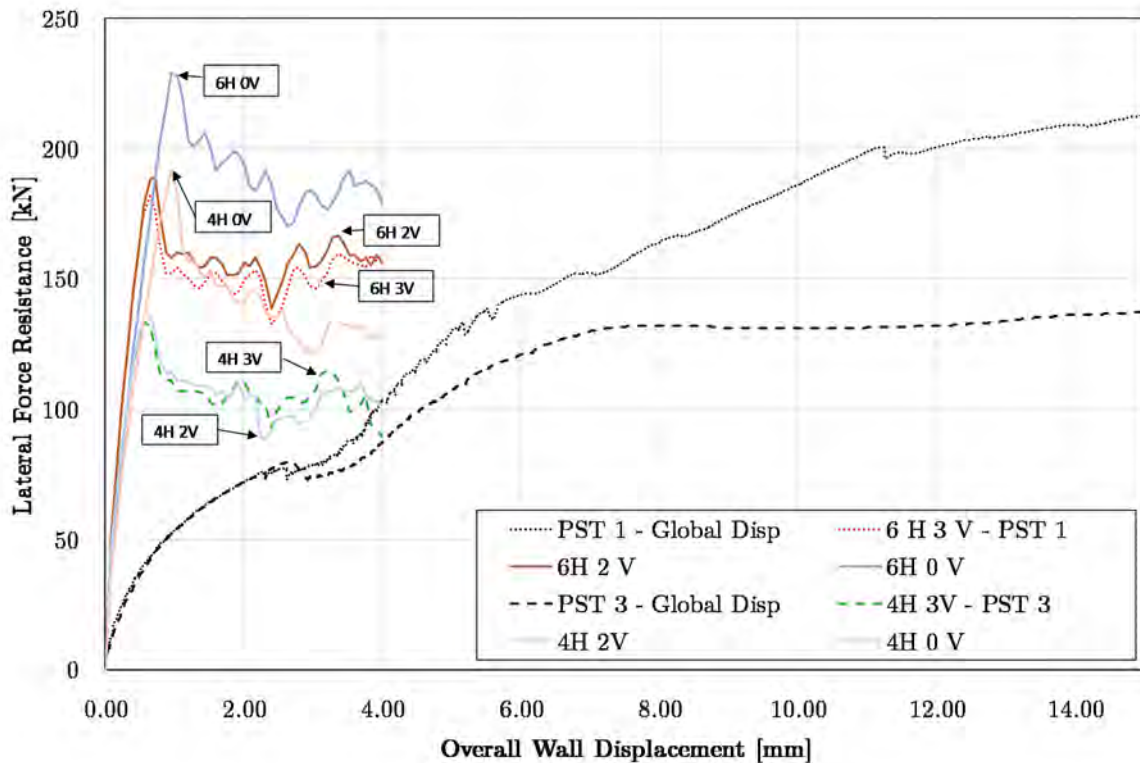
Figure 4.17: *Configuration of the structural design through changes in connection number and location*

thereby able to remain in-plane throughout the plane-stress analysis. It is however unlikely that these connections could be neglected; as out-of-plane movement due to a slightly eccentric vertical connection would be unrestrained and likely lead to the partial collapse of a structure.

The conclusion of this a sensitivity study was that the number of horizontal connections has a significant impact on the behaviour of a wall and that including this as a variable in physical testing would be important.

4.9 Finite Element Model Development

The un-meshed FE model shown in Figure (4.18) represents the numerical approximation of the physically tested model. Here two rectangular LWFC panels are sandwiched in between two NWC beams, connected via vertical rebar dowels at horizontal connections and horizontal, anchored rebar at the vertical connection. The load applicator $254 \times 254 \times 89$

structural steel section and end plate are shown in the model atop the wall.

The wall dimensions and specifications are sketched in Figure (4.19) which shows the concrete elements of the standalone connected wall and indicated reinforcement for physical scale test (PST) 1.
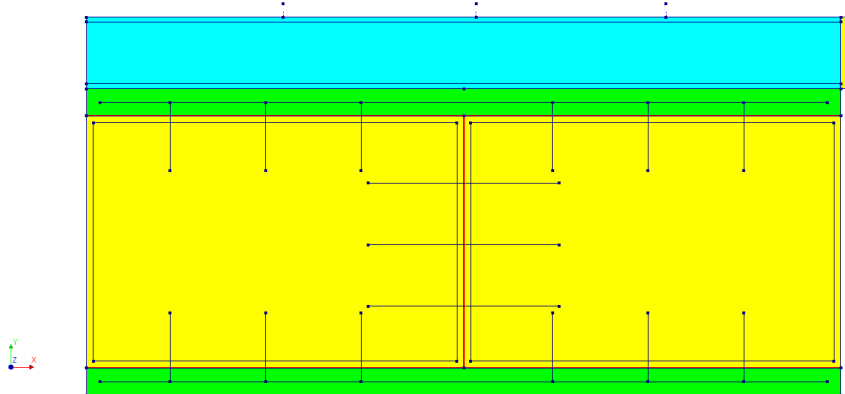
Figure 4.18: *Un-meshed FE Model*
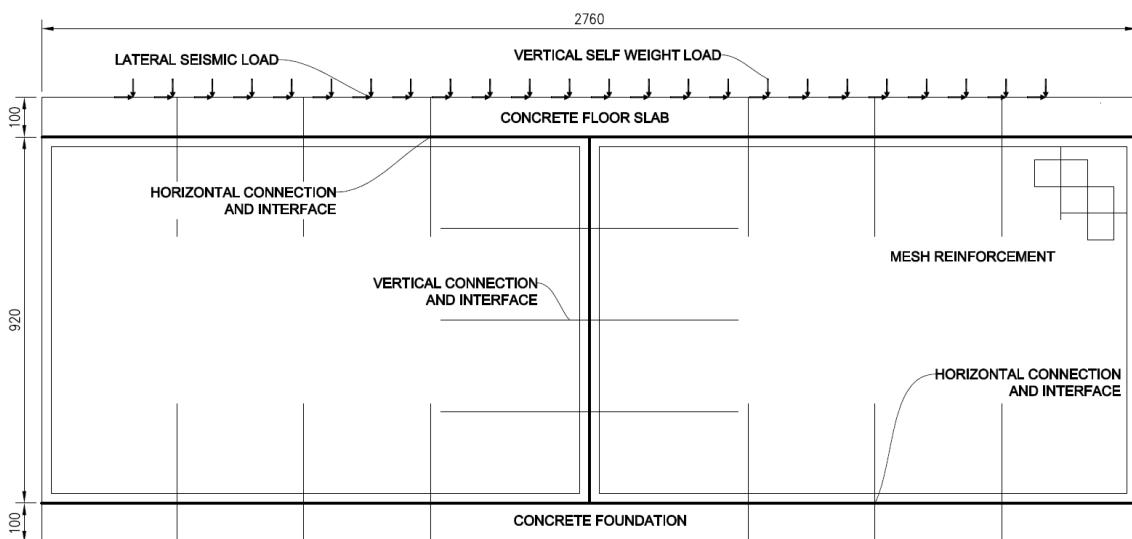
Figure 4.19: *Dimensioned preliminary FE Model*

4.9.1   Connection Simplification

The physical test connections of Figure (4.20) were simplified for the numerical model. Both the vertical connection boxes and grouted rebar horizontal connections were modelled as bond-slip rebar. The model allowed for expected dowel action of the rebar at the connections through evaluation of the rebar at the interface.

Vertical Connections

Due to the resolution of the 2.76 $m \times$ 0.92 m LWFC wall panel in comparison to the 100 mm-cube connection boxes at the vertical connection, it was decided that a bond-slip rebar across the vertical connections would be used in place of a detailed connection box
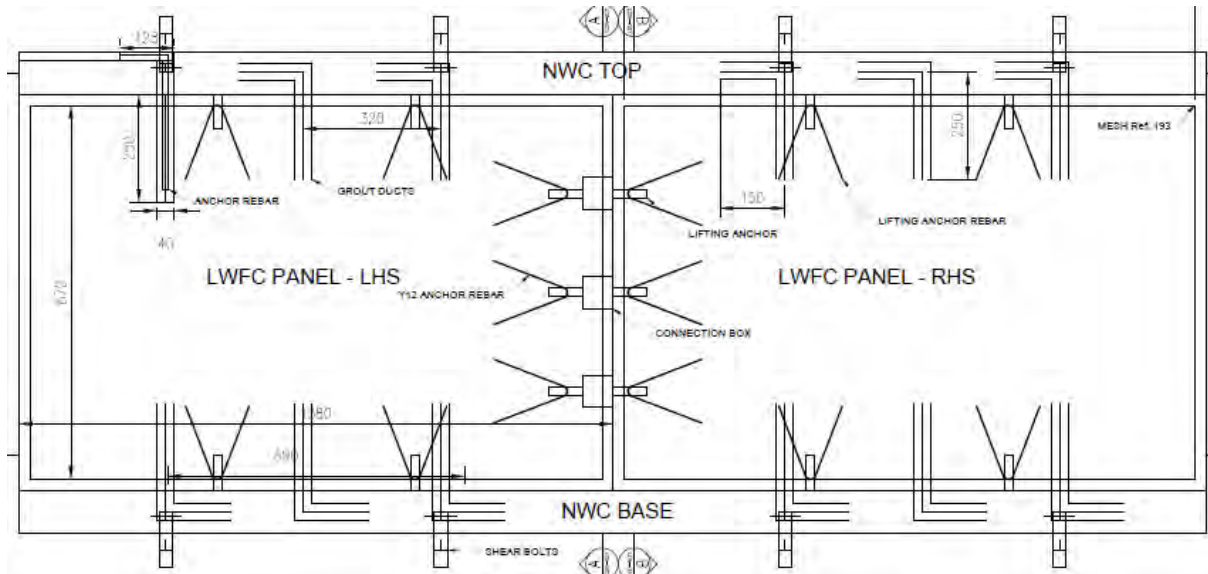
Figure 4.20: *Wall connections of physical tests, a portion of the larger layout in Appendix B.*

model.The simplification was deemed satisfactory as the equivalent shear area was similar between the numerical model and physical test setup.

The length of the rebar on either side of the connection was 350 *mm* and similar to that of the physical tests. The characteristic test output of the connection boxes is presented in Section (5.2.3).

Horizontal Connections

The horizontal connections were represented by reinforcement across the interface between the NWC and LWFC panels. The rebar length terminated at the centre of the 100 *mm* thick NWC panel and protruded 200 *mm* into the adjoining LWFC panels. Due to adequate numerical bond simplification along the bond-slip rebar, it was decided not to model the hook of the rebar required for physical testing.

4.9.2 Boundary Conditions

Boundary conditions and axis orientation of the FE model are indicated in Figure (4.21). These boundary conditions are explained for the reinforcement has been neglected. For the model it was assumed that the base of the walling unit was fixed for lateral and vertical movement. Additionally, due to the applied lateral displacement load, the lateral translation degree of freedom (x) was fixed at the yellow end-plate on the far side of the turquoise structural steel section.

4.9.3 Applied Loads

Sustained Vertical Load

The sustained vertical load applied to the FE wall model was as calculated for the physical testing in Section (3.2.3). Account was taken of the now weight-less springs in the FE model to obtain an accurate sustained vertical load of 12.36 *kN/m* along the top of the wall.

Figure 4.21: *Applied loads and boundary conditions for FE model, shown generically for the model of PST 1.*

Self-Weight

Self-weight of the wall and structural steel load member atop the wall was applied as a gravity load from the centroid of each element. The mass of the materials were individually specified and gravitational acceleration was 9.81 m/s.

Lateral Displacement

Displacement control of the physical tests was replicated in the FE model through an applied displacement load. The load was applied as a general displacement at the centre of the structural steel member through an attached, rigid end-plate (Figure (4.18)). To allow numerical integration and convergence, no time rate was specified for the lateral load. Automatic load step determination was enabled, where DIANA FEA apportioned the total applied 8 mm displacement incrementally. The maximum step increment was a 0.012 fraction of this displacement per step.

4.9.4   Vertical Restraint Load Springs

In order to replicate the increase in spring force observed during physical testing, three 100 mm grounded springs were attached along the top of the structural steel section. The springs are noted as fine lines at the centre of each LWFC panel and at the centre of the wall, atop the structural steel member in Figure (4.21). The stiffness of these springs was derived from the vertical deflection and spring force increase in PST 1, determined to be approximately 85 kN/mm per spring pair.

Multiple numerical models were attempted and spring forces were selected for PST 1 and PST 3 that best represented the global spring force behaviour observed during physical testing. A spring pair force of 200 kN/mm was chosen for PST 1 and 100 kN/mm for PST 3. The comparison between the physical and numerical spring forces are shown in Section (5.1.4).

4.9.5   Finite Elements

DIANA FEA elements used for the analyses are described in this section. The elements for each model section varied between the physical quadrilateral elements: Q8MEM for solid

steel and concrete, the nodal point elements PT3T for the ground points of the springs, the bond-slip reinforcement interface elements T6MEM, SP2TR spring elements and the line interface elements L8IF DIANA FEA BV (2016*b*).

The degrees of freedom of Q8MEM, PT3T, T6MEM and SP2TR elements are indicated in Figures (4.22), (4.23), (4.24) and (4.25) respectively. Inter-facial line element L8IF is referred to in Section (4.3) and Figure (4.11).
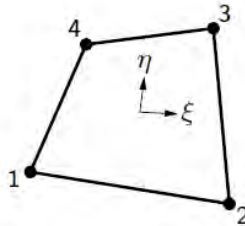
Figure 4.22: *Quadrilateral, isoparametric plane-stress material element Q8MEM, detailed in §5.7.2 of DIANA FEA element library (DIANA FEA BV, 2016*b*).*
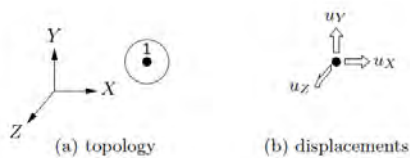
Figure 4.23: *Topology (a) and displacement (b) degrees of freedom for single-node translation damping element, PT3T, detailed in §14.4.1 of DIANA FEA element library (DIANA FEA BV, 2016*b*).*
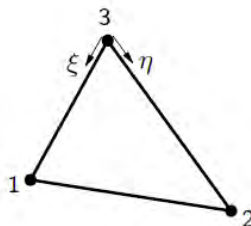
Figure 5.11: T6MEM

Figure 4.24: *Three node triangular, isoparametric plane-stress material element T6MEM, detailed in §5.7.1 of DIANA FEA element library (DIANA FEA BV, 2016*b*).*
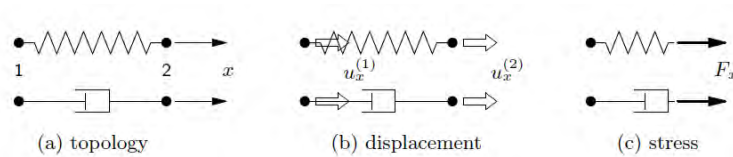
Figure 4.25: *Topology (a), displacement (b) and stress (c) degrees of freedom for two-node translation spring element, SP2TR, detailed in §14.1.4 of DIANA FEA element library (DIANA FEA BV, 2016b).*

4.9.6 Maximum Element Size

According to Van Zijl (2000), the maximum element area to prevent "snap-back" in the elements is given by Equation (4.5). For the developed FE model and sensitivity studies presented, it would be important to ensure that this maximum element size is not exceeded. Curiel-Sosa *et al.* (2013) define the snap-back phenomenon as a turning back of the load-displacement curve. This is noticed by a sharply decreased load due to a reduction in displacement after reaching an initial peak value.

$$h_e \leq \frac{G_f \cdot E}{f_t^{\,2}} \tag{4.5}$$

Where:

G_f is the fracture energy of the material
E is the Young's modulus of the material
f_t is the tensile strength of the material
h_e , the element size, typically taken as $h_e = \sqrt{A_e}$
where A_e is the element area

4.9.7 Mesh Configuration

A global mesh, seeded by size of $25 \times 25\ mm$ was chosen for the model. Seeded line-interface elements were therefore 25 mm long. The meshed elements are shown and described in Figure (4.26).

4.10 Evaluation Procedure

The multiple applied loads and required supports necessitated a phased nonlinear DIANA FE analysis as explained in §14.2 of DIANA FEA BV (2016*a*).

In the first phase; only the sustained vertical and self-weight loads were applied. A nonlinear secant (BFGS) analysis proceeded until convergence of energy, force and displacement norms were achieved. During this phase the required restraints at both the point of lateral displacement as well as the grounding points of the springs were deactivated (Figure (4.21)). These supports were deactivated to ensure a full application of the vertical, self-weight and sustained vertical loads and to eliminate incorrect reaction forces at these supports.
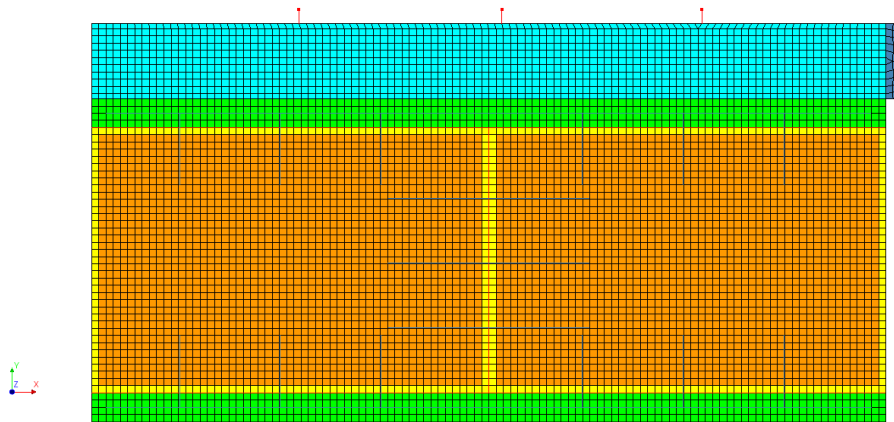
Figure 4.26: *Mesh configuration for PST 1, indicating the coarse mesh and elements of structural steel member: turquoise, steel end-plate: dark blue, LWFC panels: yellow, NWC panels: green, Steel reinforced LWFC: orange, steel reinforcement: blue, interfaces: red, springs: thin red lines (on top).*

Phase 2 of the analysis followed the same integration scheme and evaluation criteria. Continuing from phase 1, the applied stress and load was maintained and the lateral displacement load was applied. In addition, the grounded vertical springs and lateral displacement supports were activated (Figure (4.27)). After the full lateral displacement was applied and all load-steps converged, the second and final analysis phase was concluded.

Due to the nonlinear material behaviour it was necessary to allow for 300 integration attempts per load step.

Figure 4.27: *Applied loads and boundary conditions for FE model, Second phase shown generically for the model of PST 1.*

Chapter 5

Results

This chapter unpacks and explains the results from both the physical scale tests and numerical finite element analyses. The physical test results are initially interrogated individually. Thereafter the characterisation test results are explained and incorporated into the final finite element (FE) model. A FE model sensitivity study is conducted to show the effect of changing either the physical test configuration or the LWFC material properties to obtain a completed understanding of this structural design method. The chapter is concluded by providing a seismic resistance comparison after analysing specific results from both tests in more detail.

5.1 Physical Scale Tests

This section details the results of the physical tests performed in the Stellenbosch University structural engineering laboratory. Three different tests were performed on three different walls. Physical scale test(s) (PST) 1 and 2 were performed on a complete wall and the test method differed between the two. PST 3 was a repeat of PST 1 with a slightly modified structural design, by reducing the number of connecting dowels along horizontal joints.

Displacement of the wall was measured at various points as per the LVDT arrangement in Figure (3.21). Global displacement is considered as the overall displacement of the wall including the top and bottom NWC panels, measured by the difference in LVDT readings A and D of Figure (5.1). In contrast to this, local displacement is the displacement of the LWFC panels themselves, measured by the difference in LVDT readings B and C of Figure (5.1). In addition, positive displacement was decided to be in the pull-over direction for movement towards and with the Instron MTM.

5.1.1 PST 1

Test Procedure

Physical Scale Test 1 was conducted as a uniform pull-over (monotonic) test in accordance with the JRC Scientific and Policy Report (Negro and Toniolo, 2012). For this test a fully connected wall had three vertical connection boxes and six grouted rebar at the horizontal connections of each LWFC panel. The wall was pulled over in accordance with the loading
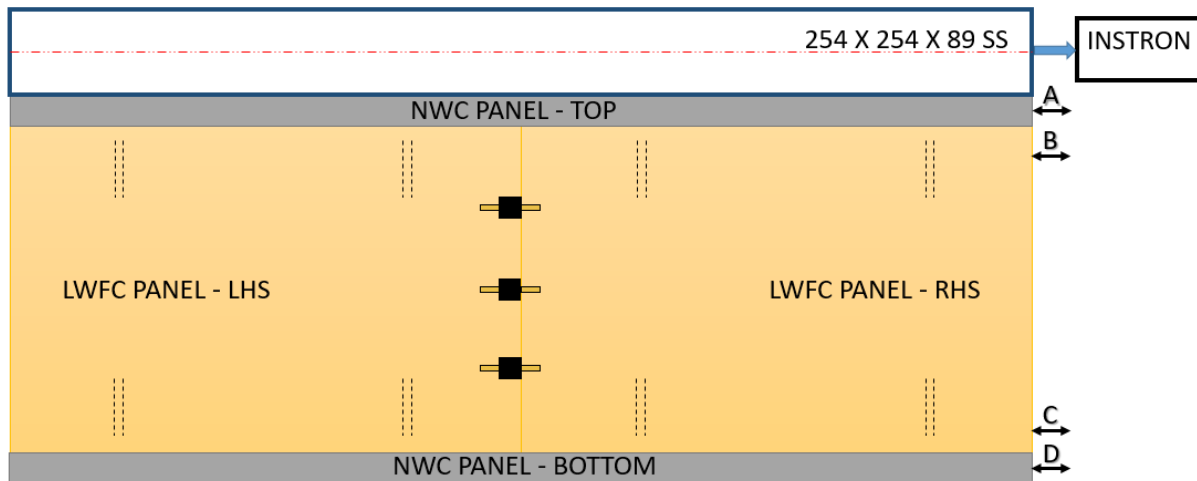
Figure 5.1: *Schematic showing global and local displacement of the LWFC wall PST.*

and boundary conditions of Section (3.2.5). The wall configuration was that of preliminary FE model 6H3V in Section (4.8).

Results

This initial test formed the basis for PST 2 and PST 3 as it was the first test in the laboratory setup. The load was applied via displacement control and the results for global and local displacement can be seen in Figure (5.2). The wall was not tested until failure but was tested until the stroke limit of the Intron MTM was reached. Thereafter the displacement load was reversed and the wall was pushed until again reaching the stroke limit. Finally the test was stopped at the point of zero lateral force resistance. Within these test limits considerable displacement was however observed. In Figure (5.2) the reader should note that permanent deformation has taken place as final displaced position is not at the (0,0) starting point on the force-displacement curve.

Interpretation

Upon further investigation of the force-displacement curve for PST 1, it was seen that distinct regions of non-linear displacement occur. From the time-lapse photography taken during the test it was noted that these displacements related to differing movements of the wall assemblage. For PST 1 there were four regions of non-linearity which are highlighted in points one through four in Figure (5.3) and are summarised as follows.

1. Cracking along the mortar joint at the bottom horizontal connection (Figure (5.4)).

2. Lifting at the left-hand side and rotation of both LWFC panels (Figure (5.5)).

3. Individual panel movement where for PST 1 it was observed that each panel began to rotate separately (Figure (5.6)).

4. Notable slip at the top and bottom horizontal connections once panel lifting and rotation reached a limit (Figure (5.7)).

Due to the lateral load at the wall height above the upper horizontal connection, it was expected that tensile forces from the moment arm developed would create a crack at this
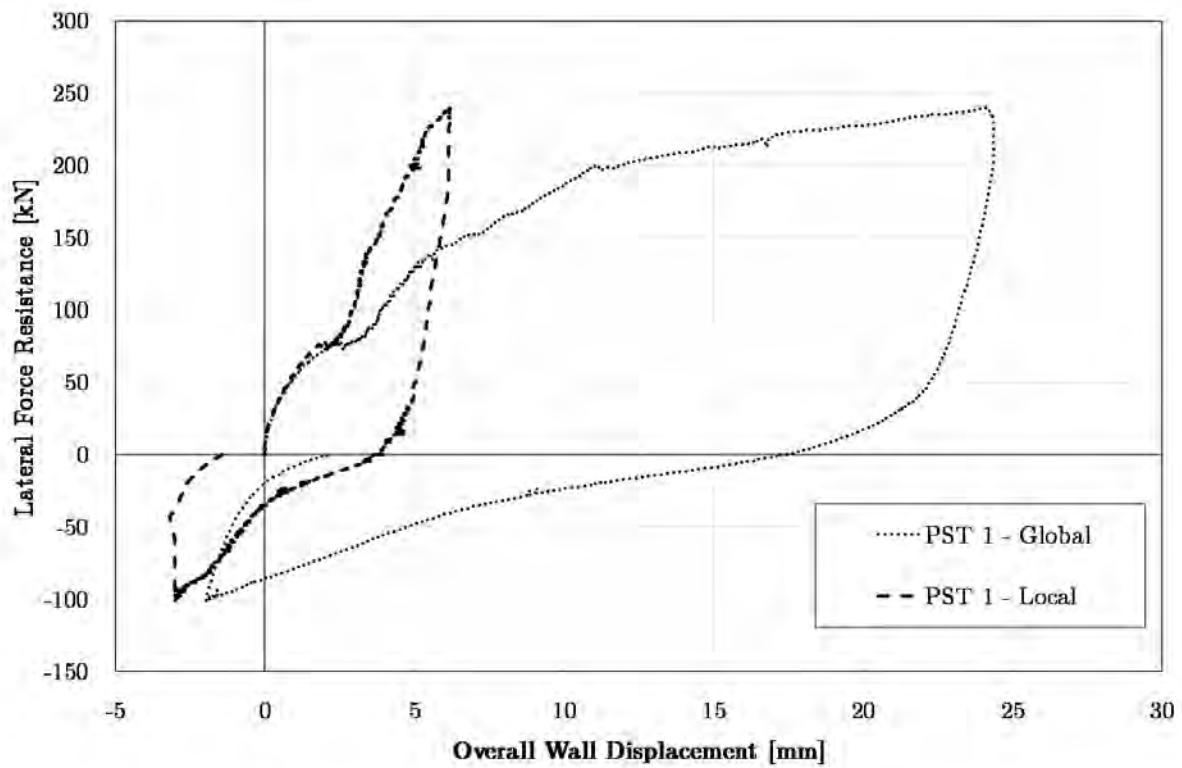
Figure 5.2: *PST 1: Force-displacement curve results for global and local displacement.*
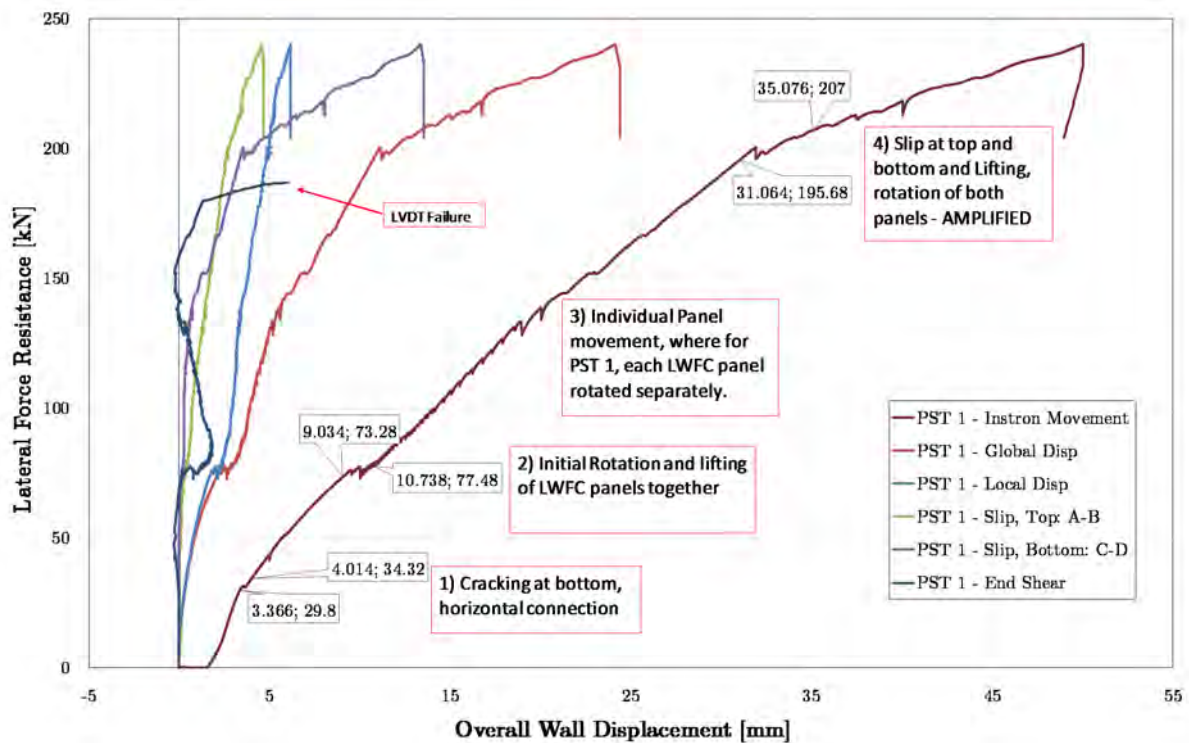
Figure 5.3: *Physical interpretation of the ascending pull-displacement of PST 1, Figure (5.2)*

Figure 5.4: *PST 1: First nonlinear displacement region, cracking along the lower horizontal connection.*

Figure 5.5: *PST 1: Second nonlinear displacement region, lifting at the LHS and global panel rotation.*

Figure 5.6: *PST 1: Third nonlinear displacement region, continued lifting on the LHS and individual panel rotation.*

Figure 5.7: *PST 1: Fourth nonlinear displacement region, notable lateral slip at the top horizontal connection - indicated by localised cracking.*

connection. This initial failure point is noted in Figure (5.4). As the lateral load increased, the wall lifted at the left-hand, far side and rotated in it's attempt to resist the internal shear forces (Figure (5.5)). This, second nonlinear displacement was further amplified by the individual panels' movement. After a certain lateral displacement, a slight vertical displacement between the panels at the central, vertical connection was observed (Figure (5.6)). This third differential displacement at the vertical connection allowed the panels to rotate individually and is viewed as a positive design feature. It is hypothesised that the reason for this individual panel movement is the symmetry of vertical (three) and horizontal connection (three per NWC panel, six per LWFC panel) numbers for PST 1. In contrast, this displacement was not observed for the unsymmetrical horizontal (two) and vertical (three) connections per LWFC panel in PST 3. The final displacement in Figure (5.7) is likely the result of a combination of yielded rebar and crushed concrete / grout at the horizontal connections where slip occurred. This displacement region was easy to see in the time-lapse photography. The grouted connections are considered to be the final limit before exaggerated slip displacement occurs.

5.1.2   PST 2

Test Procedure

Physical Scale Test 2 followed the recommendations for quasi-static, cyclic testing in the JRC Scientific and Policy Report (Negro and Toniolo, 2012) and relied on the results observed for PST 1. This test followed PST 1, had the same structural connections between the precast panels and the same sustained vertical load. The displacement was however now applied in push-pull cycles of increasing amplitude in contrast to pull-over. The wall configuration was that of preliminary FE model 6H3V in Section (4.8).

Following the JRC Report: Δ_y was chosen as 10 mm from Figure (5.2). This Δ_y value was selected as an average displacement value between local and global wall displacement at the elastic limit. From this displacement, a load sequence was initiated as detailed in Table (5.1) where the first displacement d_1 was 2.5 mm, a quarter of Δ_y and was increased by $\Delta_y = 10$ mm for each of the subsequent loading groups and applied at a constant rate of 10 mm/min.

Table 5.1: *Load cycle groups according to JRC Report (Negro and Toniolo, 2012). Constant displacement load applied at* 10 *mm/min for all three cycle groups.*

Group	Amplitude [mm]	Distance [mm]	Period [S]	Frequency [Hz]
1	2.5	10	60	0.0167
2	12.5	50	300	0.0033
3	22.5	90	540	0.0019

The displacement-time graph of the applied cyclic displacement is shown in Figure (5.8) in combination with the measured global and local wall displacements. It was seen that a delay or "lag" in displacement occurred between these values for each half-cycle. This displacement lag can be seen as the difference in amplitudes of the Instron, global and local displacement for the cyclic tests in Figure (5.8). Further, as a result of observed slippage in the test setup, PST 2 was stopped prematurely after three successful groups of three cycles each and the wall was again not tested till failure as prescribed in the JRC report. The cycle sets have been named Groups 1-3.
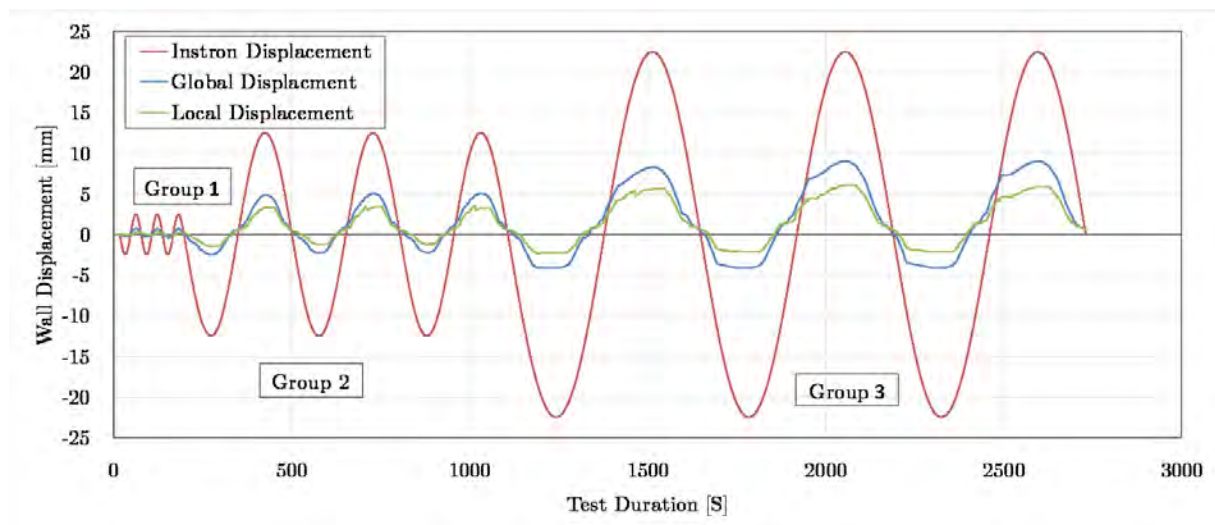
Figure 5.8: *PST 2: Instron vs overall wall displacement applied through cyclic loading according to JRC Scientific and Policy Report (Negro and Toniolo, 2012).*

Results

As per the requirements of the JRC report, the force-displacement loops for each cycle group are shown separately in Figures (5.9), (5.10), (5.11). These cycles are shown for global displacement only.

It must be noted again that the expected amplitude was not achieved due to the lag in the system and the stiffness of the wall; this wall stiffness would have to be overcome for global and local displacement to occur. It must also be understood that the Instron displacement is the programmed, input displacement for each load cycle, the maximum possible displacement, and was not measured via LVDTs. The lag between the applied Instron displacement and the resultant global displacement was due to a lack of stiffness in the physical test setup. Bolt-hole tolerances of $\pm\,2\,mm$ and deflection of the structural

steel members as well as the load application bars of Figure (3.16) limited completed load application. The force displacement response was assumed to follow similarly to that of PST 1.

The varying amplitude cycles shown over time in Figure (5.8) influenced these hysteresis loops where the negative push displacement was less than the positive pull displacement for the Instron cycle amplitude. This in turn resulted in a decrease in energy dissipation for the push half-cycles.
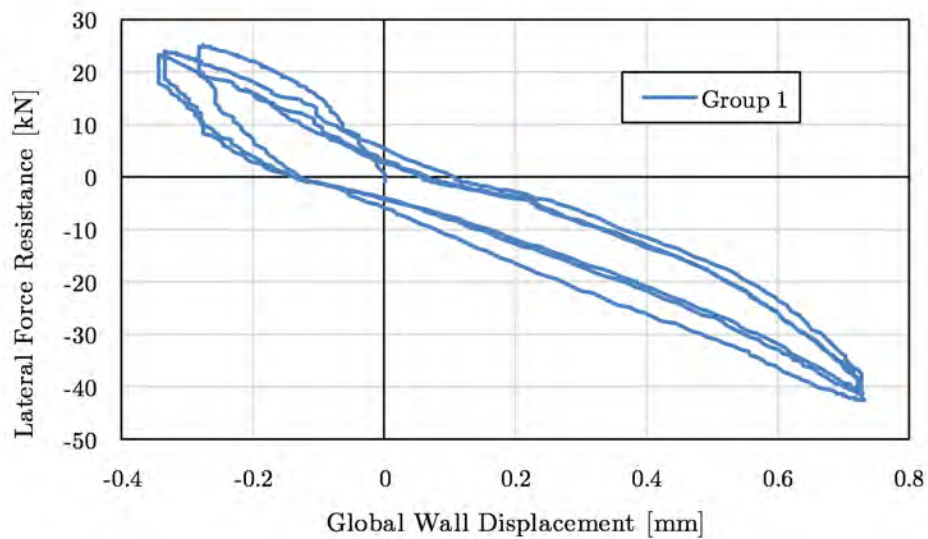
Figure 5.9: *PST 2: Force-displacement cycle group 1, amplitude of* 2.5 *mm*
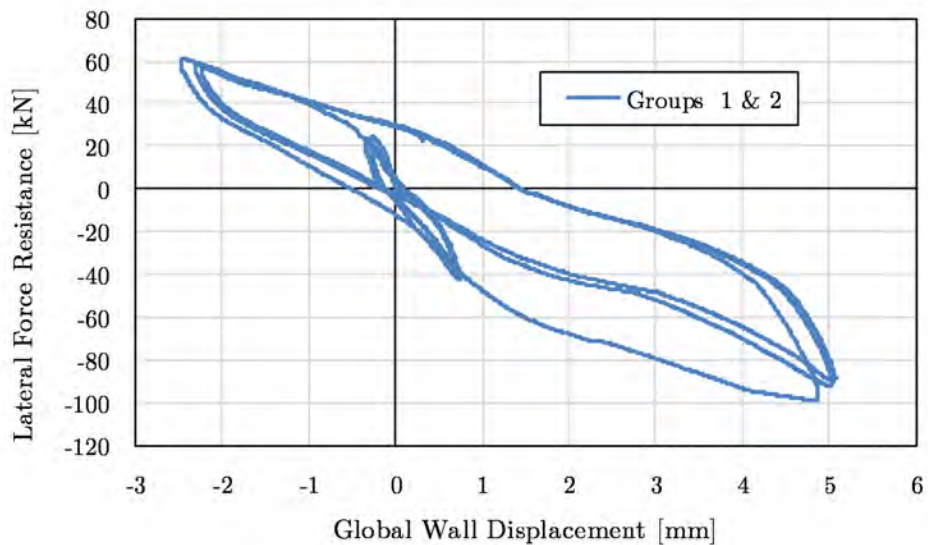
Figure 5.10: *PST 2: Force-displacement cycle groups 1 and 2, amplitude for cycle 2 of* 12.5 *mm*

Energy dissipation histograms further explain the energy dissipation potential of the walls. Figures (5.13) and (5.14) give value to the energy dissipated per half cycle, calculated according to the JRC Scientific and Policy Report Appendix A: Protocol for Connection
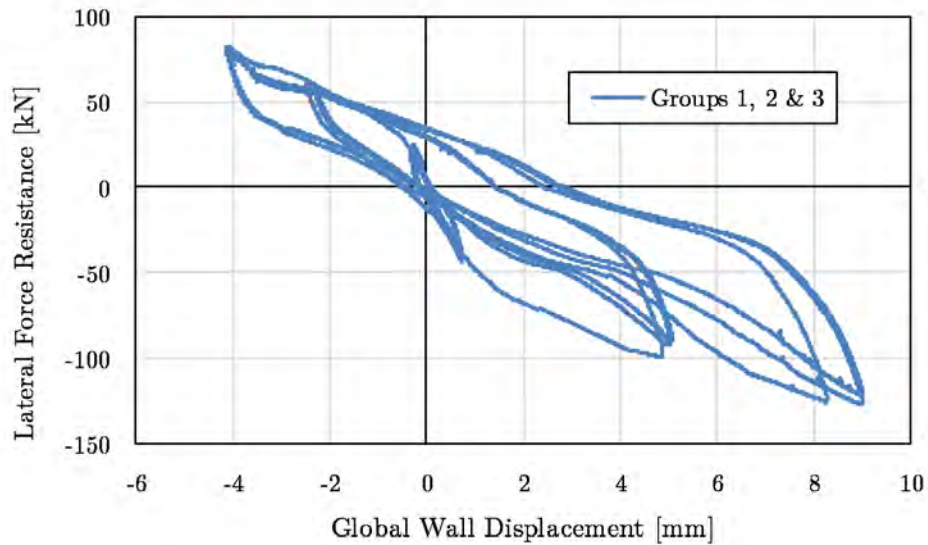
Figure 5.11: *PST 2: Force-displacement cycle groups 1, 2 and 3, amplitude for cycle 3 of 22.5 mm*

Testing (Negro and Toniolo (2012)) as the "area of the corresponding i'th branch of the force displacement diagram", U_i.

For comparison the dissipated energy U_i is converted into dimensionless, specific energy (u_i) through division of the area corresponding with the area of the elastic-plastic half-cycle (Negro and Toniolo, 2012); Equation (5.1).

$$u_i = \frac{U_i}{U_{oi}} \tag{5.1}$$

Where:
$U_{oi} = d_{pi} \cdot f_{i,max}$ and d_{pi} is the peak half-cycle displacement and $f_{i,max}$ the maximum force for an arbitrary half-cycle of Figure (5.12).
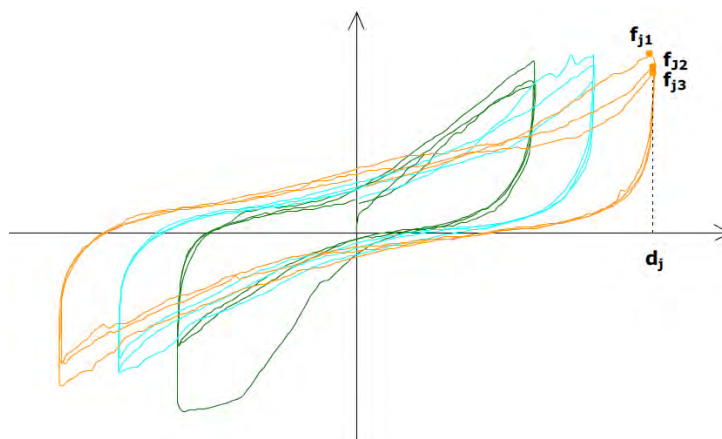
Figure 5.12: *Arbitrary force-displacement diagram for energy dissipation calculation (Negro and Toniolo, 2012)*

Figures (5.13) and (5.14) give value to the energy dissipated per half-cycle for local and global wall displacement respectively. The odd half-cycles are the less displaced push-cycles and show a decreased energy dissipation.
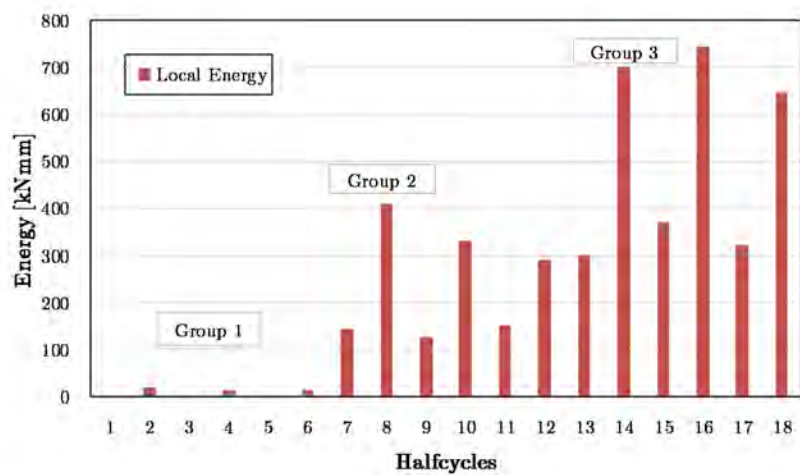
Figure 5.13: *Energy dispersion histogram for local LWFC wall displacement*
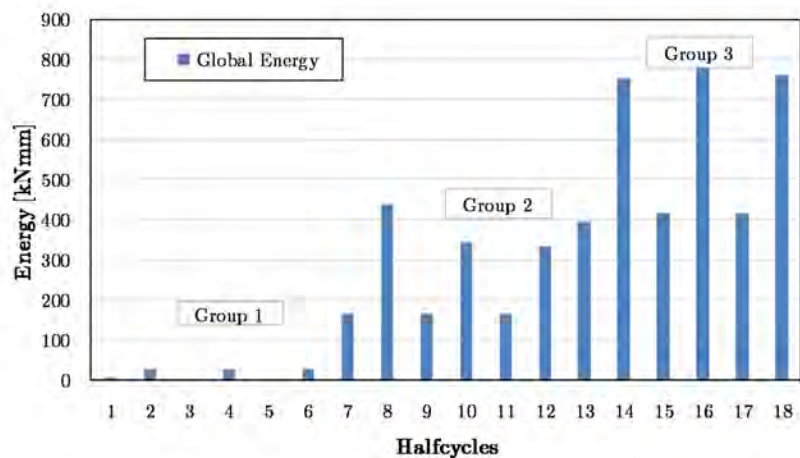
Figure 5.14: *Energy dispersion histogram for global LWFC wall displacement*

Interpretation

Both local and global energy dissipation results are shown in Figure (5.15) as non-dimensional, specific energy for each half cycle. It is thought that the difference in global and local displacements and hence energy dissipation for each cycle are related to the connections of the wall. The local energy dissipation is likely dependant on the vertical connection between the two LWFC panels and the individual panel's ability to move within the NWC floor and ground slabs. The larger global energy dissipation is likely linked to the greater displacement at the horizontal connections.

By comparing the specific energy of each half-cycle one is able to note the relatively consistent global energy dissipation where half-cycle two, nine and fifteen from cycle groups 1,2 and 3 are within a tolerable range of one another. This global dissipation can

be contrasted with the specific local energy dissipation in Figure (5.15). For this local displacement there is a definite increase in energy dissipation for the higher amplitude cycles - an indication of the change in local failure of the LWFC wall panels.

In comparison to PST 1 there is a better correlation for local and global displacement for PST 2. This is likely due to the lower forces exerted on the wall in PST 2; peaking at 127 kN in comparison to the 240 kN lateral load of PST 1. Here the wall remained in the more elastic region of PST 1, noted between explanation points 1 and 3 of Figure (5.3).

Designing a LWFC building for adequate energy dissipation during an earthquake will require a balance of stiffness between the local and global displacements. Constructing a wall that allows for only global or local displacement will therefore make inadequate use of the energy dissipation mechanisms within the wall and a combination of both should be ensured.
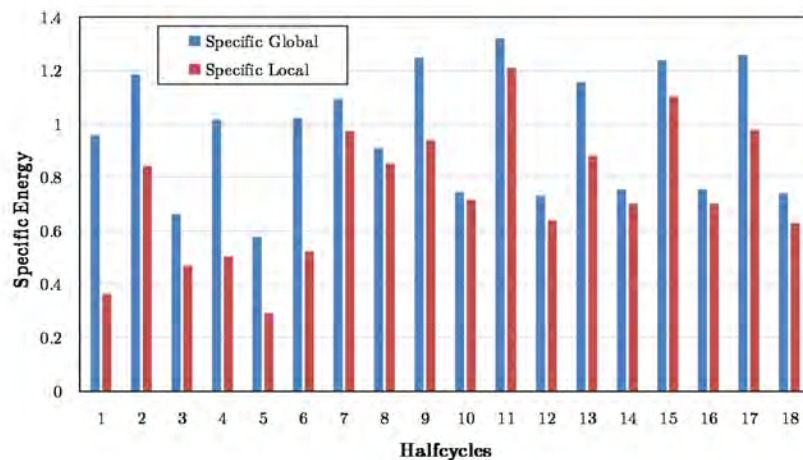
Figure 5.15: *Specific energy histogram providing a comparison between local and global energy dispersion. Energy values of Figures (5.13) and (5.13) are normalised relative to their respective elastic-plastic half cycles (Negro and Toniolo, 2012).*

5.1.3   PST 3

Test Procedure

In Section 4.8, the preliminary numerical analysis results indicated a substantial change in resistance and behaviour if two grouted rebar at each horizontal connection were removed. Thus, in contrast to PST 1, the structural design differed as two-thirds of the grouted rebar at the horizontal connections were used. The wall configuration was that of preliminary FE model 4H3V in Section (4.8).

Physical Scale Test 3 was conducted as a uniform pull-over test under the same load conditions as PST 1. The test itself was initially successful until a misalignment at the loaded end of the Instron stopped the pullover test suddenly. The displacement controlled test was however near completion and the test result was accepted. The test method therefore contrasts with PST 1 as it was limited explicitly to the pull-cycle.

Results

The force-displacement output of PST 3 in Figure (5.16) shows similar global shape, and the nonlinear displacement regions relate well to PST 1. The local displacement curve was unfortunately limited by LVDT failure, however the global displacement curve shape remains a sufficient comparison between the two tests.

It must be noted that the peak lateral force resistance of 132 kN is significantly lower than the PST 1 peak of 240 kN. The substantial difference is ascribed to the reduced number of connections.
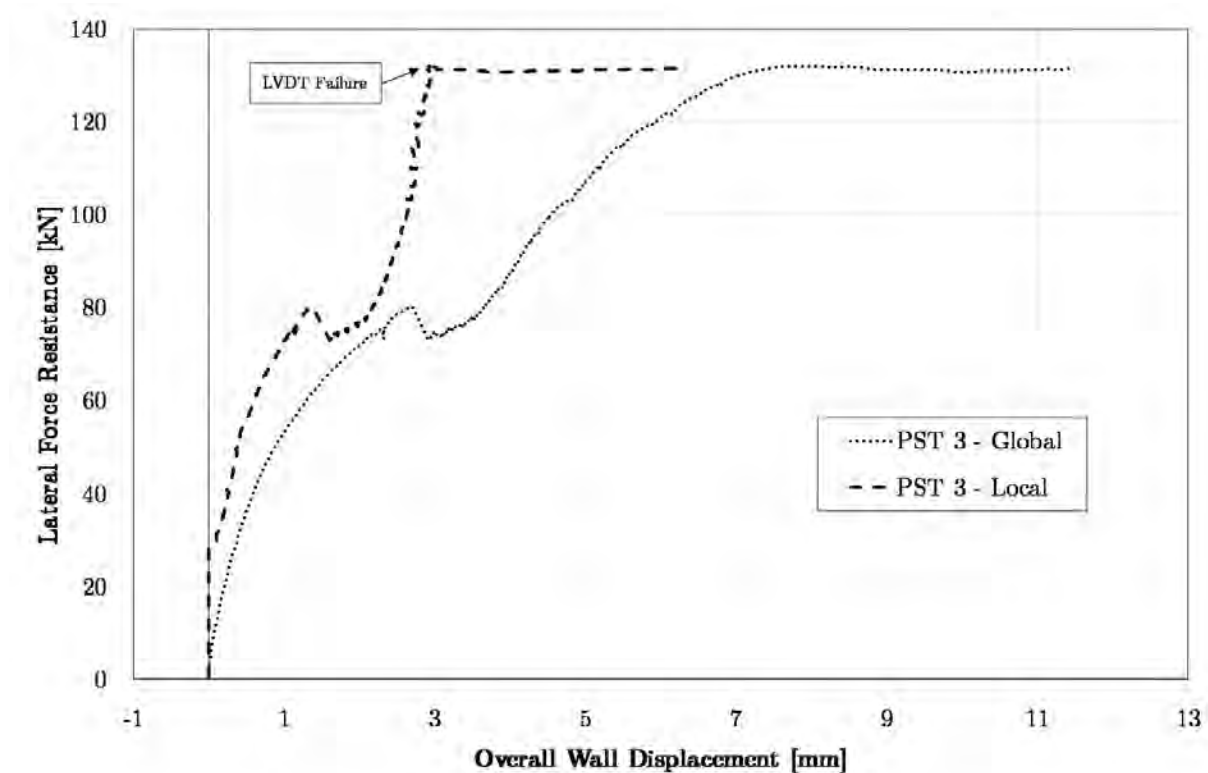
Figure 5.16: *PST 3: Force-displacement curve results for global and local displacement.*

The horizontal displacement between the two panels was measured by LVDT (vi) in Figure (3.21) for PST 3. The results shown in Figure (5.17) indicate that the LWFC panel further away from the Instron, the left-hand-side panel in Figure (5.1), remained stationary while the panel closest to the Instron moved with the Instron pull displacement. The data point (3.01875, 0.17125) highlighted in Figure (5.17) corresponds with the first nonlinear displacement region of PST 3 where lifting of the two LWFC panels halted the relative displacement between the two panels. These nonlinear displacement regions are explained in the following section.

Interpretation

For PST 3 there were three distinct regions of non-linear displacement. They are highlighted in Figure (5.18) as points 1), 2) and 3). These portions of the force resistance - displacement curve are detailed in following list.
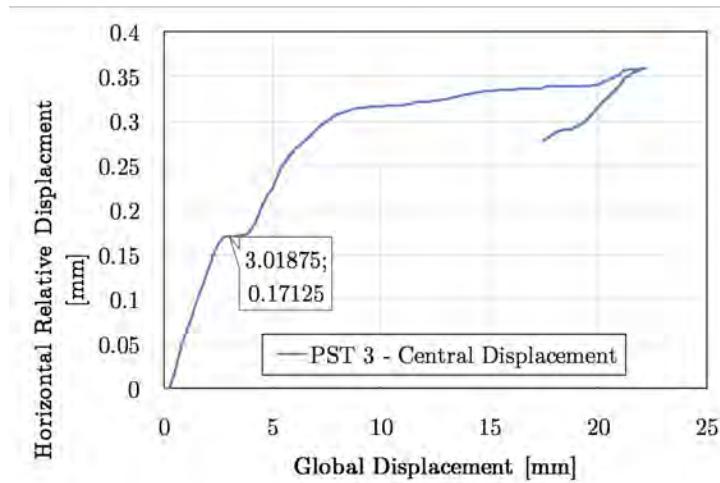
Figure 5.17: *PST 3: Horizontal displacement between the two LWFC panels, corresponding with nonlinear displacement region 1.*

1. Lifting at the far, left-hand side and rotation of the LWFC panels (Figure (5.19)).

2. Continued Lifting at the far side and rotation of both LWFC panels together (Figure (5.20)).

3. Visible slip at the horizontal connections, emphasised at the top horizontal connection (Figure (5.21)).
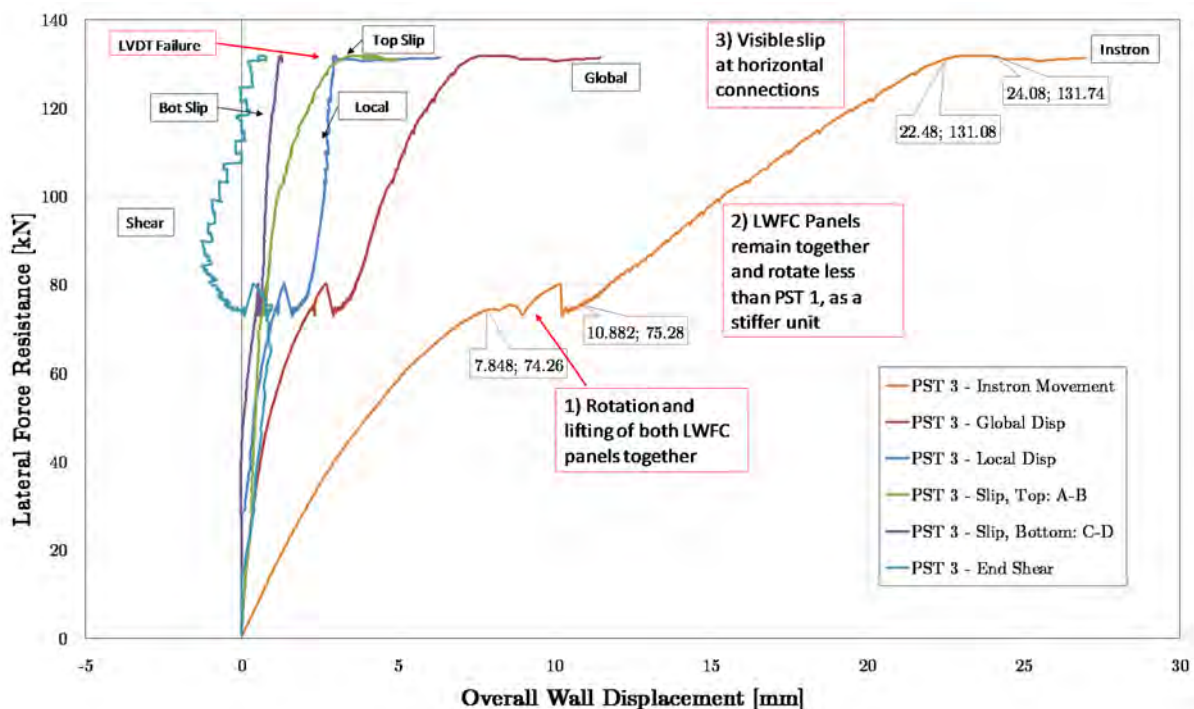
Figure 5.18: *Physical interpretation of the ascending pull-displacement of PST 3, Figure (5.16)*

As mentioned in Section (5.1.1) the LWFC panels of PST 3 displaced differently. The wall panels in PST 3 lifted at the far side and moved together as one single panel. This

Figure 5.19: *PST 3: First nonlinear displacement region, lifting on the LHS and global panel rotation.*

Figure 5.20: *PST 3: Second nonlinear displacement region, rotation of connected LWFC panels.*

difference in behaviour is attributed to the change in connection configuration. It is hypothesised that the horizontal connection of PST 3 was no longer equal in strength and number to the vertical box connections, leading to a dominant vertical connection. This dominant connection prevented slip at the vertical connection, unlike the slip that was noted in PST 1.

As a comparison between these two physical scale tests and their vertical displacement at the wall centre, Figures (5.22) and (5.23) graph the relative vertical displacement of each LWFC panel. The vertical displacement measured by LVDT's (vii) and (viii) of Figure (3.21) are termed "Vertical Disp: Instron Panel" and "Vertical Disp: Away Panel" respectively and relate to the vertical displacement of the panels close to and away from the Instron (Figure (5.1)).

Figures (5.22) and (5.23) show distinct differences in vertical displacements. As expected for PST 1, the vertical displacement at the panel further away from the Instron is limited

Figure 5.21: *PST 3: Third nonlinear displacement region, visible slip at the upper horizontal connection.*

after the initial 5 *mm* global displacement. Thereafter the displacement of the Instron panel is considerably higher; the difference between these displacements believed to be the slip at the vertical connection. For PST 3 there is only a subtle difference in these displacements as the two panels are lifted as one and displace vertically to a similar magnitude. This subtle difference for PST 3 is likely due to the distance between the two LVDTs.
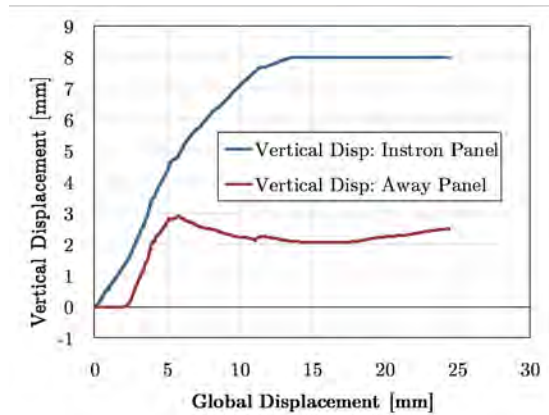
Figure 5.22: *Relative vertical displacement for PST 1, measured by LVDT's (vii) and (viii) of Figure (3.21).*
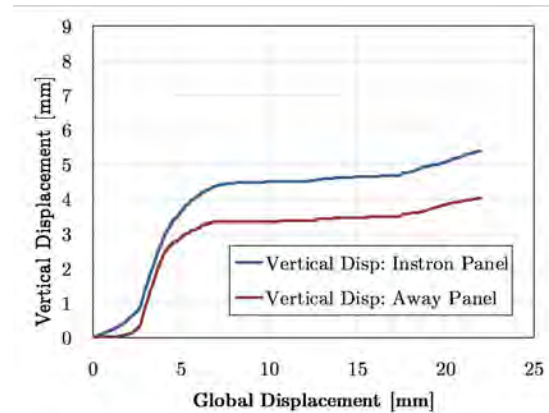
Figure 5.23: *Relative vertical displacement for PST 3, measured by LVDT's (vii) and (viii) of Figure (3.21).*

5.1.4 Spring Force Comparison

During the physical tests a moment developed across the structural steel member on which the springs were placed. Due to this moment the spring forces were seen to increase as the far side of the wall lifted, indicated by the linear-descending portion of the two curves in Figure (5.24). This increase in vertical force may have unrealistically improved the frictional interface behaviour in the physical tests. In Figure (5.24) a spring force

comparison for the physical tests is presented. The spring forces have been added and plotted against the global wall displacement. The initial load in the springs represents the pre-tension applied to simulate the vertical load from the two stories above the tested walls, determined in Section (3.2.3) and here calculated to be approximately 27 kN or 4.5 kN per spring.
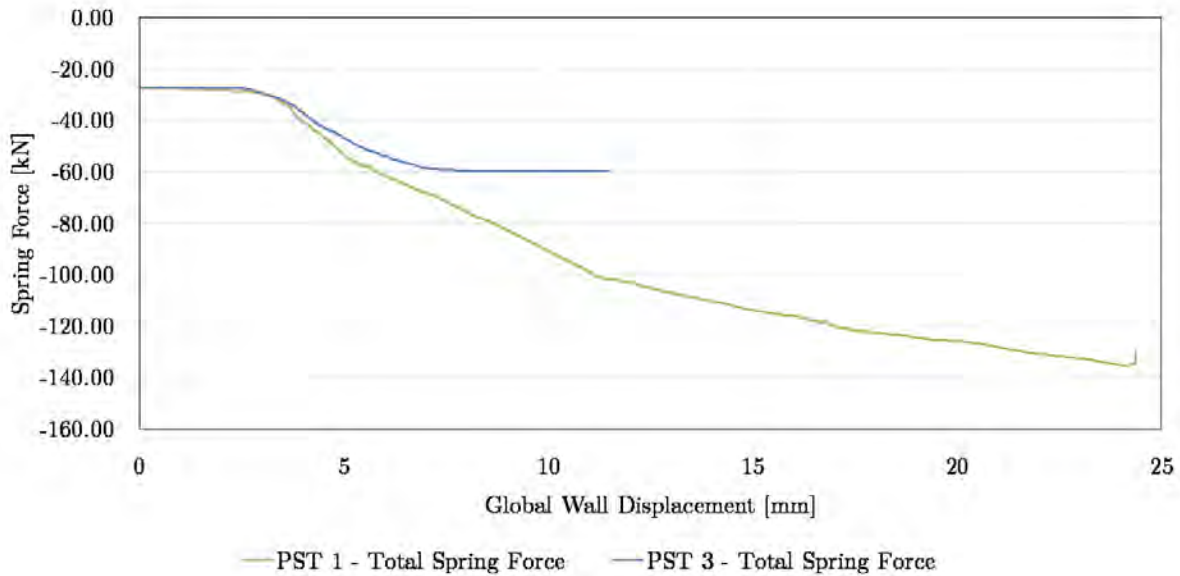
Figure 5.24: *Spring force comparison for physical tests PST 1 and PST 3*

5.2 Characterisation Tests

Characterisation tests were conducted to confirm specific LWFC material properties for further numerical analysis and to draw a comparison between reinforcement bond and connection box strength. Tensile tests on grouted rebar were also conducted.

Table (5.2) summarises the results of characteristic tests performed in accordance with Section (3.3) and details the updated material properties used for the final FE model. Characterisation tests performed by Grafe (2017) and De Villiers *et al.* (2017) are provided as a comparison to show changes and improvements in the material properties. The fracture energy (G_f) and characteristic length (l_c) were not determined in this study and the results of Grafe (2017) for fracture energy has been used. In addition to the controlled and perfectly cured specimens, cores were drilled out of the walls for a more accurate comparison of strength and density. Density and compressive strength were determined from the core samples (67 mm diameter and 145 mm height, Figure (5.26)); due to time constraints the Young's modulus was not determined but is expected to be higher due to continued hydration.

5.2.1 Concrete Material Properties

Table (5.2) references mix "16F" of De Villiers *et al.* (2017) as it is the only LWFC density comparable to this work, and the optimal Mix 8 of Grafe (2017) where a target dry density of 1400 kg/m^3 was sought. In this table there is a distinction made between the characteristic test values obtained as cured cubes and cored cylinders (Figure (5.26)). The

cored cylinders were formed from the same mix design but were of higher density due to the casting and compaction method discussed in §(3.2.2) and shown in Figure (5.25). In Figure (5.25) a poker vibrator was used to blend the required four mixes of LWFC. As a result of the aggregate-free LWFC mix design and possibly due to this compaction method, excess bleed water was observed and ultimately lost, leading to a increased overall dry density of 1579 kg/m^3. Note: The target casting density of 1600 kg/m^3 was obtained for the individual LWFC mixes before being mixed by the poker vibrator.
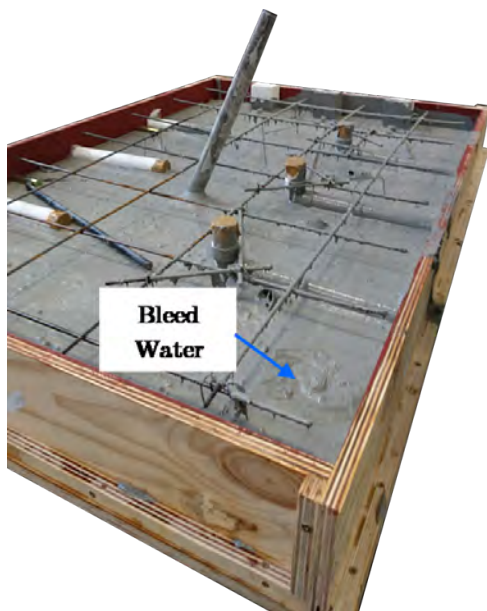
Figure 5.25: *Bleed water in LWFC panel: Likely cause for densified LWFC*

Figure 5.26: *Core drill setup for LWFC walls*

Table 5.2: *Updated material properties for PST tests*

Concrete	Grafe (2017): Mix 8	De Villiers *et al.* (2017): 16F	Cured LWFC	Cored LWFC
Dry Density $[kg/m^3]$	1400.00	1450.00	1382.30	1579.00
fcu $[MPa]$ **(Cube)**	12.36	32.26	19.84	NA
fcu $[MPa]$ **(Cylinder)**	NA	NA	23.79	22.02
Ec $[GPa]$	8.16	12.15	9.59	9.59[a]
ft $[MPa]$	1.41	2.90	1.41	1.41[a]
Gf $[N/m]$ **(Wedge)**	18.21	7.32	18.21	18.21[a]
Gf $[N/m]$ **(Beam)**	69.32	NA	69.32	69.32[a]
lc $[mm]$ **(Wedge)**	74.90	10.55	87.85	87.85[a]
lc $[mm]$ **(Beam)**	285.09	NA	334.38	334.38[a]

Values assumed to be the same as the cured LWFC, not tested.

The normalised material property curve (Figure (2.4) of De Villiers *et al.* (2017)) that was reiterated by Van Zijl *et al.* (2017) on the work of Grafe (2017), has been updated to include the cored-sample compressive strength and density from Table (5.2) and is presented as Figure (5.27). In Figure (5.27) both the wedge and beam determined fracture energy and characteristic length values are used and show a good comparison for the theoretical bond improvement of LWFC (Van Zijl *et al.* (2017)). The ultimate improvement is bench-marked against NWC values determined according to fib Model Code (2010).

A major improvement in l_c has been achieved, assuming that the G_f calculated by Grafe (2017) can be obtained for the cored wall material. In comparison to the work of De Villiers *et al.* (2017) where 3 % of the NWC l_c was obtained, the cored sample wedge and notched beam fracture energy characteristic lengths values have improved to 22 % and 85 % of their NWC counterparts - highlighted in Figure (5.27).
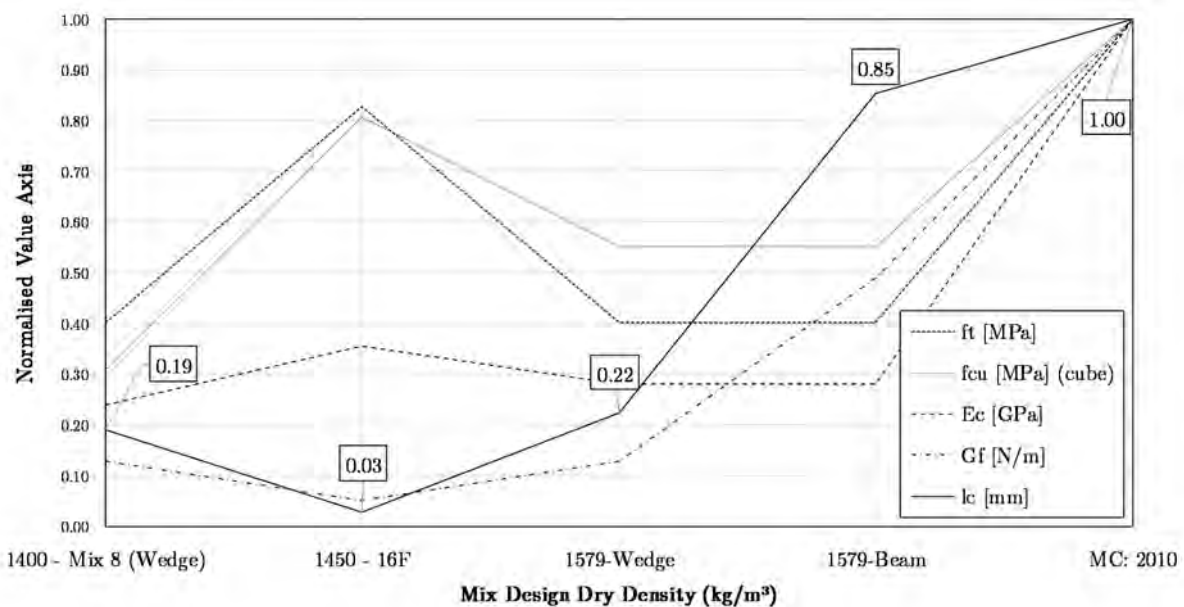
Figure 5.27: *Material property comparison normalised and focussed on characteristic length improvement as initially performed by De Villiers* et al. *(2017) and revised by Van Zijl* et al. *(2017). The figure shows the revised material properties and indicates greater improvement of characteristic length due to increased concrete strength, likely to lead to bond improvement of reinforcement in LWFC.*

5.2.2 Tensile Rebar Tests

Characteristic tensile tests were performed on the 12 *mm* rebar specimens used for connection anchorage in the physical tests. The reinforcement bars were tested according to SANS 6892-1:2010 (SANS, 2010) for tensile testing of reinforcement and tested on the 250 *kN* Zwick MTM (Figure (5.28)).

The results of the tensile tests are summarised in Table (5.3). The Young's modulus and yield stress were determined to be 215 *GPa* and 520 *MPa* and are within the SANS 920:2011 (SANS (2011*c*)) tolerance for high-tensile reinforcement steel in South Africa. Stress-strain curves until yield of the specimens are shown in Appendix (C.1).

Table 5.3: *Tensile test results of Y12 reinforcement rebar, tested according to SANS 6892-1:2010 SANS (2010)*

Specimen	Young's Modulus [GPa]	Yield Stress [MPa]
1	214	510
2	215	542
3	220	516
4	213	514
5	211	507
6	217	532
Avg.	215	520
Std. Dev.	3	13
C.o.V.	1%	2%

5.2.3 Connection Box Tests

Uni-axial tensile tests were conducted on the connection boxes to obtain their capacity and determine if design improvements should be made for future physical tests. The tests were conducted according to the same SANS 6892-1:2010 code for tensile testing of reinforcement (Section (5.2.2)) and also tested in the 250 kN Zwick MTM. Boxes 1-4 were of the same dimensions, dictated by the chosen design in Appendix (A.3). Box length for box 5 was reduced from 70 mm to 50 mm and was a prototype connection box, not used for physical tests. A size comparison between the two connection boxes can be seen in Appendix (A.1).

Consistent results for the force-displacement curves are shown in Figure (5.31). Non-linear, plastic displacement began at approximately 15 kN tensile force where the slotted 5 mm plate began to yield (Figure (5.30)). The decreased length of the single "Box-5" specimen lead to a significant (20 %) decrease in ultimate force-displacement at test end. This difference was likely caused by a decrease in the connection length and flexibility, focussing the force and deformation earlier in the test in comparison to the longer connection boxes.

A summary of reinforcement design bond stresses (σ_d) are presented in Table (5.4). σ_d results of De Villiers *et al.* (2017) are presented for mixes $12F$, $14F$ and $16F$; alongside LWFC material properties of Grafe (2017). Following the work of Grafe (2017), improved reinforcement bond was hypothesised by Van Zijl *et al.* (2017) to be proportional to an improvement of fracture energy and characteristic length (Section (2.1.6)). It was therefore necessary to firstly confirm what the improved design bond stress of the LWFC could be and how the reinforcement bond compared to the tensile strength of the connection boxes.

Table (5.4) presents a summary of the changes in both these material properties from the work of De Villiers *et al.* (2017), making use of the results from Grafe (2017). The characteristic length results were of this study and made use of an assumed fracture energy. Theoretical bond improvements are presented in Table (5.4) and σ_d was increased in proportion to both the improved characteristic length as well as the fracture energy. The basis for this improvement was De Villiers *et al.* (2017) mix $16F$, the closest dry density to
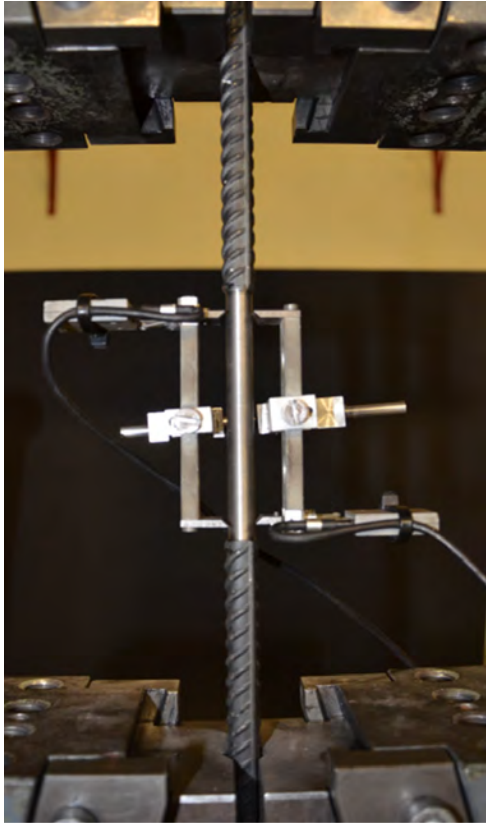
Figure 5.28: *Characteristic test on Y12 rebar in* 250 *kN Zwick MTM*

Figure 5.29: *Vertical connection box test setup in* 250 *kN Zwick MTM under tensile load*

Figure 5.30: *Tested connection box showing yielded side at out-of-plane horizontal slot.*

that of the cored samples. This improvement was distinguished between the two fracture energy test methods, namely: notched-beam and wedge-splitting. The altered bond stress was later compared to the theoretical bond of 40 MPa NWC, determined via fib Model Code (2010).

Ultimately the improvement in bond due to the difference in l_c was too great (from $\sigma_d = 0.72$ to 7.9-35.67 MPa) and theoretically higher than the reinforcement bond of NWC (3.5 MPa). These unrealistic results have not been tabulated. It was therefore decided that the smaller improvement - directly due to increased G_f - would be used. In Table (5.4) an improvement from 0.72 MPa to 1.79 MPa was conservatively chosen and is based on the lower, wedge-splitting G_f value. For completeness the notched-beam fracture energy improvement of 6.82 MPa is presented.

Utilising Equation (5.2) and an assumed embedded depth of 5 diameters, the maximum depth for σ_d by De Villiers (2015), the maximum tensile force resisted by Y12 rebar under the chosen $\sigma_d = 1.79$ is 5.4 kN. The 15 kN tensile strength of the connection box is approximately triple the potential tensile force in the anchored rebar. The connection boxes are therefore of adequate strength as the rebar is likely to lose bond strength before the connection boxes yield. No changes to the current connection box are proposed, although shear tests on in-situ connection boxes may provide more information in cases of significant inter-wall slip along the vertical joint, these tests were however not performed.

$$T_f = (2 \cdot \pi \cdot r) \cdot (5 \cdot d) \cdot \sigma_d \tag{5.2}$$

Where:

r is the reinforcement bar radius
d is the reinforcement bar diameter, and
T_f is the tensile force resistance
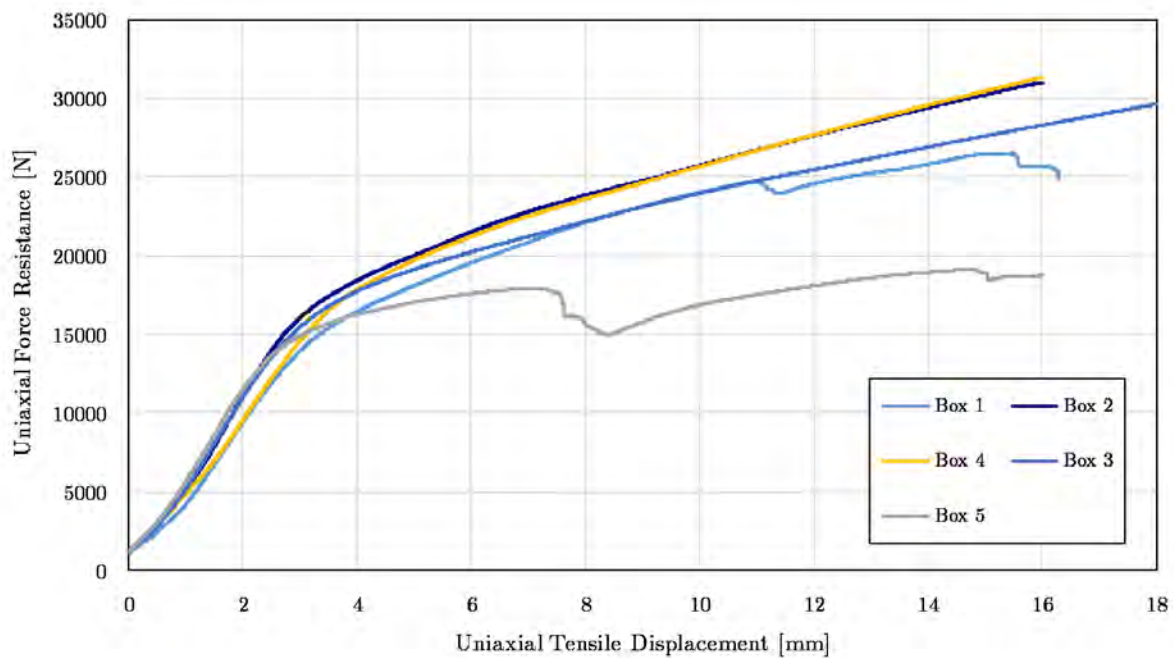
Figure 5.31: *Tensile test results of connection boxes*

Table 5.4: *Concrete design bond stress (σ_d) improvement according to the work of De Villiers et al. (2017), Grafe (2017) and Van Zijl et al. (2017).*

	Comp Strength, fcu [MPa]	Tensile Strength, ft [MPa]	Young's Modulus, E [GPa]	Fracture Energy, Gf [N/m]	Char Length, lc [mm]	Design Bond Stress, sigma d [MPa]
De Villiers, 12F	10.41	1.05	6.46	4.67	27.47	1.06
De Villiers, 14F	19.10	1.71	8.75	5.72	17.08	1.05
De Villiers, 16F	32.26	2.90	12.15	7.32	10.55	0.72
Grafe, Mix 8: Wedge	12.36	1.41	8.16	18.21	74.90	1.79
Grafe, Mix 8: Beam	12.36	1.41	8.16	69.32	285.09	6.82
Dunn: Wedge	23.0	1.41	9.59	18.21	87.85	1.79
Dunn: Beam	23.0	1.41	9.59	69.32	334.38	6.82
NWC: MC 2010	40.00	3.51	34.13	141.81	393.10	3.50

5.3   Numerical Analyses

Numerical analyses were performed, based on the final LWFC material properties and updated FE model configuration. This section details the results of those analyses and attempts to draw a comparison between the physical tests and numerical models for reinforced LWFC. The FE models did not include the second, cyclic test but focussed on the monotonic pull-over, physical tests: PST 1 and PST 3. The cyclic tests were neglected due to scope limitations. Numerical modelling of the cyclic test is advised for future research. The section is concluded with an explanation of the limitations of the developed model.

5.3.1   Updated LWFC Material Model

Characteristic strength, density and Young's modulus tests were conducted on the LWFC specimens as per Section (3.3). These results are listed in Table (5.2) and are the LWFC material properties in the final FE models.

The final LWFC material model made use of the exact density and compressive strength of 67 mm diameter and 145 mm height cored wall samples. The Young's modulus chosen was derived from cured cylinders of 100 mm diameter and 200 mm height while the fracture energy was chosen to be 69.32 N/m, calculated by Grafe (2017) through notched-beam bending tests. The Poisson's ratio was assumed to be $v = 0.2$.

5.3.2   Final FE model

The final FE model better replicated the physical test setup and utilised updated LWFC material properties for the tested walls. The un-meshed FE model configurations of PST 1 and 3 are shown in Figures (5.32) and (5.33).

The turquoise beam and attached yellow steel end-plate represent the $254 \times 254 \times 89$ structural steel section through which the lateral load was applied to the wall. In addition to the structural steel member, the coil springs were placed further away from the wall, on top of the steel member and provided better moment-arm distances. The self-weight loads from the prototype house above (Figure (3.3)) and the tested wall were also applied more accurately and are the best representation of the physical test in the final FE model.
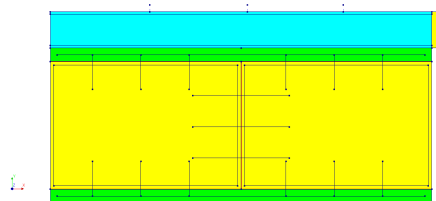
Figure 5.32: *PST 1: Three vertical connection boxes and six grouted rebar at horizontal connections per LWFC panel (FE Model 25-06)*
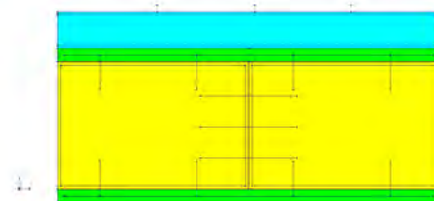
Figure 5.33: *PST 3: Three vertical connection boxes and four grouted rebar at horizontal connections per LWFC panel (FE Model 05-01)*

5.3.3   PST 1, 25-06

Introduction

The preliminary FE model 6H3V (4.8) was updated for the final FE model of PST 1. Each analysis attempt was uniquely named and the selected analysis was FE model 25-06. The remaining analyses used are detailed in the sensitivity study (Section (5.4)).

Results

The force-displacement results of 25-06 alone are shown in Figure (5.34). The local, global, top slip and bottom slip are measured similarly to the physical tests; the end-shear is the effective local displacement at the unloaded or far-side of the LWFC wall panels (Figure (5.1)). The comparison between the results of PST 1 and the FE model are shown in Figure (5.35).

In this test two local failure points are observed, as indicated in Figure (5.34). Peak 1 is the point at which the lower horizontal connection cracks and the wall begins to lift up and rotate due to the lateral displacement. Peak 2 correlated well with the final observed failure of the wall - the point at which slip was noted across the top horizontal connection.

In comparison to the nonlinear regions of PST 1, distinct changes in the force-displacement curves are noted. The changes to both the global and local deformation are subtle changes in gradient and not peak drops. Both changes in gradient do however correlate well with the two failure mechanisms observed in the physical test. The two gradient change points are circled on the global deformation curve in Figure (5.35) and are nonlinear displacement regions 1 and 4 of PST 1 in Figure (5.3).
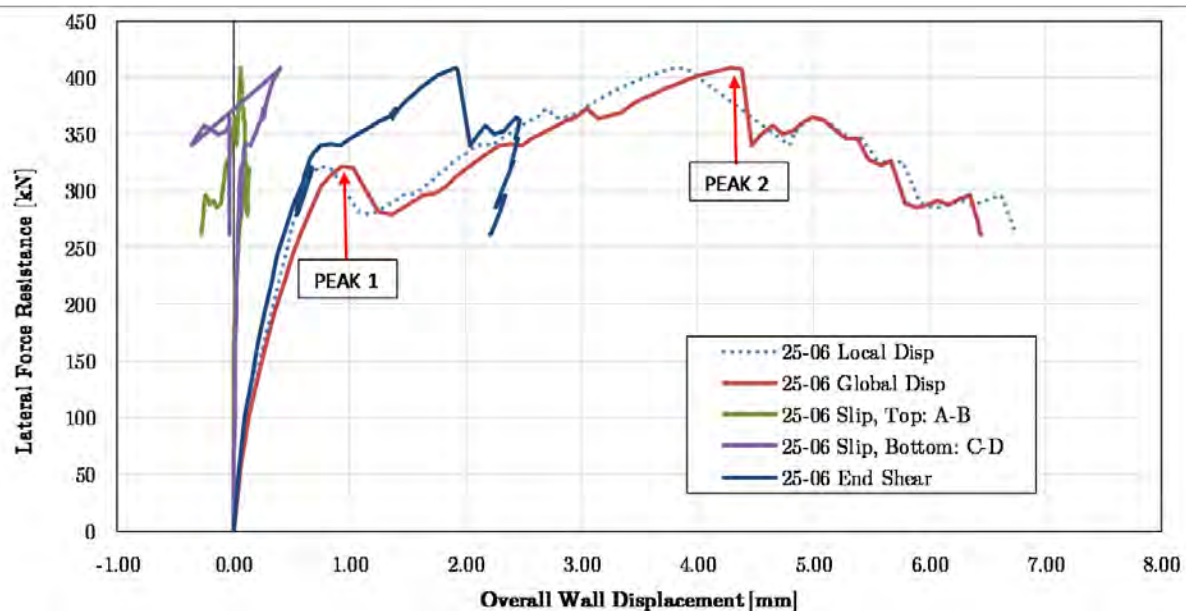
Figure 5.34: *Final FE model results of 25-06 showing global displacement peaks 1 and 2.*

Interpretation

The global and local displacement curves of the FE model in Figure (5.34) follow closely on one another and show that the full panel is activated and displaces together with the
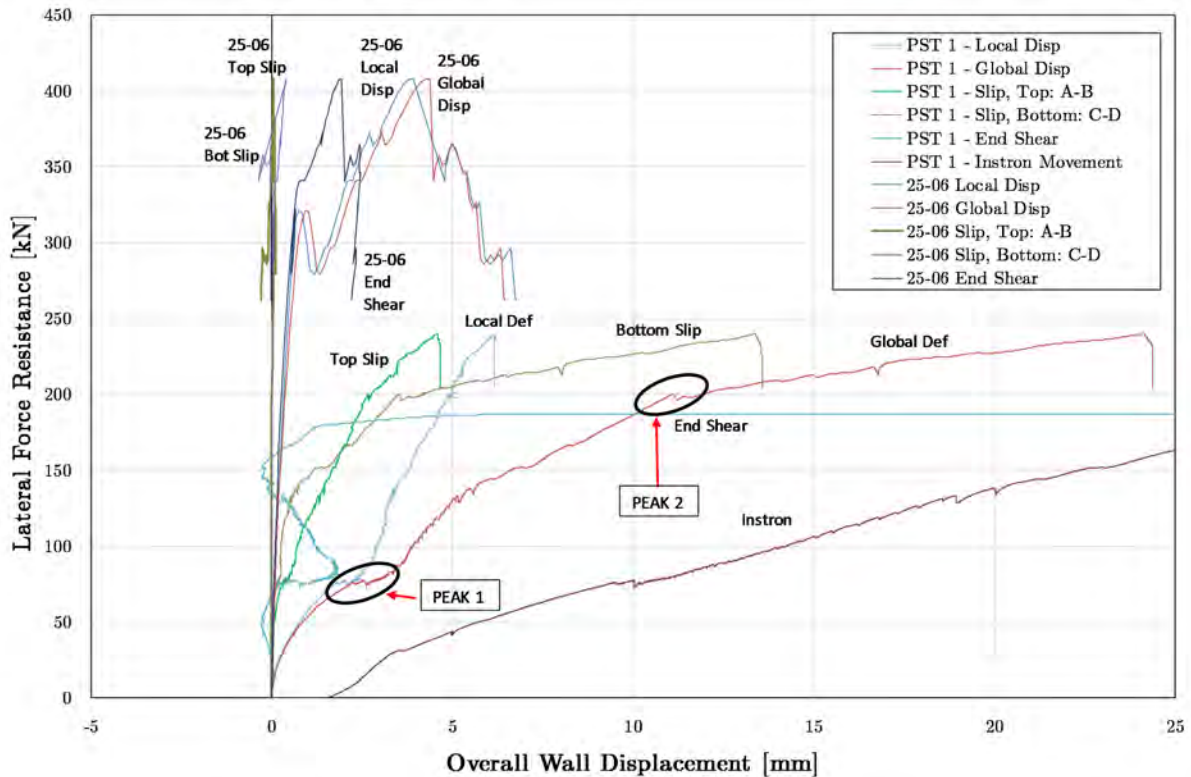
Figure 5.35: *Comparison between the results of PST 1 and FE model analysis 25-06. Peaks 1 and 2, herein highlighted for the global displacement of the physical tests, correlate with the FE model peaks in Figure (5.34).*

wall without considerable slip. The end-shear notably drops at the second peak, indicating slip at the horizontal connections and a return of the wall to it's un-rotated configuration. This slip is observed in the displaced form of the wall and crack layout for the second peak in Figure (5.37).

For 25-06 it is important to note in Figure (5.37) that top slip only occurs after peak 2 and that the global panel displacement is lead by local displacement for this stronger panel.

Dowel action is visible in Figure (5.36) which shows the cracked state at the first peak where the cracks are focussed along the grouted vertical rebar along the horizontal connections. This dowel action is in contrast to the less cracked state of the FE model for PST 3 (05-01) in Figure (5.41) and corresponds well with the differing final cracked states for the physical tests in Figures (5.38) and (5.43) of physical tests 1 and 3. This confirmation is an indication of better load transfer across the horizontal connection for PST 1, 25-06 in contrast to PST 3, 05-01 where the LWFC panels are barely damaged.

Figure 5.36: *Final FE model results of 25-06, cracking at first peak.*

Figure 5.37: *Final FE model results of 25-06, cracking at second peak.*
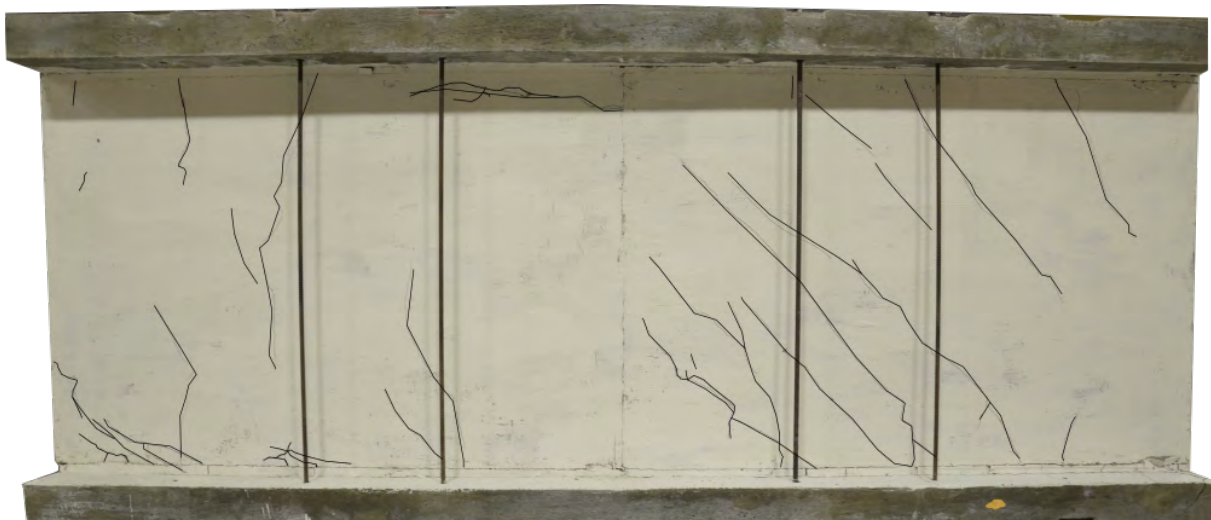
Figure 5.38: *Final cracked state for physical test, PST 1*

5.3.4   PST 3, 05-01

Introduction

The preliminary FE model 4H3V (4.8) was updated for the final FE model of PST 3. Each analysis attempt was uniquely named and the selected analysis was FE model 05-01. The remaining analyses used are detailed in the sensitivity study (Section (5.4)).

Results

The force-displacement results of 05-01 alone are shown in Figure (5.39). Similarly to the FE results of PST 1, there are two distinct peaks that correlate with the initial lifting and rotation of the wall and are followed by the final slip at the top horizontal connection.

The comparison between the results of PST 3 and the FE model are shown in Figure (5.40). The two nonlinear displacement peaks of the FE test results are related to the nonlinear displacement regions 1 and 3 in Section (5.1.3), circled and labelled as peak 1 and 2 in Figure ((5.40)).
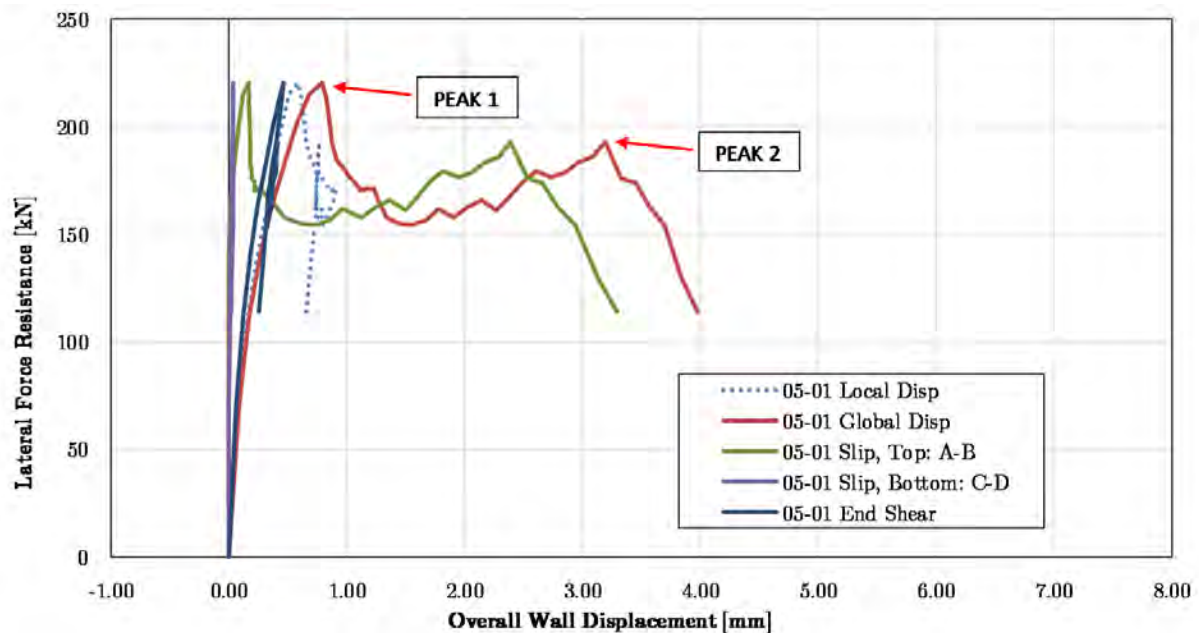
Figure 5.39: *Final FE model results of 05-01 showing global displacement peaks 1 and 2.*

Interpretation

Based on the crack profile of Figures (5.41) and (5.42) and confirmed by the physical crack profile of Figure (5.43), the dowel action capacity for PST 3, 05-01 is sooner reached and exceeded, resulting in slip across the grouted connection. This obvious comparison is likely due to the reduction in number of dowels between the two models.

The displacement shape of the FE model results for 05-01 differs distinctly to that of 25-06. The differences are most distinct with regard to end-shear, local displacement and top slip. For 05-01 the global, overall wall displacement is closely linked to the top slip displacement in Figure (5.39) which reinforces the understanding of the weaker horizontal connection and evident top slip in the physical test (Figure (5.21)). In comparison to 25-06, top-slip at the horizontal connection now governs the displacement response of the wall.
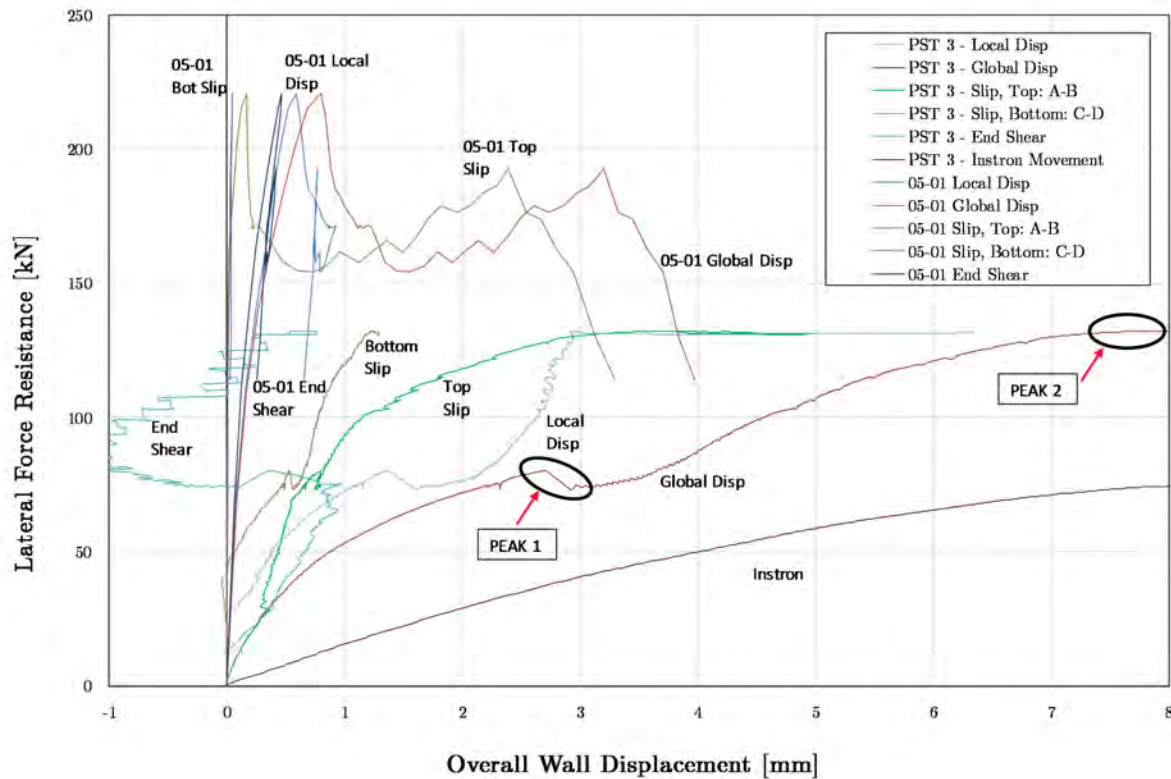
Figure 5.40: *Comparison between the results of PST 3 and FE model 05-01*

The sharp drop in end-shear and local displacement in Figure (5.39) may indicate the onset of dowel action in 05-01. These dowels are overcome by slip and possible shear, indicated by the capacity drop at the second peak.

Another indication of the differing dowel action between the two models is the higher peak lateral force resistance of FE model 25-06 (408 kN), considerably higher than that of 05-01 (220.5 kN) and also occur at peak 2 rather than peak 1. The different peak values are in proportion to the 240 kN and 132 kN peaks of the respective PST 1 and PST 3 physical tests. Overall the resistance of PST 1, 25-06 is close to double that of PST 3, 05-01 for the physically tested and FE walls, indicating a stronger and possibly better connected wall for PST 1, 25-06.

Peak lateral resistance occurred at peak 2 for 25-06, which gives an indication of the energy dissipating, absorption ability of 25-06 which displaces further before failure. This is in contrast to 05-01 which has an earlier drop in capacity and maximum lateral force at peak 1. The peak-to-peak distance of 25-06 is 3.34 mm and is considerably larger than the 2.4 mm of FE model 05-01. This increase in distance of 40 % between the peaks of 25-06 relates well to the physical tests where a comparative distance of approximately 8.6 mm peak-to-peak for PST 1 and 5.1 mm for PST 3, or 68 % was observed. The physical implications of this increase is that the better connected PST 1 (25-06), with a larger overall deflection, has a higher energy absorption capacity than PST 3 (05-01).
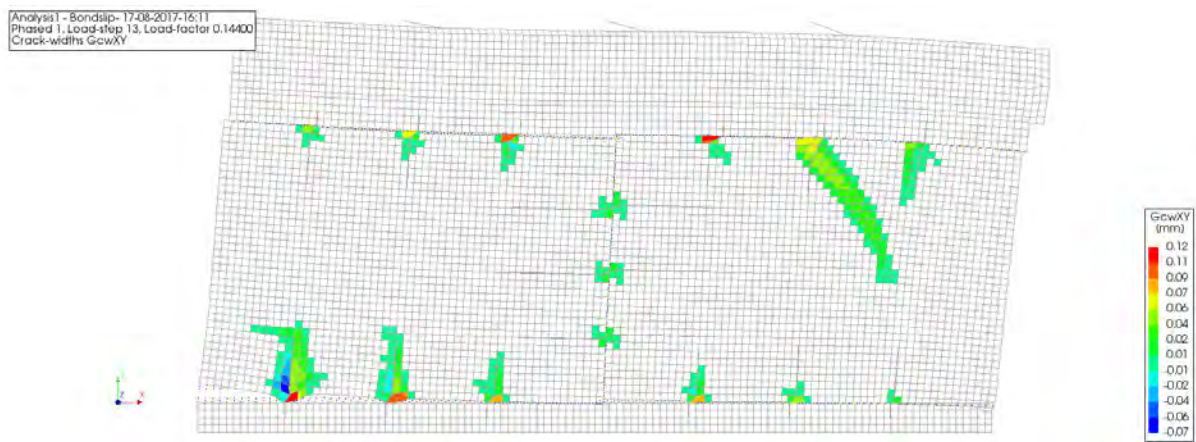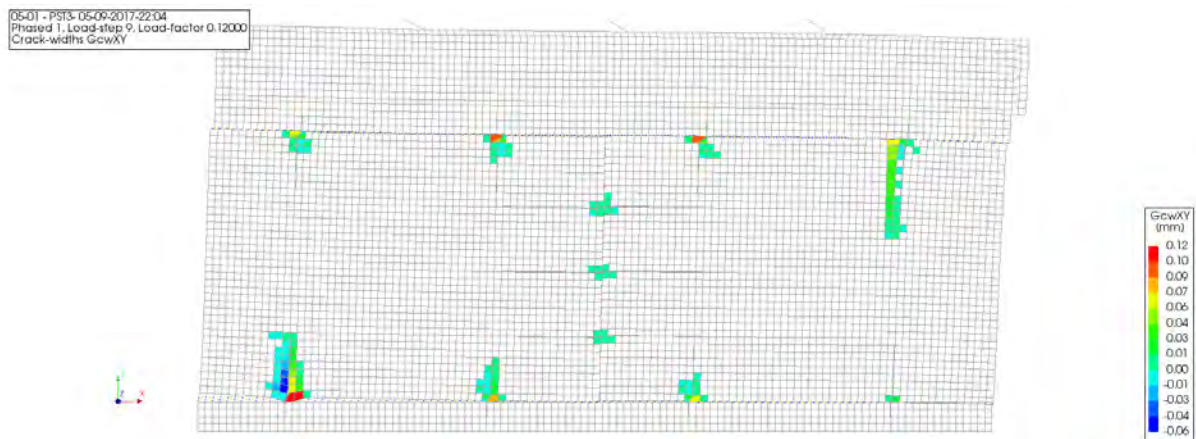
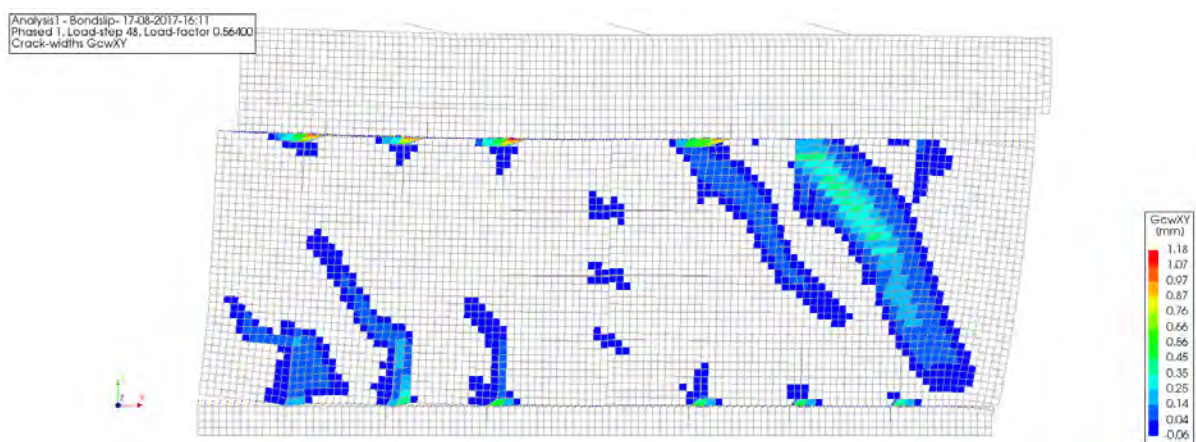Figure 5.41: *Final FE model results of 05-01, cracking at first peak.*
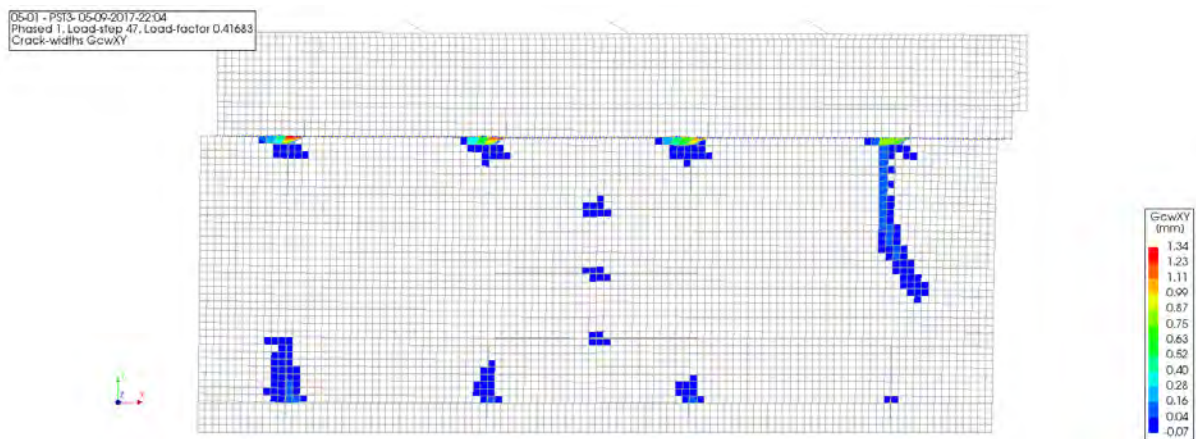
Figure 5.42: *Final FE model results of 05-01, cracking at second peak.*

Figure 5.43: *Final cracked state for physical test, PST 3*

5.3.5 Vertical Displacement at Vertical Connection

In this subsection a comparison of the vertical displacement at the vertical connections is given. In the physical test results of PST 1, there was a change from overall panel movement to individual LWFC panel movement, indicated by the different vertical displacement of each panel at the vertical connection between the two LWFC panels. This was in contrast to the lift and continued rotation of both panels together for PST 3 (Section (5.1)).

For the FE models, the overall initial magnitude of the vertical displacement at the Instron panel is again higher for PST 1, 25-06 and does correlate with the physical tests. In Figure (5.44) the vertical displacement at the Instron panel is 0.118 *mm* for 25-06 in contrast to 0.06 *mm* for 05-01 (in Figure (5.45)) at 1.0 *mm* global displacement.

The vertical displacements for 25-06 (Figure (5.44)) shows a lag between the Instron and away panel displacements where the away-panel displacement is initially negative and later follows the shape of the Instron panel displacement. This initial negative displacement and lag is also noted for 05-01 in Figure (5.45). This trend in both models is thought to be due to the simplified vertical connections where the rigid steel box in voided LWFC has been replaced by a bond-slip rebar for the FE models (Section (4.9.1)).

Another difference between the two FE models is the global displacement point at which the Instron and away panel vertical displacement curves begin to follow the same shape. For 25-06 this point is after approximately 1.5 *mm* in contrast to the earlier change at about 0.5 *mm* global displacement for 05-01. This difference is a possible indicator of the point at which the two wall panels begin to displace together. This contrasts with the physical test data which suggested that local displacement of individual panels follows after the displacement of both panels together and suggests that this is switched around; where individual displacement is initially present and is followed by displacement of both panels together.

Ultimately, the distinction between the vertical displacements of PST 1 and PST 3 are less noticeable for the FE models. The different magnitudes of vertical displacements do however allude to greater local displacement for 25-06 in contrast to 05-01 as observed for the physical tests in Section (5.1.3).
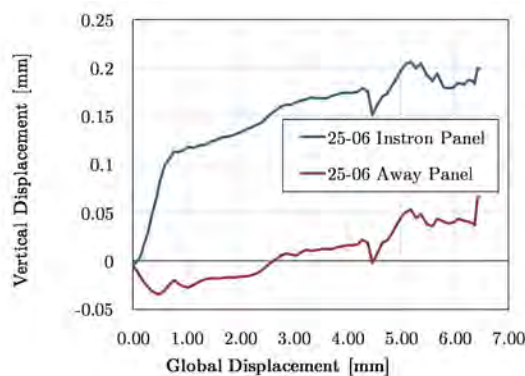
Figure 5.44: *Relative vertical displacement for FE model of PST 1, measured in the FE model at LVDT points (vii) and (viii) of Figure (3.21).*
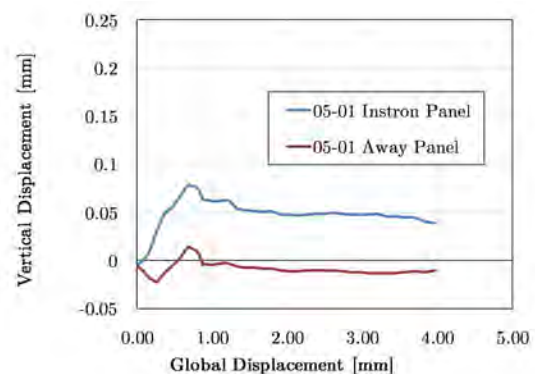
Figure 5.45: *Relative vertical displacement for FE model of PST 3, measured in the FE model at LVDT points (vii) and (viii) of Figure (3.21).*

5.3.6   Spring Force Comparison

The final FE model included springs that best simulated this increase in applied vertical force. Un-tensioned springs to ground were placed in the model that would increase the applied vertical load with rotation of the wall. The spring stiffness was derived from the gradient of the descending branch of the vertical displacement - spring force curve for PST 1 and PST 3, calculated to be approximately 82 kN/mm (Figure (5.46)).
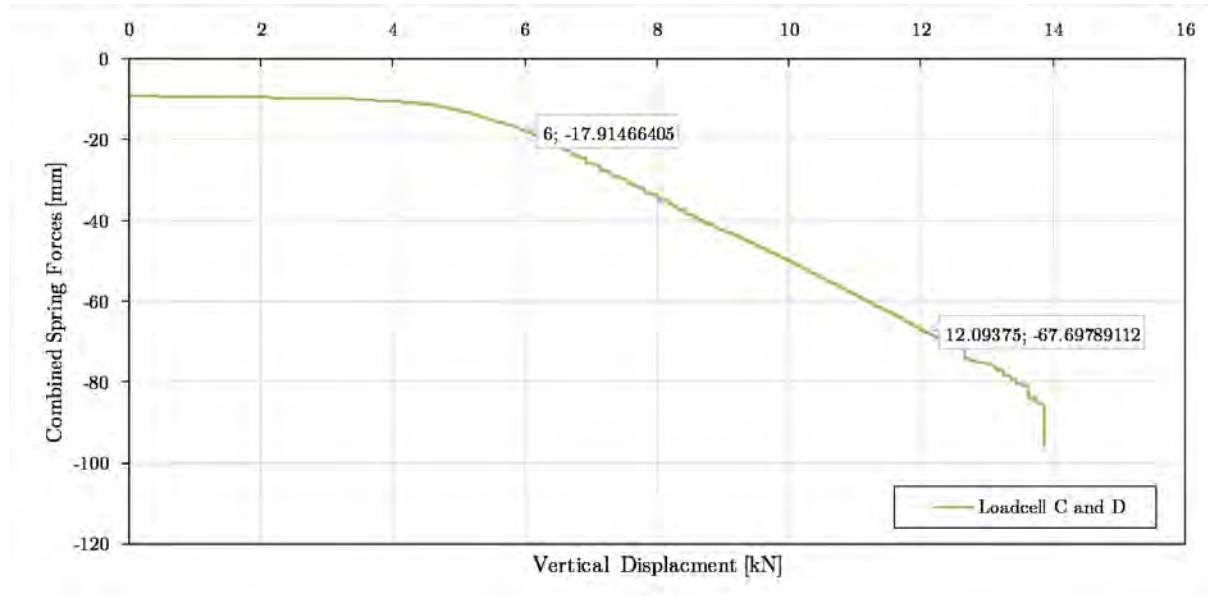
Figure 5.46: *Spring-displacement gradient used for FE model spring stiffness determination. Load-cells C and D were the load cells furthest away from the Instron head and were shown to have the highest increase in spring-force due to vertical displacement.*

In Figure (5.47) this spring force was combined with the distributed vertical force that represented the sustained vertical load from the structure above. The initial load of 36.2 kN was 34 % higher than the physical tests and increased suddenly with a sharper descending branch for both the PST 1 and PST 3 FE models (25-06 and 05-01). The plateau of FE model 05-01 and PST 3 were of similar 60 kN magnitude. For 25-06 and PST 1 the curve shape was similar but the overall force magnitude was significantly different; peaking at 200 kN for the FE model and 135 kN for PST 1.

Possible reasons for the different shape and magnitude of the simulated curves is the immediately applied lateral loads for the FE models. In Sections (5.3.3) and (5.3.4) the first peaks of the FE models were reached sooner and had sharper ascending force-displacement branches than their physical test counterparts. This is likely due to the simplified interfaces at the horizontal connections in the FE models where friction and stiffness's were prescribed at the zero-tension interface. Here the interface properties were based on theoretical data and were not empirically derived. These assumptions may have overestimated the friction and resulted in increased vertical displacement and therefore higher spring forces.
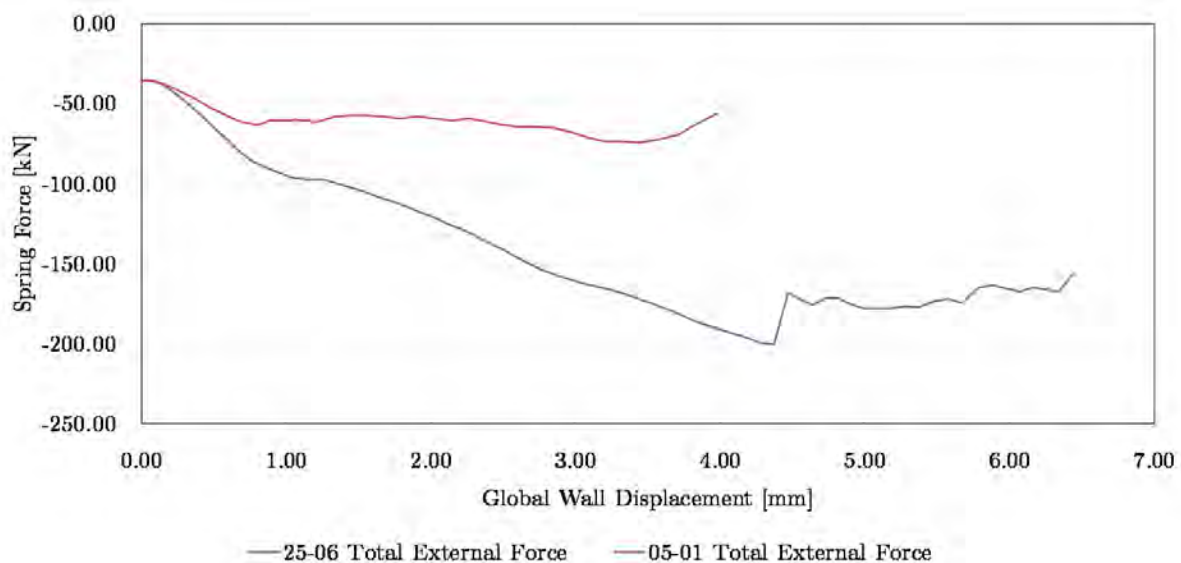
Figure 5.47: *Combined spring and applied load, external force comparison for FE models of PST 1 (25-06) and PST 3 (05-01).*

5.3.7 Model Limitations

Limitations of the final FE model are described in this section and form the basis for recommended improvements in Section (7.3).

Slip in Frame not accounted for: Slip was observed during the physical tests at the underside of the wall test setup frame, where the frame was anchored at two points to the laboratory strong floor. This loss of friction in the physical test frame was not accounted for in the FE model as a fixed translation boundary condition was prescribed at the bottom of the wall.

Theoretical interface stiffness: The prescribed interface stiffness was theoretically determined as described in Section (4.3) and not physically measured. An accurate understanding of this interface may lead to better similarity between the stiffness of the physical tests and FE models.

Theoretical inter-facial friction: The physical interface included a masonry mortar joint. The prescribed interface friction was hence assumed to be high (45 deg), however it was not experimentally tested. An accurate understanding of this inter-facial friction may lead to better similarity between the stiffness of the physical tests and FE models.

5.4 Finite Element Sensitivity Study

A sensitivity study is conducted on the updated FE models for PST 1 and PST 3. Spring stiffness, steel connection area and the interface friction angle are varied for the structural design sensitivity analysis. Thereafter a sensitivity study is performed on the LWFC material where fracture energy, tensile strength and compressive strength are changed for separate FE models. The dependence of the FE model on each of these criteria is

determined for PST 1. The results of the sensitivity study are subsequently used to calibrate PST 3 where only the spring stiffness sensitivity is tested.

The sensitivity study comprises of 21 FE models where the basis for comparison is the chosen final FE models 25-06 and 05-01. The models are compared according to the total spring force, vertical displacement at the side furthest from the Instron displacement, the total lateral force and finally the local and global displacements at the highest point on the global displacement graph. A summary of these peak values is presented in Table (5.5).

The sensitivity to each of the structural design elements and material properties are presented in Sections (5.4.1), (5.4.2) and (5.4.3) where the global displacement-lateral force curves are plotted for each variable under consideration.

Table 5.5: *Sensitivity study peak values for each FE model*

	25-03	25-04	25-05	25-06	25-07	25-08	25-09
Spring Force [kN/mm]	33.40	46.80	124.00	164.00	56.00	54.50	170.13
Vertical Displacement [mm]	0.50	0.49	1.24	1.20	0.51	0.50	0.95
Lateral Force [kN]	305.40	300.38	395.18	408.15	314.16	307.85	316.75
Local Displacement [mm]	0.75	0.74	4.00	3.82	0.74	0.75	2.54
Global Displacement [mm]	0.95	0.95	4.49	4.28	0.94	0.95	3.05
	26-01	26-02	26-03	26-04	26-05	26-06	26-07
Spring Force [kN/mm]	267.88	71.85	48.00	117.60	169.00	327.66	100.18
Vertical Displacement [mm]	1.23	0.58	0.50	0.84	1.19	1.64	0.94
Lateral Force [kN]	458.20	307.20	309.12	309.26	405.73	485.28	348.72
Local Displacement [mm]	4.03	0.80	0.75	0.99	3.65	4.07	3.21
Global Displacement [mm]	4.39	1.03	0.94	1.22	4.09	4.55	3.55
	26-09	27-08	27-09	27-10	27-11	28-01	05-01
Spring Force [kN/mm]	39.13	22.04	39.13	24.23	43.78	41.97	27.47
Vertical Displacement [mm]	0.40	0.24	0.40	0.25	0.40	0.40	0.41
Lateral Force [kN]	258.13	214.68	258.13	217.58	261.68	230.87	220.52
Local Displacement [mm]	0.54	0.41	0.54	0.41	0.54	0.57	0.59
Global Displacement [mm]	0.66	0.53	0.66	0.53	0.69	0.77	0.80

5.4.1 PST 1: Structural Design

Changes in structural design are considered to be changes that could affect the overall FE model behaviour. The spring stiffness and interface friction angle are altered as per Table (5.6) and the grouted dowel area is halved in Table (5.7).

Spring Stiffness and Interface Friction Angle

Figure (5.48) details the sensitivity of global displacement with regard to both spring stiffness and interface friction angle. The stiffness of the restraining springs on top of the PST 1 FE models were either all 200 kN/mm or placed in pairs of 50, 100 and

200 kN/mm, the stiffest springs furthest away from the Instron head. The interface friction angle which determined the coefficient of static friction, μ of both the vertical and horizontal connections, is decreased as per Table (5.6) for both of these spring stiffness configurations.

Table 5.6: *Sensitivity to both spring stiffness and interface friction angle*

Spring Stiffness [kN/mm]	200				50, 100 and 200			
Friction Angle [deg]	30	35	40	45	30	35	40	45
FE Model	26-02	25-08	25-07	25-06	25-04	25-03	26-03	25-05
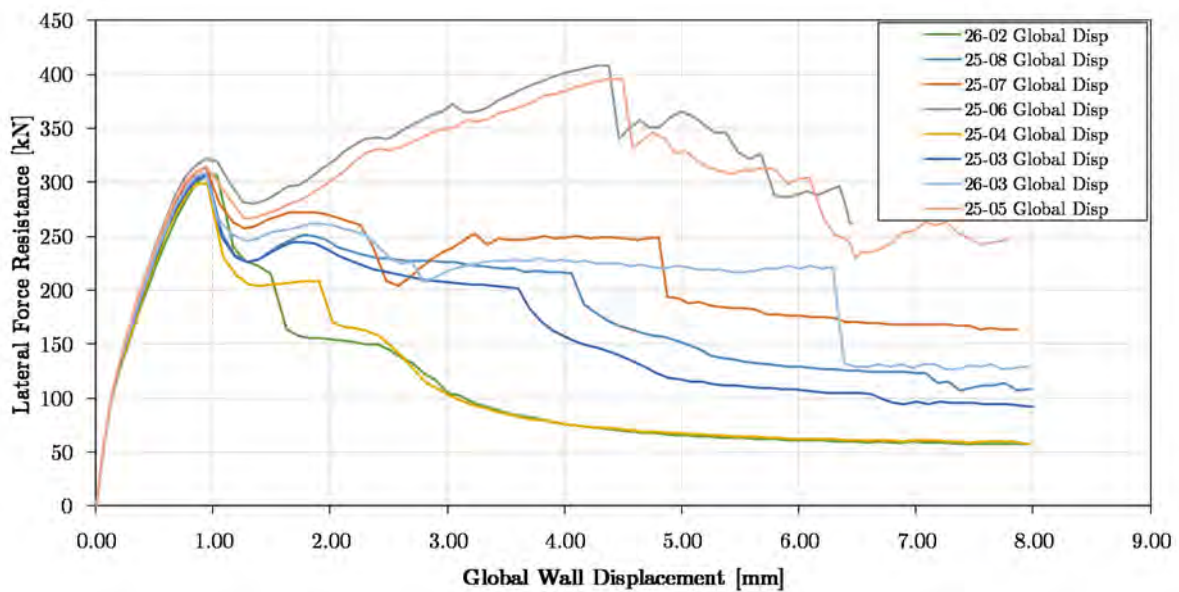
Figure 5.48: *Sensitivity to both spring stiffness and interface friction angle*

Ultimately the spring stiffness had a marginal affect on global displacement which was heavily influenced by changes of the interface friction angle. A decrease in friction angle lead to a single failure peak (FE models 26-02 and 25-04) due to slip along the horizontal connections, contrasting with the double peak failure of the higher friction angel FE models (25-06 and 25-05).

Connection Dowel Diameter

The cross-sectional area of the connection dowels at both the grouted horizontal and vertical connections was halved. 12 mm diameter dowels were replaced by 8 mm dowels in FE model 25-09 (Table (5.7)). There was an overall loss of stiffness and a lower final peak for FE model 25-09 with half the reinforcement area (Figure (5.49)). This result indicated that the model was indeed sensitive to rebar size. The lower stiffness and second peak indicated an earlier onset of dowel-action in the model and a lower ultimate failure point along the horizontal connections - as expected due to the decreased shear resistance.

Table 5.7: *Sensitivity to grouted dowel diameter*

Dowel Diameter [mm]	12	8
FE Model	25-06	25-09
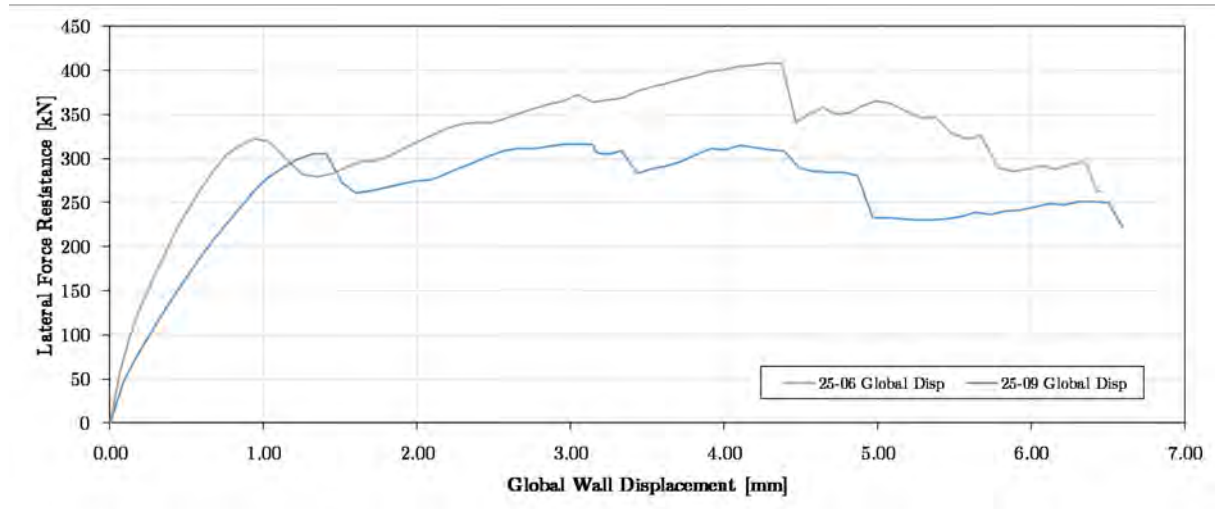
Figure 5.49: *Sensitivity to grouted dowel diameter*

5.4.2   PST 1: Structural Material, LWFC

Fracture energy, tensile strength and compressive strength of LWFC were decreased by 12.5 % and 25 % in this sensitivity study.

Fracture Energy

Both notched-beam ($G_f = 69.32 \sim 70\ N/m$) and wedge-splitting ($G_f = 18.21\ N/m$) fracture energy values for mix 8 of Grafe (2017) were tested and reduced by 12.5 % and 25 %. The respective FE models are summarised in Table (5.8) and the global displacement curves are plotted in Figure (5.50).

Table 5.8: *Sensitivity to LWFC fracture energy*

Spring Stiffness [kN/mm]	200				
Friction Angle [deg]	45	45	45	45	45
Fracture Energy [N/m]	70	61.25	52.5	18.21	15.94
FE Model	25-06	26-04	26-05	26-01	26-06

In contrast to what was expected, a drastic decrease in fracture energy tended to give an increased peak lateral force as shown by FE models 26-01 and 26-06 in Figure (5.50). In addition, initial stiffness changes were observed for the various FE models in Figure (5.50). High variability was shown between results and the sensitivity of fracture energy alone was deemed inconclusive. It was later realised that both fracture energy and tensile strength would need to be changed together to gain an accurate understanding on the sensitivity of this material property.
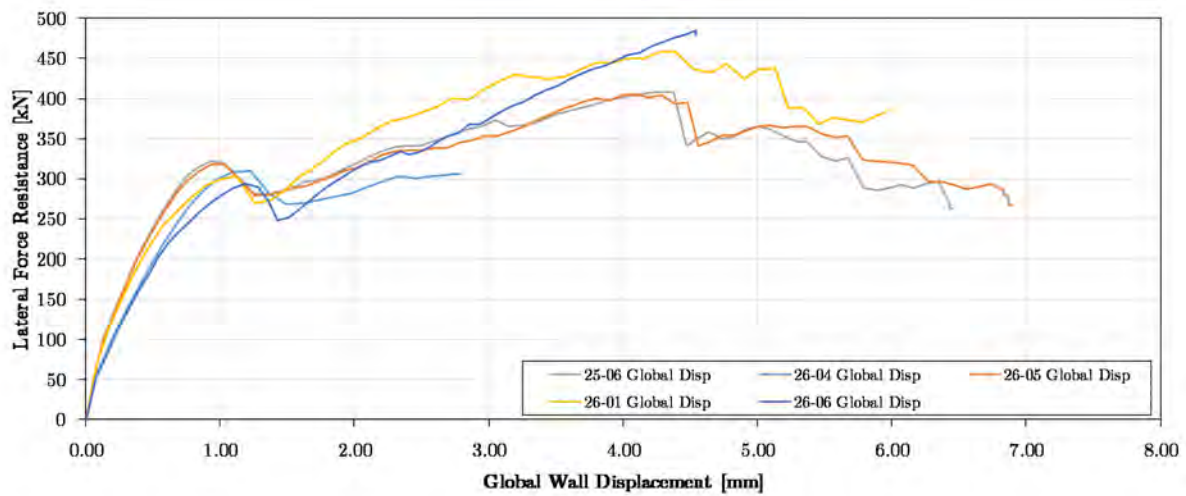
Figure 5.50: *Sensitivity to LWFC fracture energy*

Another problem identified with low fracture energy, high tensile strength models was that the maximum element size criterion could be exceeded (Section (4.9.6) and Van Zijl (2000)). This was seen to be true for analysis 26-06 which had a maximum element size of 0.01 m^2, smaller than the 25 $mm \times$ 25 mm, 0.03 m^2 elements used.

Tensile Strength and Fracture Energy

A reduction in both the tensile strength and related fracture energy was performed while again providing a difference in spring configuration. The FE models developed are detailed in Table (5.9).

Table 5.9: *Sensitivity to LWFC tensile strength and fracture energy*

Spring Stiffness [kN/mm]	200				50, 100 and 200			
Friction Angle [deg]	45	45	45	45	45	45	45	45
Fracture Energy [N/m]	70	61.25	52.5	18.21	70	61.25	52.5	18.21
Tensile Strength [MPa]	1.41	1.23	1.06	0.37	1.41	1.23	1.06	0.37
FE Model	25-06	26-09	27-02	27-03	25-05	26-07	N/A	27-04

Spring configuration had a notable effect on the shape of the force-displacement curves in Figure (5.51) where a varied spring configuration (FE models 25-05, 26-07 and 27-04) lead to a rounder second peak and possibly indicated a gradual failure of these models. An interesting result of the decreased fracture energy was that of models 27-03 and 27-04 where the peak force was higher than the final FE model (25-06). It is hypothesised that this increased peak was due to a greater activation of the rebar mesh within the now weaker LWFC. The relatively low fracture energy and average tensile strength of LWFC proved challenging to successfully analyse to full computational convergence.
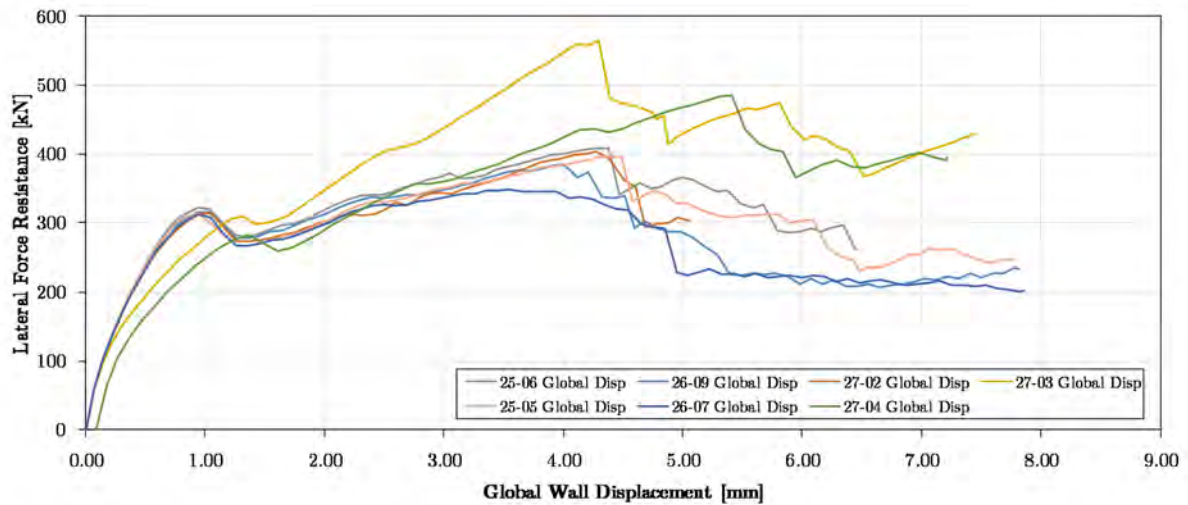
Figure 5.51: *Sensitivity to LWFC fracture energy*

Compressive Strength

Compressive strength was decreased by 25 % and reduced to the value of 12.5 MPa, determined by Grafe (2017) for mix 8, for both spring configurations. The various FE models are detailed in Table (5.10) and the results curves are plotted in Figure (5.52).

Table 5.10: *Sensitivity to LWFC compressive strength*

Spring Stiffness [kN/mm]	200			50, 100 and 200		
Friction Angle [deg]	45	45	45	45	45	45
Fracture Energy [N/m]	70	70	70	70	70	70
Compressive Strength [MPa]	22	16.5	12.5	22	16.5	12.5
FE Model	25-06	27-11	27-10	25-05	27-09	27-08
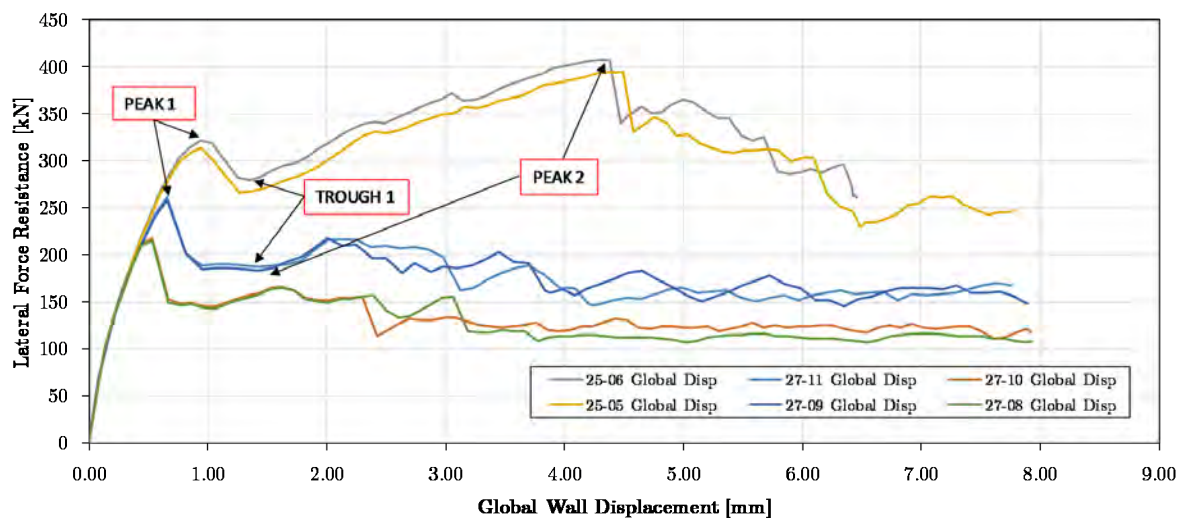
Figure 5.52: *Sensitivity to LWFC compressive strength*

The FE model is shown to be highly sensitive to compressive strength. Each force-displacement pair in Figure (5.52) has a lower initial peak in relation to the decrease in compressive strength. It is interesting to note that the global stiffness, gradient of the initial slope of the curve, is the same for each model but peaks sharply for the lower strength models and could indicate localised crushing. Another distinct difference between the models is the differing second peak force-displacement values. For the high strength models (25-05 and 25-06), the second peak is higher than the first, however this same peak is almost non-existent for the weaker models.

A possible explanation for this marked effect of compressive strength on the FE models is that compressive strength enhances dowel-action and is directly related to the crushing of LWFC at the grouted connections. For low-strength models the rebar is immediately activated and exposed to higher stresses which contrasted with the high strength models where the concrete and rebar deformed together in better combination. The relationship between reinforcement bond-strength and compressive strength should be investigated further.

Figures (5.53), (5.54) and (5.55) correlate with the vertical stress state for FE model 25-06 at the respective peak 1, trough 1 and peak 2 force displacement points in Figure (5.52). These distinct displacement regions show the progression of peak compressive stress throughout the FE analysis 25-06. Initially the compressive stress is concentrated (blue) at the protruding rebar for peak 1 as dowel action of the rebar has begun to crush the nearby concrete. This same stress increases for trough 1 and shows crushing and displacement of the top NWC panel. The final peak 2 stress is higher than both peak 1 and trough 1 and is concentrated at the toe on the right-hand-side of the lower horizontal connection. This stress concentration at the toe was observed during physical testing and resulted in crushing of the lower NWC panel.

In comparison, Figures (5.56), (5.57) and (5.58) represent the same points for the weaker FE model, 27-11 which had a 25 % reduction in compressive strength and the same rebar placement. For this analysis there are distinctly lower compressive stresses developed and a reduction in the ductile failure of the dowel connections. The reduction in peak stresses confirms the overall weaker response in Figure (5.52). Consequently this sensitivity study explains that compressive strength has a large influence on the observed failure mechanisms and achievable ductility of the wall.
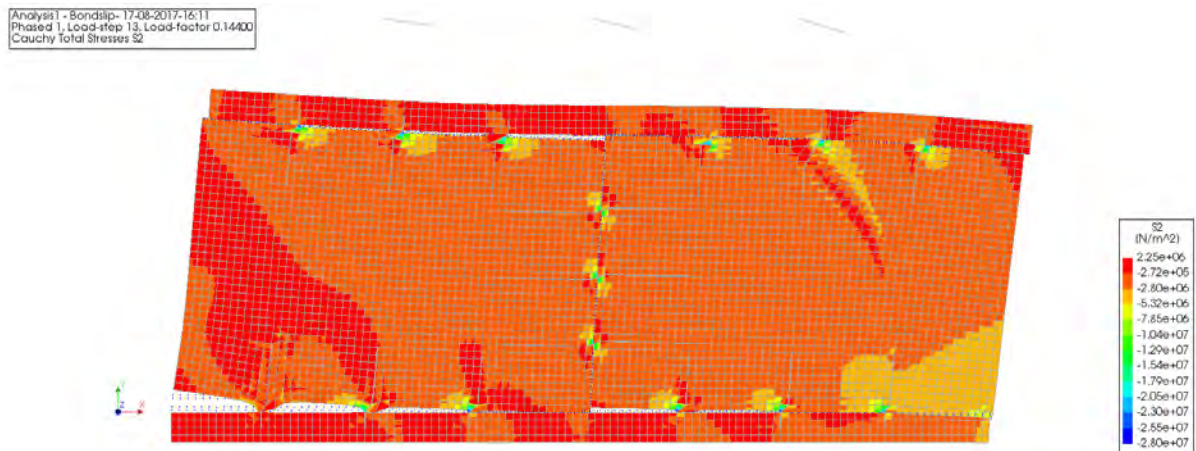
Figure 5.53: *Sensitivity to LWFC compressive strength: 25-06, Peak 1 Compressive Stress Distribution*
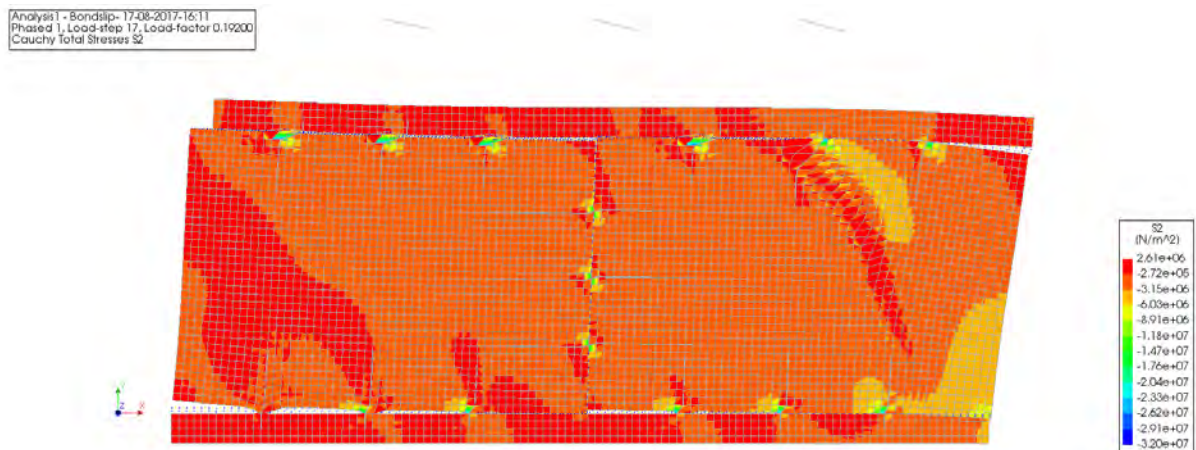
Figure 5.54: *Sensitivity to LWFC compressive strength: 25-06, Trough 1 Compressive Stress Distribution*
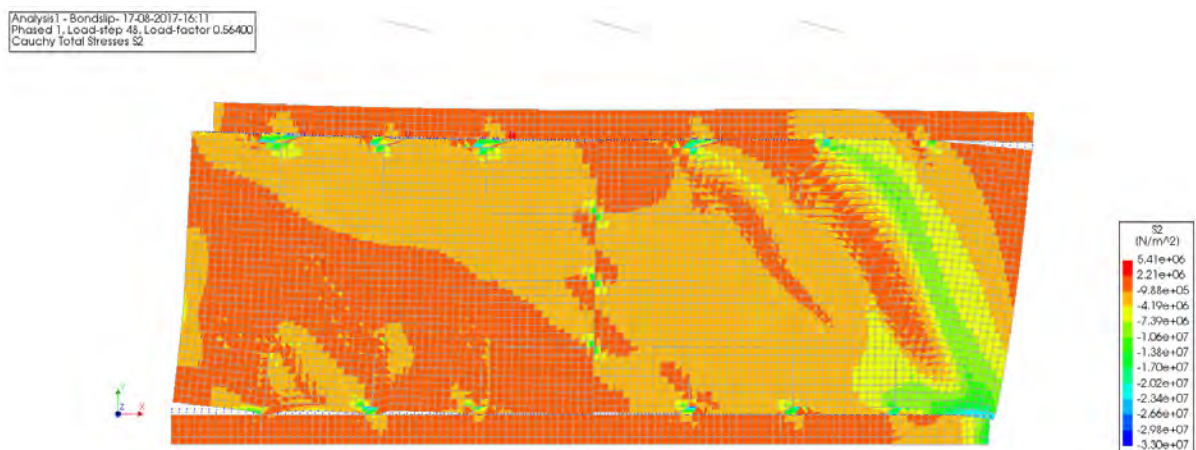
Figure 5.55: *Sensitivity to LWFC compressive strength: 25-06, Peak 2 Compressive Stress Distribution*
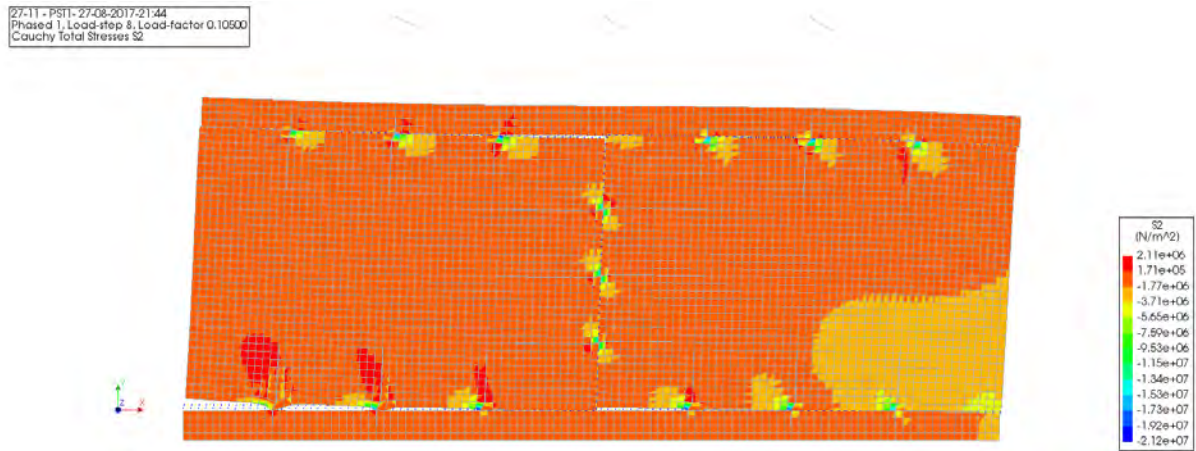
Figure 5.56: *Sensitivity to LWFC compressive strength: 27-11, Peak 1 Compressive Stress Distribution*
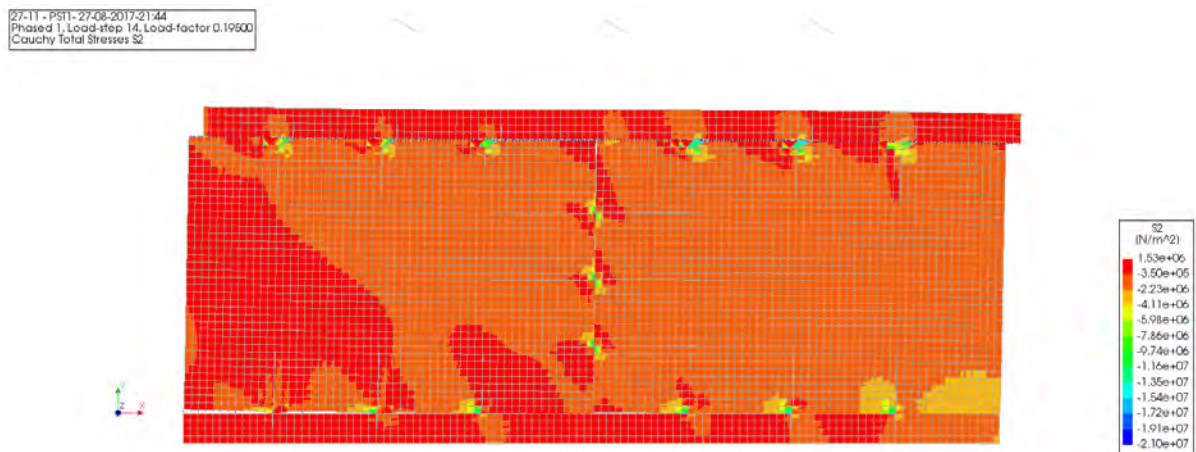
Figure 5.57: *Sensitivity to LWFC compressive strength: 27-11, Trough 1 Compressive Stress Distribution*
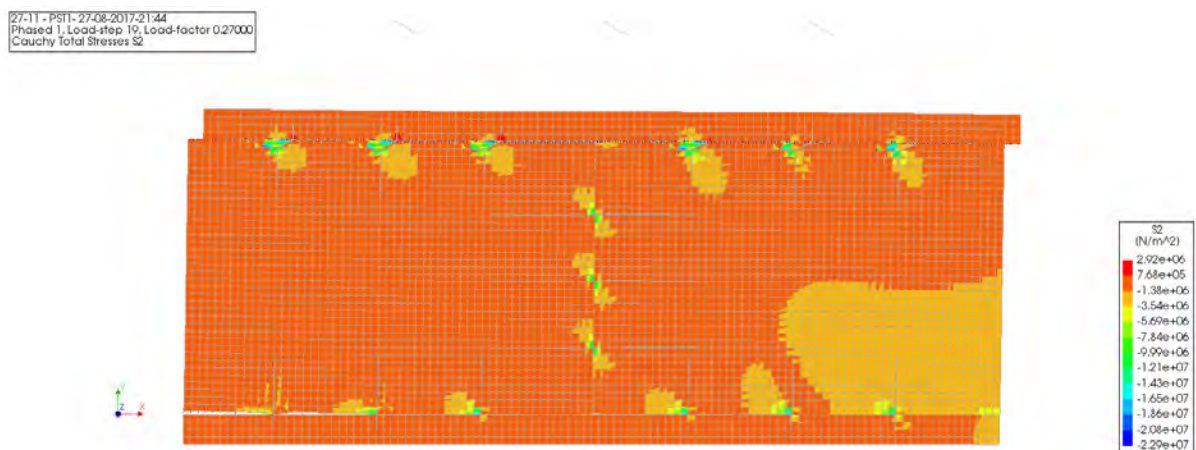
Figure 5.58: *Sensitivity to LWFC compressive strength: 27-11, Peak 2 Compressive Stress Distribution*

5.4.3 PST 3: Spring Stiffness

A limited sensitivity study was performed on PST 3 where the spring stiffness was varied to confirm if a stiffness of 200 kN/mm throughout (as per final FE model, 25-06) should be continued for PST 3.

The results of the two FE models (Table (5.11)) are presented in Figure (5.59). Both curves had similar stiffness and peak force values, however model 05-01 indicated drastic failure after peaking a second time. This was in contrast to the gradual and continued displacement of the stiffer FE model (28-01). FE model 05-01 was selected as the final FE model for PST 3 since the final peak shape and value realistically demonstrated the enhanced slip and dowel-action, shear failure at the horizontal connections. This failure method was expected for PST 3 and was demonstrated during the physical tests (Section (5.1.3)). Thus the spring stiffness of the FE model for PST 3 was reduced to 100 kN/mm.

Table 5.11: *Sensitivity of FE model PST 3 to spring stiffness*

Spring Stiffness [kN/mm]	200	100
FE Model	28-01	05-01
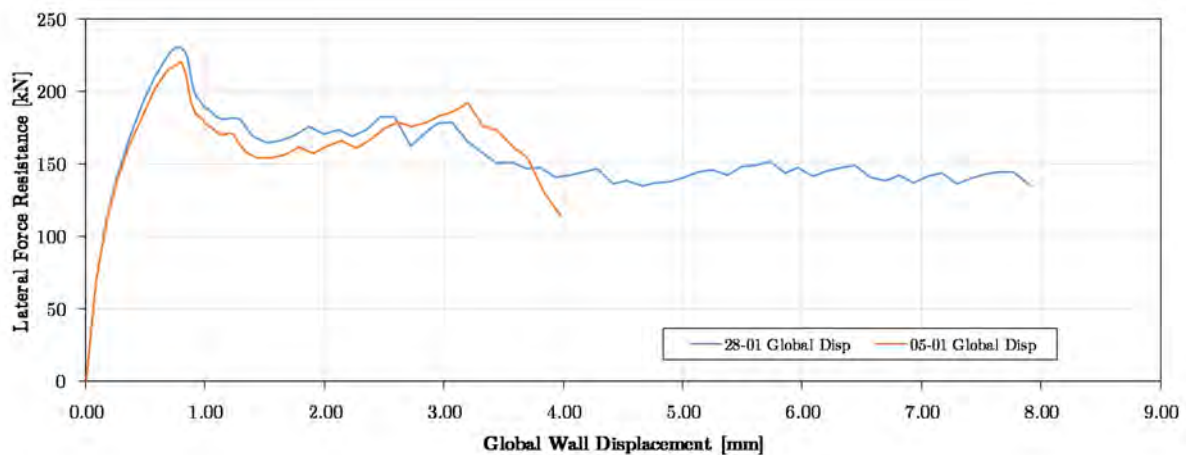
Figure 5.59: *Sensitivity of FE model PST 3 to spring stiffness*

5.5 Connections

5.5.1 Horizontal, Grouted Connections

The final cracked state of quasi-static, cyclic tests PST 2 (Figure (5.60)) indicates good symmetric cracking of the tested wall. It is evident from this crack layout and that of PST 1 and 3 in Figures (5.38) and (5.43), that the cracks emanated from the grouted rebar at the horizontal connections but the deformation was focussed in the LWFC panels themselves.

The design method of Crisafulli *et al.* (2002) focussed on placing less reinforcement across the grouted connections and more reinforcement for flexure within the wall panels as discussed in Section (2.3.4).

Figure 5.60: *Final cracked state for physical test, PST 2*

In the physical tests the two layers of reinforcement mesh were of similar ($678 \ mm^2$) cross-sectional area to the grouted rebar across the horizontal connections. In the cracked walls and the cracked FE models (Figures (5.37) and (5.42)), well placed grid reinforcement distributed the deformation in the walls beyond the connections and across the LWFC panels. In combination with this deformation distribution is the overall slip failure at the horizontal connections due to little reinforcement across the horizontal connections.

Even though the reinforcement design was not in perfect agreement with the theory of Crisafulli *et al.* (2002), the results of the cracks and deformation at the horizontal connections agree with the limited ductility design response suggested for lightly reinforced precast rectangular wall panels.

5.5.2 Vertical, Bolted Steel Connection Boxes

The bolted steel connection boxes at the vertical connections successfully provided limited movement as required for overall ductility in the connected walls.

In Figures (5.22) and (5.23) a comparison was made between the vertical displacement of each LWFC panel (at the vertical connection) for the two physical tests. The difference between the displacements on each of these graphs is the differential vertical movement at the vertical connections, enabled by the slotted holes in the connection boxes and ductility of the steel. For PST 1 (Figure (5.22)), an approximate slip of 5 mm was measured. This movement correlated well with the connection box design in Appendix (A), where the 16 mm (M16) bolt was placed at the centre of a 36 mm slot which allowed for at maximum 10 mm vertical displacement in either direction. Under the applied displacement it is understandable that the total 5 mm movement was less than the maximum 10 mm as all three connection boxes had to be activated and displace together.

This positive result is comparable to the LSB connections described in Section (2.3.2) which allowed for movement in precast structures under seismic load (Pall *et al.*, 1980).

5.6   Seismic Resistance Comparison

The equivalent static lateral force procedure outlined in SANS 10160-4:2017 SANS (2017) was used to determine the seismic base shear on the chosen LWFC prototype house on 1:3 scale. The primary reason for this calculation was to determine the sustained vertical load to be applied to the physical scale test walls during connection testing. The secondary reason was to gauge the susceptibility of the structure to seismic loads and to calculate the lateral force resistance required per storey level.
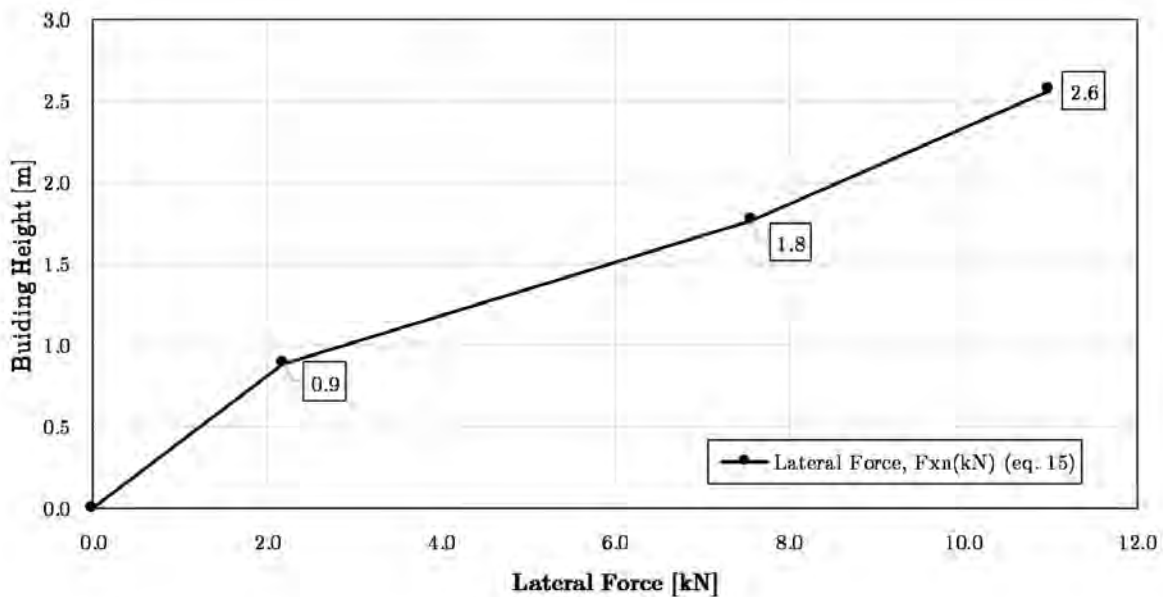
Figure 5.61: *Lateral force calculated for seismic analysis per storey height according to SANS 10160-4:2017 (SANS (2017)) §8.0*

Figure (5.61) shows the lateral force on the scaled building storey heights of 0.9 *m*, 1.8 *m* and 2.6 *m* for the originally 7.7 *m* tall building (Figure (3.3)). The values were calculated and displayed in Table (3.5), Section (3.2.3). The total lateral load was calculated to be approximately 20 *kN* and varies slightly, depending if the cured (1400 kg/m^3) or cored (1579 kg/m^3) density is used.

In comparison, this scaled lateral load is in order of $5 - 15\%$ of the applied total forces via connection testing ($132 - 240\ kN$) and FE element model lateral forces of $220 - 408\ kN$.

This single comparison leads to a conclusion that the LWFC walling system herein presented is strong enough to withstand moderate seismic loads. It is however important to understand that this single comparison is not enough to guarantee a seismically stable LWFC structure due to the scaled, simplified and limited testing to date.

Chapter 6

Summary and Analytical Design

This chapter initially provides a summary of the influential parameters of the numerical analysis sensitivity study. The summary is followed by a normalised displacement comparison which attempts to better compare the nonlinear displacement regions observed at different points in the physical and numerical models. The chapter is concluded with an analytical model for determining the peak lateral force resistance of a precast LWFC wall assembly.

6.1   Sensitivity Study: Influential Parameters

This section presents a summary of the most influential sensitivity study parameters for the chosen FE model. The sensitivity study results were displayed in Section (5.4).

Friction angle had a marked effect on the force-displacement response of the PST 1 FE models. Figure (5.48) in Section (5.4.1) gave evidence for a change in nonlinear displacement regions as well as force displacement peaks when the friction angle was reduced. This result emphasises the need for a good understanding on the actual friction along the connection which may necessitate further testing.

The reinforcement dowel cross-sectional area was halved to compare the sensitivity of the FE models. Figure (5.49) shows that there is an overall loss of strength and a 25 % lower final peak for FE model 25-09 with half the reinforcement area now across the connections. This predictable response is important and shows that the FE model connections rely on the reinforcement dowels, as demonstrated by the physical tests.

The initial fracture energy reduction sensitivity analysis of Section (5.4.2) did not provide reliable data. It was later found that this was due to too large an element size (according to Equation (4.5)) in one of the analyses. The pure fracture energy reduction tests were followed by a simultaneous reduction of both tensile strength and fracture energy in Section (5.4.2). These test results indicated that a decrease in fracture energy would result in lower initial stiffness, but higher peak forces at the maximum displacement (Figure (5.51)). It was hypothesised in Section (5.4.2) that this could be due to the now weaker LWFC which enables the stronger reinforcement mesh within the LWFC panel to be activated, and sooner play a role in the resistance of the LWFC wall, thereby increasing the final peak force-displacement values. A final interesting comparison is the different peak values of analyses 27-03 and 27-04 which had the same, reduced fracture energy but had different

111

spring arrangements (Figure (5.51)). The stiffer arrangement of 27-03 led to a significantly higher final peak force of 670 kN in comparison to the 485 kN peak of 27-04. Only at this low ($G_f = 18.21$ N/m) fracture energy did the spring stiffness's have a significant influence on the force deflection curves. It is hypothesised that the low fracture energy and reduced overall strength allowed for greater movement of the wall panels and increased the effect of displacement springs due to a likely increase in vertical displacement.

The final influential FE sensitivity study parameter is compressive strength. In the sensitivity study compressive strength was initially reduced by 25 % of the final FE model (22 MPa) value and was decreased further to the 12.5 MPa compressive strength value achieved by Grafe (2017). Figure (5.52) displays multiple differences between the full and reduced strength models. Apart from the distinct decrease in second peak force-displacement values, the first peak shape and value also changed for the reduced compressive strength models, reducing the first peak by roughly 33 % for the weakest model. The lower and sharper first peak indicates weaker dowel resistance due to the lower compressive strength. Here the initial lifting and rotation of concrete panels was reduced, visualised by comparing Figures (5.53) and (5.56) which show a reduction in compressive stress at the dowel connections for the reduced compressive stress FE model 27-11. Considerable reduction in the second peak force-displacement value indicates a change in the observed toe-crushing behaviour. The weaker FE models show a decrease in dowel action and rotation, focussing the failure mechanism at the top horizontal connection. This contrasts greatly with the stronger models, where the peak 2 failure mechanism is a combination of dowel action at the horizontal connection and crushing at the toe; indicated by the comparison of Figures (5.55) and (5.58). Ultimately this sensitivity parameter gave a good indication of the ductility provided by the compressive strength of the wall, reinforcing the idea that a strong, shear resistant wall is essential to obtain full use of the precast connections.

6.2   Normalised Displacement Comparison

In this section the results of the physical tests and final FE model are compared on a normalised scale to show agreement in relative stages at which the inelastic displacement mechanisms arose. The importance lies in the design objective to mobilise and balance as many as possible mechanisms of inelasticity, especially those of highly ductile, energy dissipative nature, for appropriately safe response to seismic excitation. These mechanisms represent the stages of displacement change for each of the tests and were identified in the interpretation section of the results of the physical tests, Sections (5.1.1) and (5.1.3) for PST 1 and PST 3 respectively and in the results of numerical analyses, in Sections (5.3.3) and (5.3.4).

Global displacement was chosen to be the most consistent displacement parameter for normalisation. The selected force-displacement locations, chosen for normalisation of both the global and local displacement curves, are listed in Table (6.1) for each of the analysis force-displacement curves. The points chosen were the second, "peak 2" values of the respective analyses and thus coincide at point (1.0, 1.0) for the normalised axes.

It is important for the reader to note that this comparison does not replace the preceding results which indicated differences between FE model and physical test results, but aims to provide an additional tool to understand the failure mechanisms of the walls.

Table 6.1: *Global displacement force-displacement pairs, chosen for the normalisation of each test*

Curve	Force [kN]	Displacement [mm]	Location
PST 1 - Global	200.3	11.11	Peak 2, Figure (5.35)
25-06 - Global	408.2	4.28	Peak 2, Figure (5.34)
PST 3 - Global	131.9	7.65	Peak 2, Figure (5.40)
05-01 - Global	192.7	3.20	Peak 2, Figure (5.39)

6.2.1   Normalised Displacement: PST 1 / FE Model 25-06

Figure (6.1) gives a comparison between the local and global displacement of PST 1 and the chosen final FE model 25-06. This graph is the normalised comparison of Figure (5.35). In contrast to the varying scale of the individual test results, Figure (6.1) shows an improved comparison between the global displacements of the physical and FE model.

The nonlinear displacement region (2) "initial rotation and lifting of both LWFC panels" is now seen to occur at a relative 0.32 and 0.25 of peak global displacement for PST 1 and FE model 25-06 respectively. Similarly, the first peak identified in Figure (5.35) for the PST 1 occurred at a relative local displacement of 0.18, now extremely close to the 0.17 relative value for the FE model. Nonlinear displacement region (3) "individual panel movement" shows a better visual comparison between the physical and numerical test results. As per the chosen method of normalisation, the second peak values for both global displacement curves correlate at the point (1;1).

A final comparison is the post-peak, (4) "slip" behaviour of PST 1 and FE model 25-06 which continues to vary after normalisation. Global displacement curve PST 1 indicates a displacement-hardening behaviour (black arrow in Figure (6.1)) in contrast to displacement-softening (red arrow in Figure (6.1)) of FE model 25-06. It is hypothesised that this difference in behaviour is due to the distinct limit imposed on the material strength parameters in the FE model, contrasting with the continued displacement observed in the physical tests.
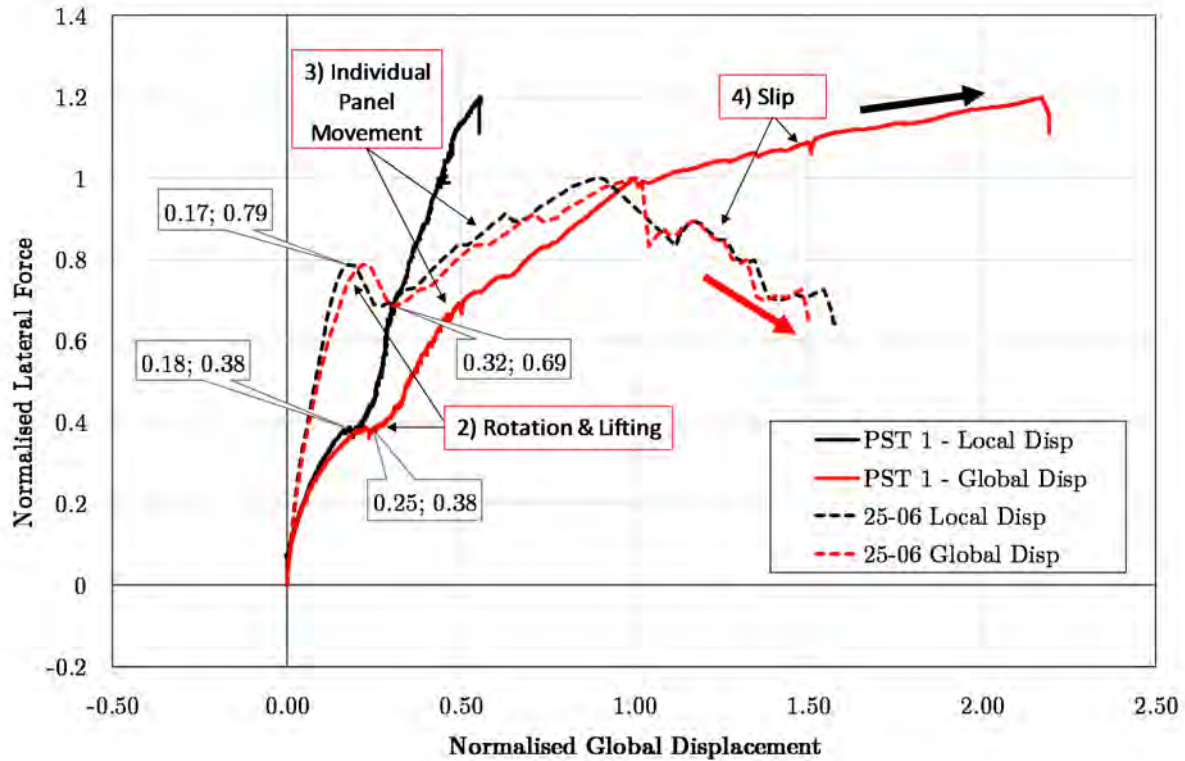
Figure 6.1: *Normalised displacement comparison for PST 1: a comparison of local and global displacement*

6.2.2   Normalised Displacement: PST 3 / FE Model 05-01

Figure (6.2) gives a comparison between the local and global displacement of PST 1 and the chosen final FE model 05-01. This graph is the normalised comparison of Figure (5.40) and gives a scaled relation of global and local displacement between PST 3 and FE model 05-01.

Figure (6.2) shows that the "first peak" identified in Figure (5.40) for PST 3 and recognised as nonlinear displacement region (1) "rotation and lifting" is achieved at the same 0.18 relative local displacement for the physical and numerical tests. The values for global displacement of PST 3 and FE model 05-01 also show a favourable comparison of 0.25 and 0.35 respectively, for the same nonlinear displacement region. These relative displacements give better visualisation than the contrasting, un-scaled displacements of 0.8 *mm* and 2.7 *mm*, for peak 1 global displacements in Figure (5.40), of FE model 05-01 and PST 3 respectively. Nonlinear displacement region (3) "slip at the horizontal connections" shows an improved correlation in this normalised comparison.
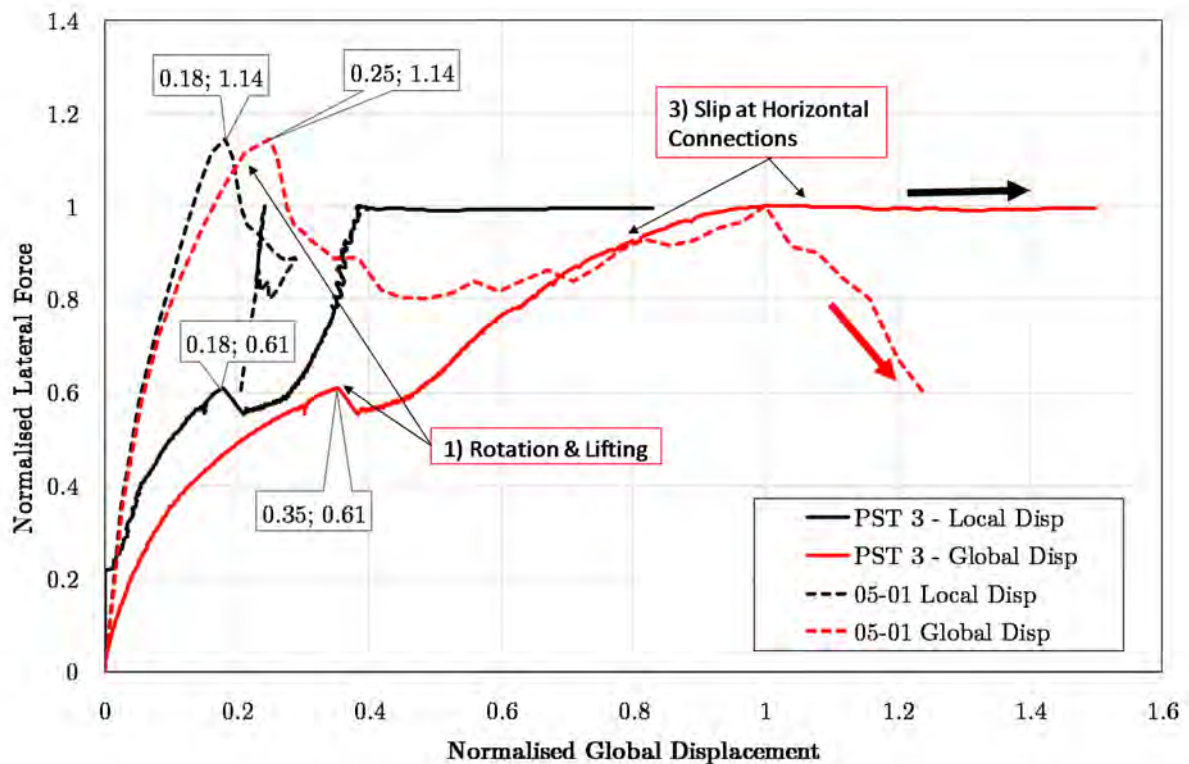
Figure 6.2: *Normalised displacement comparison for PST 3: a comparison of local and global displacement*

6.2.3 Normalised Displacement: Slip at Horizontal Connections

Figure (6.3) shows that top and bottom slip of PST 1 and FE model 25-06 follow one another closely until a high level of non-linearity is seen at the end of the initial elastic displacement. Interestingly, this nonlinear region occurs at the peak, unitary force of both PST 1 and FE model 25-06, but the relative global displacement at this point differs by a factor of four. Normalised slip in Figure (6.4) gives a better comparison between PST 3 and FE model 05-01 for top horizontal connection slip. In Figure (6.4), for the wall with fewer dowel connections, top and bottom slip follow each other closely before extreme slip is seen at the top horizontal connection in both the physical and FE tests.

Figures (6.3) and (6.4) highlight the difference in dowel action in the FE models replicating PST 1 and PST 3. The better connected PST 1 FE model did not slip as seen in the physical tests, and is directly contrasted by the FE model for PST 3. This difference in global displacement shape for the FE models can be seen between Figures (5.53) and (5.58) in the compressive strength sensitivity study.
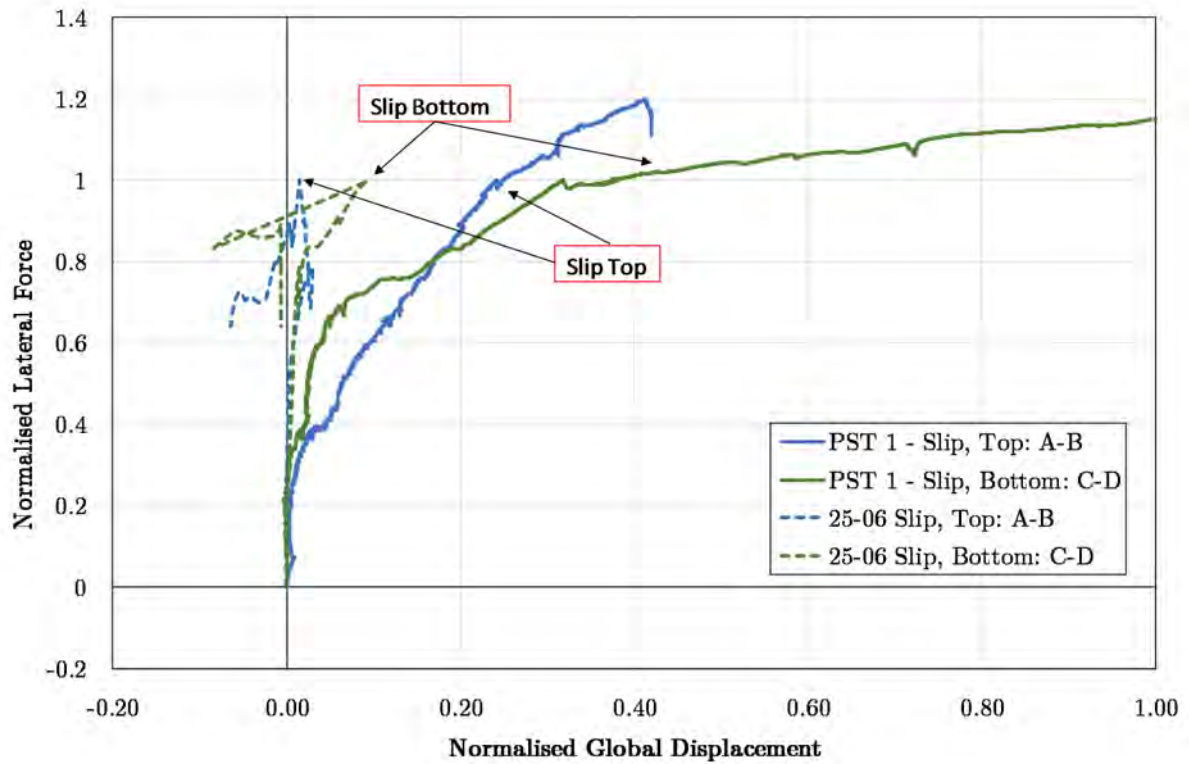
Figure 6.3: *Normalised displacement comparison for PST 1: Top and bottom slip for PST 1 and FE model 25-06.*
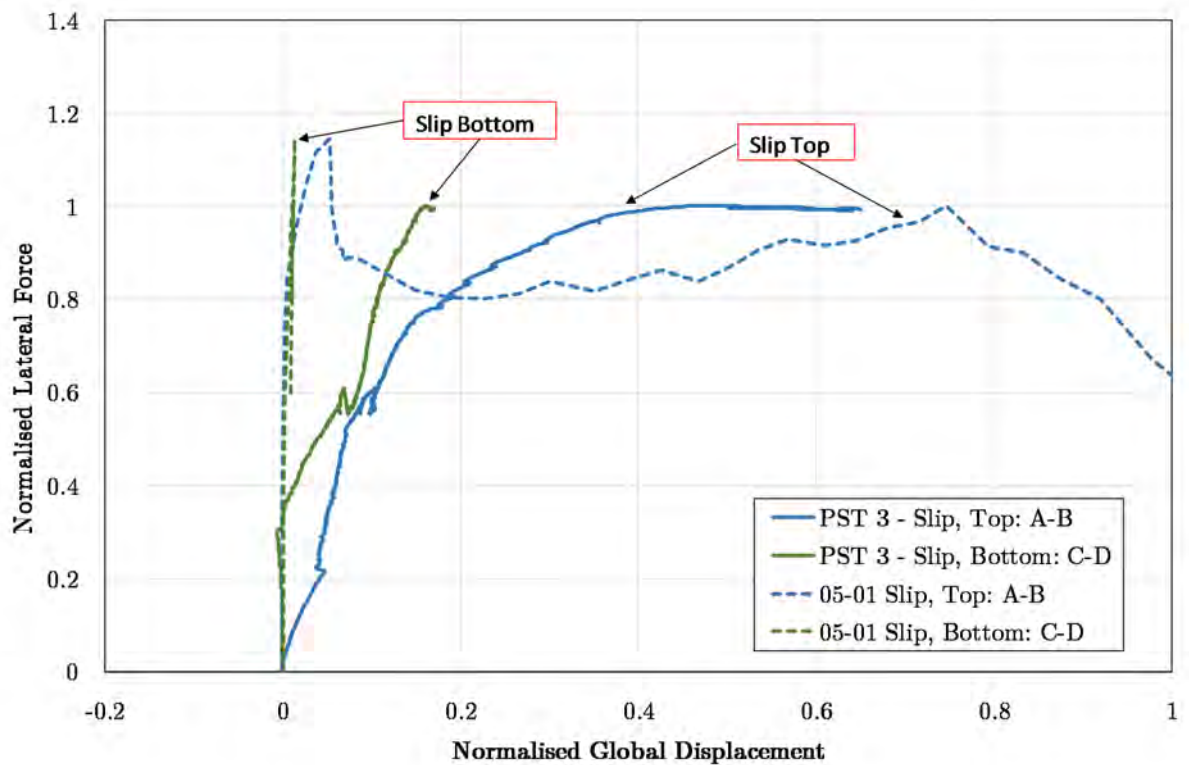
Figure 6.4: *Normalised displacement comparison for PST 3: Top and bottom slip for PST 3 and FE model 05-01.*

6.2.4   Dowel Connection Behaviour

Force-displacement curves for wall 3 (PST 3 and FE model 05-01) were normalised with reference to the peak 2 force-displacement points of PST 1 and FE model 25-06 to better visualise the effect of a change in dowel-connection behaviour. Normalising with reference to the larger force-displacement value was assumed to give a better comparison of the relative lateral force effect due to the altered dowel configuration of PST 3. The normalisation parameters used for this comparison are summarised in Table (6.2).

Table 6.2: *Normalisation force-displacement pairs for dowel connection behaviour*

Curve	Force [kN]	Displacement [mm]	Location
PST 1 - Global	200.3	11.11	Peak 2, Figure (5.35)
25-06 - Global	408.2	4.28	Peak 2, Figure (5.34)
PST 3 - Global	200.3	11.11	Peak 2, Figure (5.35)
05-01 - Global	408.2	4.28	Peak 2, Figure (5.34)

Global displacement in Figure (6.5) shows that the mechanisms of non-linearity occurred within similar global displacement regions for both PST 1 and PST 3 and that this similarity was successfully mirrored in FE models of these walls (25-06 and 05-01). Another successful comparison is the difference in normalised lateral force. PST 1 had a 34 % higher lateral force at peak global displacement with the extra dowel pair per wall panel, compared to the 42 % increase between modelled analyses 25-06 and 05-01. This comparison clearly shows the significant decrease in overall lateral resistance caused by a reduction in dowels.

In Figure (6.6) top and bottom slip are compared between the two physical tests on the new normalised scale for further comparison of the effects of a reduced number of dowels at the horizontal connections. The peak slip displacement of PST 1 was dominated by bottom slip, contrasting with the dominant top slip displacement of PST 3. This difference was possibly due to construction differences and not due to the connection design. It is thought that the weaker of the two connections would first lose adhesive bond and begin to slip. Once activated, the majority of the displacement would be concentrated at this connection. The total, top and bottom, peak slip of PST 1 relative to global displacement (1.61) was approximately four times that of PST 3 (0.42).
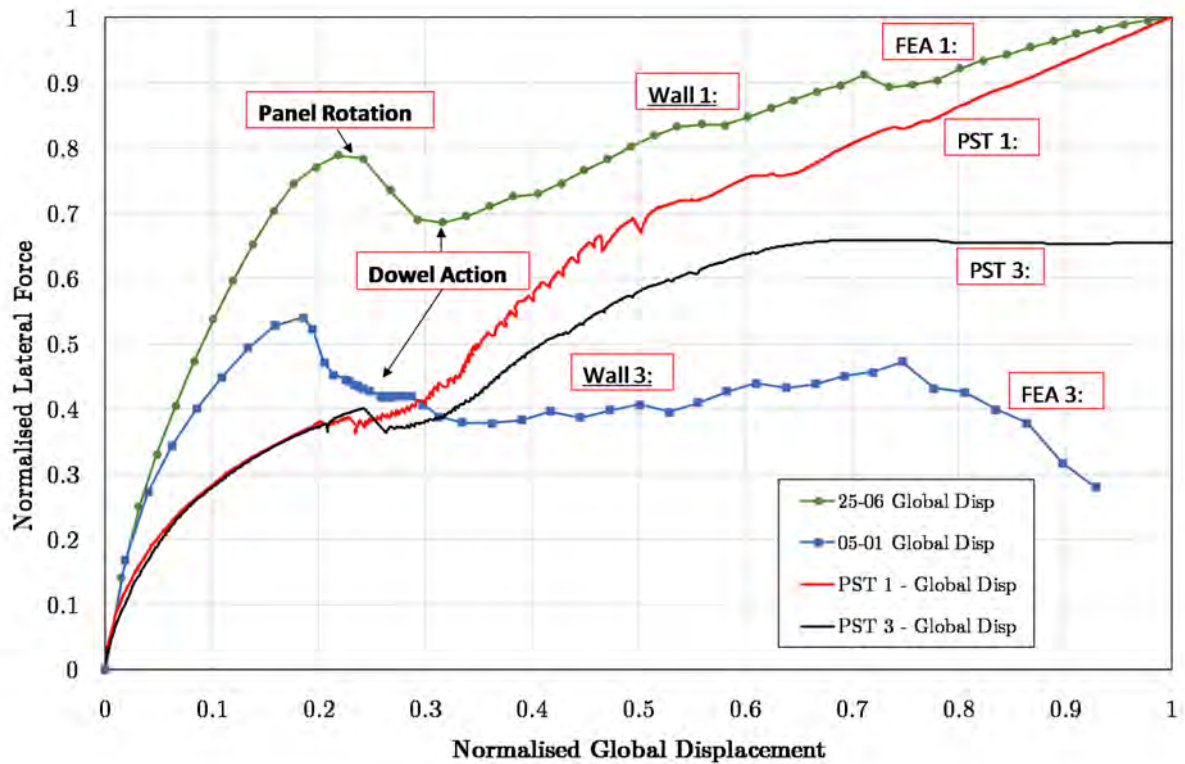
Figure 6.5: *Normalised displacement comparison of dowel connection influence: Global displacement of physical tests and FE models.*

Figure 6.6: *Normalised displacement comparison of dowel connection influence: Slip during physical tests*

6.2.5   Conclusion on Normalised Displacement Study

These normalised comparisons show that the relative displacement of both the physically tested and numerically analysed models correlate better than previously indicated. Even though the relative stiffness and total force resistances of the models do differ, the FE models were successful in replicating global and local displacement behaviour observed during physical tests, and thus in capturing the physical mecha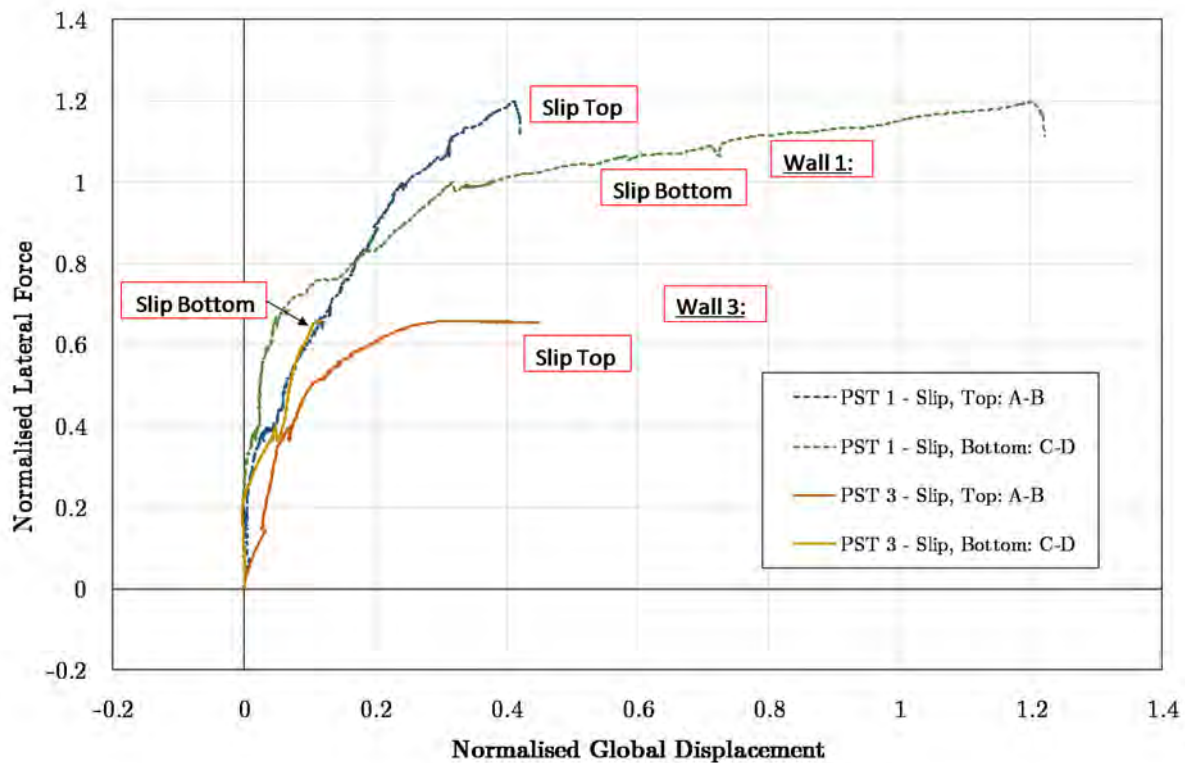nisms of inelasticity and energy dissipation. Figures (6.3) and (6.4) ultimately gave a reasonable comparison between top and bottom slip of each model, providing a relative scale that showed how top and bottom slip are close to one another while the wall is undergoing elastic displacement. Discrepancies between the FE models and physical tests in Figures (6.3) and (6.4) show that the simplified FE model connections had an effect on both the stiffness and the plastic behaviour of the FE models.

6.3   Analytical Design for Reinforced LWFC Walls

In this section an analytical design procedure is proposed for the calculation of horizontal resistance of a connected, precast and reinforced LWFC wall. This design method focusses on the theoretical shear resistance of the larger horizontal connections and is based on the results of PST 1 and 3.

During physical testing it was seen that failure of the walls under lateral, horizontal load was dominated by shear-slipping along the horizontal connections. According to fib Model Code (2010), §6.3, concrete-concrete load transfer across interfaces is dominated by three mechanisms: 1) Adhesive bonding and mechanical interlocking, 2) shear friction and 3) dowel action.

6.3.1   Adhesive bonding and mechanical interlocking

Adhesive bonding and mechanical interlocking is caused by chemical adhesion between the two surfaces. This mechanism is influenced by surface preparation and cleanliness of the surface as well as the strength of the old and new concretes (fib Model Code, 2010). In the context of precast LWFC and the test setup of Section (3.2.4), adhesion is likely to play a role in the connection resistance as masonry mortar was used to ensure full contact between the connected LWFC surfaces. Representative values for mean shear resistance due to adhesion, τ_a of normal strength concrete are between $\tau_a = 1.5 \sim 2.5 N/mm^2$ for a rough, sand-blasted interface and $\tau_a = 2.5 \sim 3.5 N/mm^2$ for very rough, high pressure jet cleaned interface.

6.3.2   Shear Friction

Shear Friction due to surface roughness and perpendicular forces to the interface has a measurable effect on the shear resistance of horizontal connections. According to fib Model Code (2010) a smooth coefficient of friction is $\mu = 0.5 \sim 0.7$ and contrasts with a very rough interface of $\mu = 1.0 \sim 1.4$. The coefficient of friction for cast LWFC panels in this study is decidedly smooth, however the confining stress σ_c created by the coil springs did increase due to panel rotation and was sustained throughout the tests. Thus the coefficient of friction chosen for the analytical design is $\mu = 0.6$.

fib Model Code (2010) §6.3.4 *Modelling and design* presents the individual mechanisms of shear transfer. Equation (6.1) (fib Model Code (2010) equation 6.3-5) represents the combined mechanism of adhesion, interlocking and shear friction.

$$\tau_u = \tau_a + \mu \cdot (\sigma_n + \kappa_1 \cdot \rho \cdot f_y) \tag{6.1}$$

Where:

τ_u is the total, ultimate shear resistance
τ_a is the adhesion, interlock shear resistance
κ_1 is the interaction ("effectiveness") factor
σ_n is the lowest compressive stress, resulting from the normal force on the interface ρ is the degree of reinforcement across the interface $\rho = A_s/A_c$ and
f_y is the reinforcement steel yield strength.

6.3.3   Dowel Action

Dowel action, the final mechanism for shear resistance at a horizontal connection, refers to the bending resistance of reinforcement bars across the connection interface. Once adhesive bonding is overcome and shear friction is active, shear displacement occurs across the interface and creates a differential displacement between the upper and lower end of the reinforcement. This differential displacement induces a bending moment within the reinforcement. In addition, as the connection opens, tensile stresses are induced on the reinforcement which limit the ultimate bending resistance (fib Model Code, 2010). This dowel action adds ductility to the shearing action, contributing to the shear resistance at large displacements.

Equation (6.2) (fib Model Code (2010) equation 6.3-6) represents the resistance, V_F to an acting shear force. This maximum dowel action is reduced to incorporate the interaction of tensile forces and bending for rough surfaces. This reduction is achieved by incorporating κ_1 in Equation (6.3) (fib Model Code (2010) equation 6.3-7).

$$V_F(s) \approx V_{F,max} \cdot \left(\frac{s}{s_{max}}\right)^{0.5} = \kappa_2 \cdot A_s \cdot \sqrt{f_{cc} \cdot f_y} \cdot \left(\frac{s}{s_{max}}\right)^{0.5} \le \frac{A_s \cdot f_y}{\sqrt{3}} \tag{6.2}$$

Where:

$V_{F,max}$ is the maximum value of dowel action
s_{max} is the slip when $V_{F,max}$ is reached, $s \le s_{max} \approx 0.1 \cdot d_s \sim 0.2 \cdot d_s$
κ_2 is the interaction coefficient for flexural resistance

$$V_F(s) = V_{F,max} \cdot \left(\frac{s}{s_{max}}\right)^{0.5} \cdot \sqrt{1 - \left(\frac{\sigma_s}{f_y}\right)^2} = V_{F,max} \cdot \left(\frac{s}{s_{max}}\right)^{0.5} \cdot \sqrt{1 - \kappa_1^2} \tag{6.3}$$

Where:

$\kappa_1 = \sigma_s / f_y \leq 1.0$

6.3.4 Combined Influence Along Horizontal Interface

The combined effect of all three mechanisms is not a clear superposition of the most extreme cases of each, but rather a careful combination of all three. fib Model Code (2010) §7.3.3.6 gives an example for shear at the interface between concrete cast at different times. Considering the previously conducted physical tests, the connection interface was intersected by grouted dowel reinforcement. The prescribed shear stress design limit value, τ_{Rdi} is given by Equation (6.4), equation 7.3-51 in fib Model Code (2010). In this combination, chemical adhesion was neglected and the shear resistance focussed on aggregate interlock and friction effects.

$$\tau_{Rdi} = c_r \cdot f_{ck}^{1/3} + \mu \cdot \sigma_n + \kappa_1 \cdot \rho \cdot f_{yd} \cdot (\mu \cdot \sin\alpha + \cos\alpha) + \kappa_2 \cdot \rho \cdot \sqrt{f_{yd} \cdot f_{cd}} \leq \beta_c \cdot \nu \cdot f_{cd} \quad (6.4)$$

Where:

c_r is the coefficient for aggregate interlock effects at rough interfaces
α is the inclination of the reinforcement crossing the interface
β_c is the coefficient for the strength of the compression strut
f_{ck} characteristic value of compressive strength of concrete
f_{yd} design yield strength of reinforcing steel in tension
f_{cd} design value of the cylinder compressive strength of concrete, and
$\nu = 0.55 \left(\frac{30}{f_{ck}} \right)^{1/3} \leq 0.55$

6.3.5 Analytical Model: PST 1 and PST 3

An iterative study was conducted, using the parameters previously mentioned to determine a likely combination of friction and dowel action for the analytical model presented. After consulting fib Model Code (2010) Table 7.3-2 for coefficients of different surface roughness, it was seen that the smooth surface assumption held for the analytical representation of design shear stress for PST 1 and PST 3. The friction coefficients used to calculate the design shear stress for the horizontal connection are summarised in Table (6.3). In this analytical design, the effect of aggregate interlock c_r and chemical adhesion τ_a were neglected, based on the assumption that their contribution to shear resistance would be lost once dominant friction and dowel action took place. The friction coefficient was chosen to be $\mu = 0.6$. The six grouted Y12 rebar had a degree of reinforcement crossing the interface of $\rho = 0.16$ % for PST 1 and were assumed to be vertically placed.

The shear stress design limit value was calculated according to Equation (6.4) to be $\tau_{Rdi} = 0.488\ MPa$. Based on the connection area, selecting the cross-sectional wall area to be $2.76\ m \times 0.15\ m = 0.414\ m^2$, the shear force resistance per connection for PST 1 is calculated to be approximately $202\ kN$. Following the same assumptions, this force resistance decreases as expected for PST 3 to $140\ kN$, which has a lesser degree of reinforcement crossing the interface, $\rho = 0.11$ %.

Table 6.3: *Material factors for interface behaviour*

c_r	0	f_{ck}	20	MPa	σ_n	0.065	MPa
μ	0.6	f_{yd}	520	MPa	ρ	0.16	$\%$
κ_1	0.5	f_{cd}	22	MPa	ν	0.55	
κ_2	1.1	α	90	deg	β_c	0.4	MPa

6.3.6 Analytical Model: Lateral Force Resistance of Reinforced LWFC Walls

It was important to compare the results of the physical tests in Section (5.1), and the numerical models in Section (5.3) to determine this simplified model for predicting the lateral force resistance of reinforced LWFC wall panels. The proposed analytical model focusses on the resistance of a single horizontal connection. However it is shown in Table (6.4) that the peak forces of the analytical model correlate well with the peak force values of the physical tests, decreasing as expected for model PST 3 with fewer dowel connections. Additionally, the analytical model predictions are 20 % lower than PST 1 and 6 % higher than PST 3, *leading one to draw a conclusion that the resistance of one horizontal connection governs the capacity of the wall.*

In the FE model, both the upper and lower horizontal connections are perfectly symmetric and with exactly the same strength and stiffness. In contrast, for the physical tests, construction tolerances could lead to a difference in shear resistance of the two connections and the capacity of the wall would be limited by the weaker of the two connections. Thus it is hypothesised that for the physical connections, failure is dominated by a single connection and is similar to the results of the horizontal connection analytical model. This is contrasted with the numerical model which distributes the load and deformation better.

Table 6.4: *Summary of peak lateral forces*

	PST 1	PST 3
Physical Peak [kN]	240	132
Numerical Peak [kN]	408	220
Analytical Peak [kN]	202	140

The proposed analytical model for physical test lateral force prediction is that of Equation (6.5). This revision of Equation (6.4) neglects aggregate interlock and assumes that capacity of the wall is limited by the shear stress design limit of a single horizontal connection. This analytical model focusses on a combination of friction and dowel action and shows a relationship between shear strength and the degree of reinforcement across the connection interface.

$$\tau_{Rdi} = \mu \cdot \sigma_n + \kappa_1 \cdot \rho \cdot f_{yd} \cdot (\mu \cdot \sin\alpha + \cos\alpha) + \kappa_2 \cdot \rho \cdot \sqrt{f_{yd} \cdot f_{cd}} \leq \beta_c \cdot \nu \cdot f_{cd} \qquad (6.5)$$

Chapter 7

Conclusion and Recommendations

This chapter concludes the thesis and explains the relevant findings with reference to the objectives and research focus set out in Chapter 1. The chapter is concluded with a list of recommendations for future research on the topic of reinforced LWFC building systems.

7.1 Summary

This research was conducted to systematically evaluate lightweight foam concrete as an appropriate construction material for precast walling systems for low-rise residential infrastructure in low to moderate seismic regions. The ultimate goal was to propose design guidelines for such structural systems.

It was decided that three different physical tests would be conducted on LWFC wall assemblies. The first test, PST 1, would be the benchmark test and would be fully connected at the vertical and horizontal connections. The second test, PST 2 would contrast with PST 1 by virtue of the applied, quasi-static, load. The third and final full-scale test, PST 3 would differ from PST 1 by decreasing the number of grouted rebar across the horizontal connections.

To design the physical tests, and to extend the physical wall test results and scope, numerical analyses of the physical tests were performed. A preliminary FE model was developed before the final physical tests were conducted and provided preliminary data that aided in physical testing. The focus of the FEA was to capture mechanisms of inelasticity, i.e. friction and slip in wall-foundation, wall-floor and wall-wall interfaces, diagonal cracking in the LWFC walls, and crushing of the wall toes and at connecting dowels.

PST 1 displayed four distinct nonlinear regions and differed from PST 3 as expected due to its reduced number of dowel connections. Both the scale of displacements as well as the peak lateral force resistance were lower for the less connected PST 3. Slip was seen at the vertical connection boxes during PST 1. This slip allowed for displacement of the individual wall panels in PST 1 and was not seen in PST 3 where both panels remained connected. In PST 3, the vertical connection was therefore seen to be dominant .

The results of PST 2, which was similarly connected and reinforced to PST1, but loaded cyclically to simulate seismic excitation, were used to establish the energy dissipating

ability of the LWFC walling system under seismic load. A quasi-static load was applied to the wall setup of PST 1 in accordance with a precast connection testing guideline. Energy dissipation histograms were created for each push-pull half-cycle for both global and local displacement. The energy dissipation histograms were normalised to show a comparison over the test duration, indicating a consistent global displacement energy dissipation and a gradual increase in local displacement energy dissipation. Overall it was concluded that energy dissipation though various mechanisms of inelasticity are required for appropriate behaviour under seismic load.

Characterisation test results were used to calibrate the updated LWFC material model, allowing the final FE model to better represent the physical tests performed. The numerical analyses of PST 1 and PST 3 displayed similar displacement mechanisms to their physical test counterparts but differed with regards to force-displacement curve shape, ultimate displacement at failure and lateral force resistance. Although the numerical results differed, the analyses were considered successful through a comparison of crack patterns and inelastic deformation mechanisms observed during physical testing.

The normalisation comparison of Chapter (6) compared the nonlinear displacement mechanisms observed in both the physical and numerical test results. This comparison showed that these mechanism occurred at the same relative displacement for each of the respective tests. This justified extrapolation of the physical wall results by computational studies of the wall response sensitivity to LWFC compressive and tensile strength and fracture energy, dowel diameter, and interfacial friction. Chapter (6) was concluded with a proposed analytical design for reinforced LWFC walls based on the physical wall responses and computational sensitivity studies, and design standards for regular structural concrete in modular structural systems. The proposed analytical design made use of shear friction and dominant dowel action; which were seen in the FE sensitivity study to have the greatest effect on lateral force-displacement response for the modelled walls. Results from the analytical model indicated that the shear capacity of a single horizontal connection governed the capacity of the physically tested wall.

7.2 Conclusions

7.2.1 Physical Tests

Sound wall behaviour under lateral load: Two reinforced LWFC walls were precast and connected via mechanical and grouted dowel connections. The walls were tested under in-plane lateral load and showed sound wall behaviour, illustrated by multiple cracks and observed displacement mechanisms.

Precast wall connection dependence: The two walls differed by manner of grouted horizontal connection. The wall with fewer dowels crossing the horizontal connections had a reduction in lateral load capacity and lower deformation due to fewer diagonal cracks; clearly showing the influence of connections on lateral force capacity

Energy dissipation behaviour: A third wall was tested under quasi-static cyclic loading to understand the energy dissipation behaviour of the precast connected precast wall. It was seen that a combination of both global and local displacement contributed to effective energy dissipation within the wall. Thus it is concluded that the degree of energy dissipation is dependent on connection placement and layout.

7.2.2   Numerical Analysis

Preliminary LWFC material FE model: A preliminary LWFC material and FE model was established; based on literature understanding and previous test results from within the research unit. This preliminary study gave confidence to the physical test design, test method, test sensitivities and expected results.

Final FE model: The final FE model gave a better representation of the physical test setup and boundary conditions. The final FE model aimed to both confirm and allow for extrapolation of the physical test results. The results of the FE model did not directly align with those of the physical tests, but displayed similar regions of nonlinear displacement. In addition, the detailed results of the FE models gave valuable information regarding the failure mechanisms within the connected wall.

Finite element sensitivity study: A FE sensitivity study was conducted to understand dependence of the final FE model to changes in interface friction, dowel size, tensile strength and compressive strength. Decreased interface friction led to greater slip at the horizontal connections and overall lower lateral resistance. Changes to compressive strength highlighted the dependence of the LWFC wall's lateral resistance to adequate dowel action at the horizontal connections. Reduced compressive strength led to crushing of LWFC alongside the grouted rebar and premature slip at the horizontal connections.

Normalised displacement comparison: A normalised displacement comparison between physical and FE test results reinforced the understanding of relative nolinear displacement mechanisms occurring at the same time within both the physical and FE tests.

7.2.3   Analytical Design

Lateral force capacity, connections slip dependence: The results of the FE tests and the observed slip at the horizontal connections for the physical tests gave confidence to the hypothesis: shear resistance of the connections determine the ultimate capacity of the walls under lateral load.

Analytical model: Ductility of both friction and dowel-action was confirmed by the FE sensitivity study to have a major contribution to the ductile lateral-displacement response of the precast LWFC walls. Thus for this model, less ductile adhesive and aggregate interlock shear resistance could be neglected. The analytical model therefore focussed on frictional and dowel-action resistance at the connection interface and provided similar lateral force resistances to the physical tests.

Wall stiffness, strength and ductility are important: The analytical model relies upon both friction and dowel action to develop a shear stress design limit. Without an adequately stiff and resistant wall between the two horizontal connections, the contribution of friction and dowel action would be diminished as sufficient shear force resistance would not develop. Reinforcement of LWFC walls is therefore important for overall rigidity and lateral force resistance. Interaction with sufficient bond between the bars and LWFC, as well as fracture energy of the LWFC, crack control to distributed cracks with fine widths contribute to the energy dissipation and overall wall system ductility and safety.

7.2.4 Precast LWFC System for Seismic Design

Reinforced LWFC: Reinforced LWFC walls failed in a predictable manner and gave ductile response as well as understandable crack patterns under high lateral loads well beyond the seismic demand in the region of interest.

Precast, connected LWFC walls: The capacity and failure mechanisms of connected, precast LWFC walls are sensitive to the number of connections, connection location and connection placement. The energy dissipating ability of LWFC walls is also dependent on these factors and a balance of global and local displacement must be ensured to prevent brittle failure.

Seismic resistance: LWFC reinforced precast panels have definite potential for structural applications in seismic regions and surpass the static lateral force requirements of SANS 10160-4:2017.

7.3 Recommendations for Future Research

The following section details recommendations for future research of both physical scale tests and numerical analyses of reinforced LWFC.

Sustained vertical load: After analysing the results it is recommended that hydraulic control for applying sustained vertical load be researched and utilised for future testing.

Friction tests: Conduct tests to determine the coefficient of static friction between the LWFC-NWC and LWFC-LWFC interface.

Advanced control for physical tests: Make use of a shear-wall test frame for future tests to prevent slip of the test setup.

Detailed FE connection boxes: A likely improvement to the FE model will be to create detailed connection boxes at the vertical connection. In contrast to the current simplification of a dowel rebar across the connection, accurately modelled connection boxes will allow slip and vertical displacement that was seen in PST 1.

FE data extrapolation: A further step regarding the FE models would be to "fit" the physical test curves by altering the material properties; utilising the results of the sensitivity study.

Different element shape: To prevent possible shear and volumetric (inelastic) locking it is suggested that cross-triangle elements be used in place of the current quadrilateral elements for future FE models.

Analytical sensitivity study: It is recommended that an in-depth sensitivity study be conducted to enlarge the use of the simpler, analytical model for future codification.

Appendices

Appendix A

Connection Details

A.1   Vertical Connection Bracket

Figure A.1: *Longer vertical connection box after tensile test, l = 70 mm.*

Figure A.2: *Shorter vertical connection box after tensile test, l = 50 mm.*
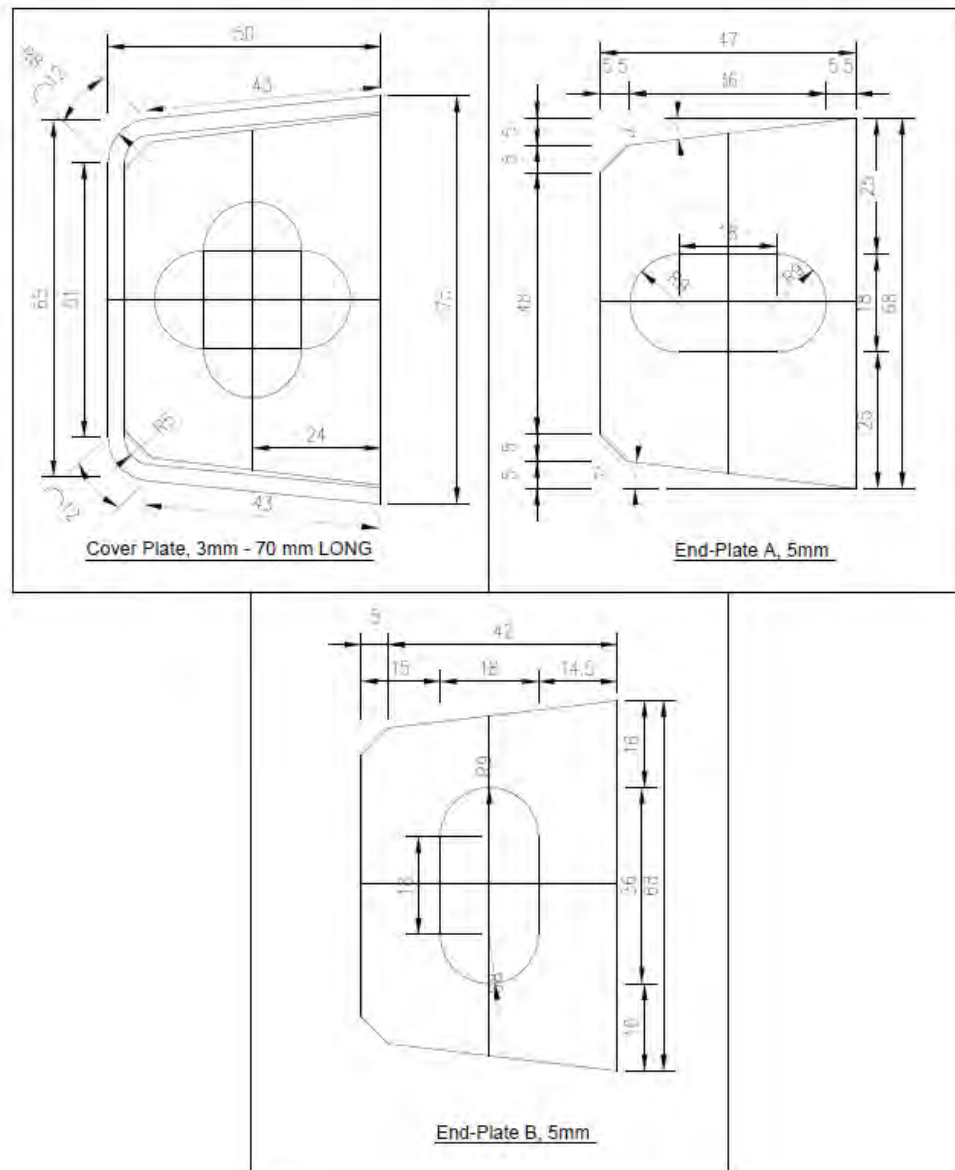
Figure A.3: *Vertical connection box bracket detail drawing (CCW, 2017) indicating side A and B and the dimensions of steel used*

Appendix B

Detailed Design of Global Experiment

Figure B.1: *Detailed reinforcement and connection layout for physical scale tests in Section (3.2.1)*
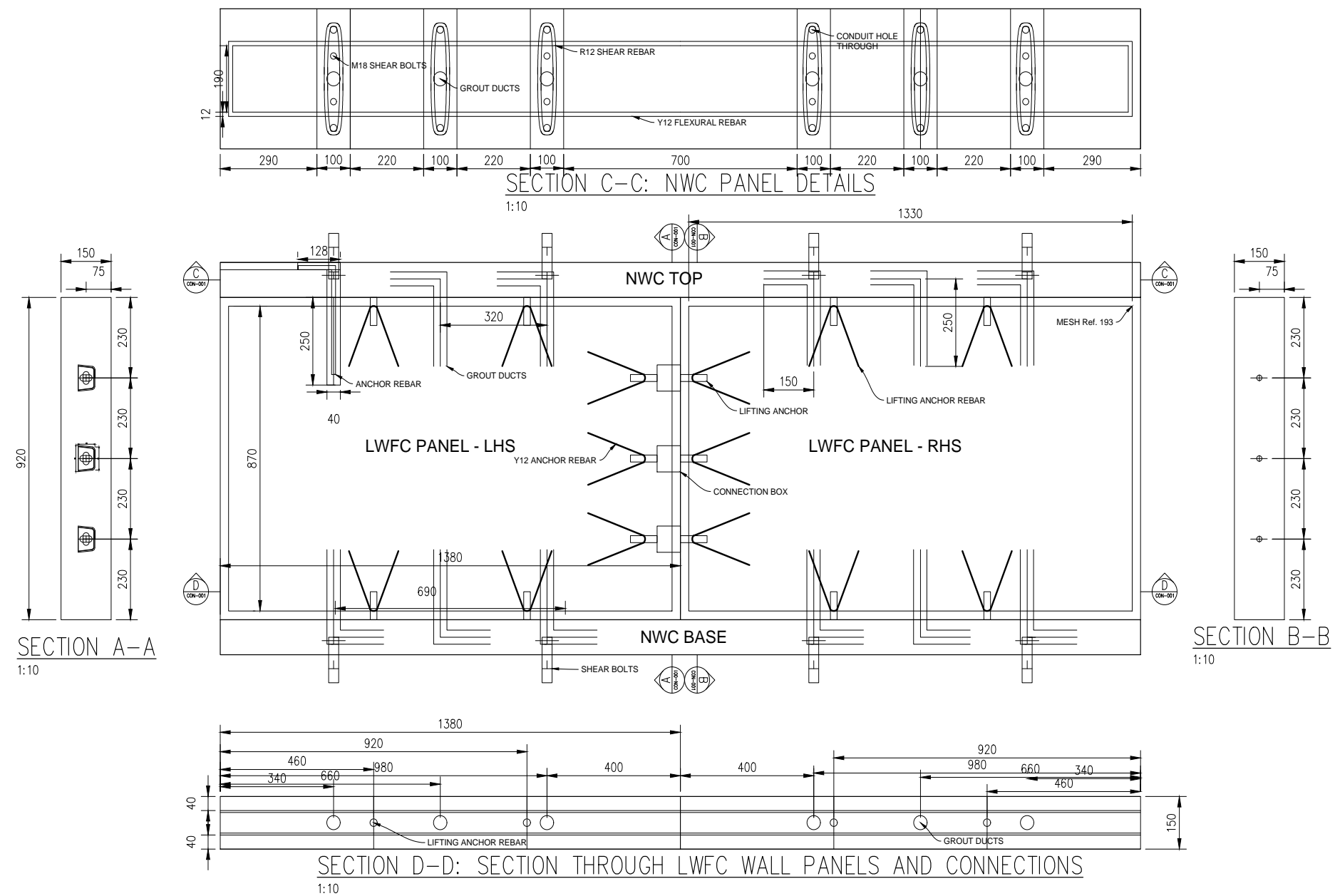
Appendix C

Calibration Test Results

C.1   Tensile Tests

Figure C.1: *Tensile test results of Y12 rebar: Stress-strain curves according to SANS 6892-1:2010 SANS (2010).*

List of References

Brühwiler, E. and Wittmann, F. (1990). The wedge splitting test, a new method of performing stable fracture mechanics tests. *Engineering Fracture Mechanics*, vol. 35, no. 1, pp. 117 – 125. ISSN 0013-7944.
Available at: `http://www.sciencedirect.com/science/article/pii/001379449090189N`

BSI (2004). *BS EN 1992-1-1: 2004- Eurocode 2: Design of concrete structures-Part 1-1: General rules and rules for buildings.* British Standards Institution. London.

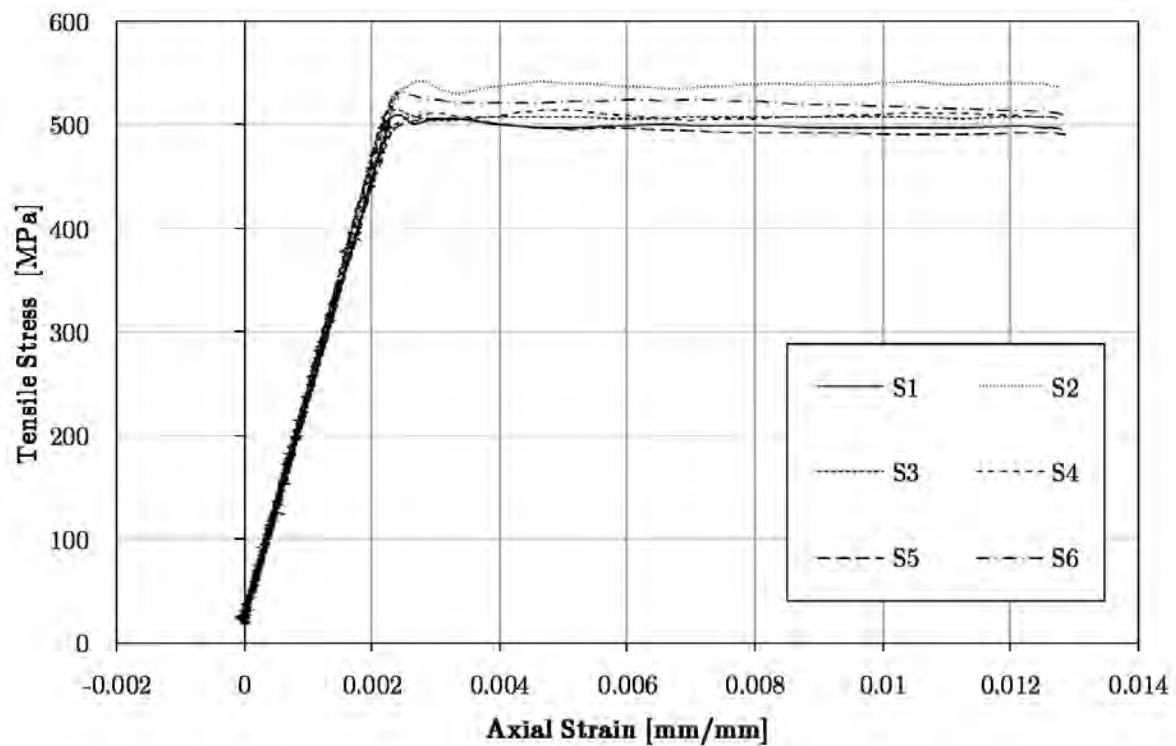BSI (2013). *BS EN 12390-13:2013 - Testing hardened concrete, Determination of secant modulus of elasticity in compression.* British Standards Institution. London.

Bull, D., Barnard, D., Brown, B., Fenwick, R., Hopkins, D., McSaveney, L., Park, R., Restrepo, J. and Wilkinson, R. (1999). *Guidelines for the Use of Structural Precast Concrete in Buildings:*, vol. 2. Centre for Advanced Engineering, University of Canterbury, Christchurch, New Zealand. ISBN 0-908993-20-X.

CCW (2017). Cape concrete works.
Available at: `http://www.capeconcrete.com/`

Crisafulli, F.J., Restrepo, J.I. and Park, R. (2002). Seismic design of lightly reinforced precast concrete rectangular wall panels. *PCI journal*, vol. 47, no. 4, pp. 104–121.

Curiel-Sosa, J., Beg, O. and Murillo, J.L. (2013). Finite element analysis of structural instability using an implicit/explicit switching technique. *International Journal for Computational Methods in Engineering Science and Mechanics*, vol. 14, no. 5, pp. 452–464.

De Beer, L. (2016). *Developing and testing a sprayable overlay of strain hardening cement-based composite for retrofitting of unreinforced load bearing masonry walls.* Master's thesis, Stellenbosch University.

De Villiers, J. (2015). *Bond behaviour of deformed steel reinforcement in lightweight foamed concrete.* mathesis, Stellenbosch University.

De Villiers, J., Van Zijl, G. and van Rooyen, A. (2016). Fracture of lightweight foamed concrete in evaluation of bond behaviour of steel reinforcement embedded in LWFC. *Proceedings of the 9th International Conference on Fracture Mechanics of Concrete and Concrete Structures.*
Available at: `http://framcos.org/FraMCoS-9/Full-Papers/289.pdf`

De Villiers, J., van Zijl, G. and van Rooyen, A. (2017). Bond of deformed steel reinforcement in lightweight foamed concrete. *Structural Concrete.*

DIANA FEA BV (2016*a*). *Diana 10·1 User's Manual: Concrete and Masonry Analysis.*
Available at: `dianafea.com`

DIANA FEA BV (2016*b*). *Diana 10·1 User's Manual: Element Library.*
Available at: `dianafea.com`

DIANA FEA BV (2016*c*). *Diana 10·1 User's Manual: Material Library.*
Available at: `dianafea.com`

Dörr, K. (1980). *Ein Beitrag zur Berechnung von Stahlbetonscheiben unter besonderer Berücksichtigung des Verbundverhaltens.* phdthesis, University of Darmstadt.

El Zareef, M. and Schlaich, M. (2008). *Bond behaviour between GFR bars and infra-lightweight concrete*, pp. 721–727. ISBN 9780415475358.

Elices, M., Guinea, G. and Planas, J. (1992). Measurement of the fracture energy using three-point bend tests: Part 3-influence of cutting the p-δ tail. *Materials and Structures*, vol. 25, no. 6, pp. 327–334.

E&OE (2017). Reinforcement mesh in southern africa.
Available at: `http://www.stewartsandlloyds.co.za/Portals/0/Products/SteelProducts/ReinforcingMesh.pdf`

Feenstra, P., De Borst, R. and Rots, J. (1991). A comparison of different crack models applied to plain and reinforced concrete. In: *Proceedings of the International RILEM/ESIS Conference" Fracture Processes in Concrete, Rock and Ceramics", Noordwijk, The Netherlands, 19-21 June 1991.*

Fenwick, R., Bull, D.K. and Gardiner, D. (2010). Assessment of hollow-core floors for seismic performance.

fib Model Code (2010). Special activity group 5. *fib Bulletin*, , no. 55.

Fine Software (2017). Contact elements.
Available at: `http://www.finesoftware.eu/help/geo5/en/contact-elements-01/`

FIP (1983). *FIP Manual of lightweight aggregate concrete.* Surry University Press.

Grafe, J. (2017). Report issue *s*0117: Optimization of fibre content in foam concrete for improved fracture behaviour. techreport, Institue of Structural Engineering, Stellenbosch University, South Africa.

Hadipramana, J., Samad, A.A.A., Zaidi, A.M.A., Mohammad, N. and Ali, N. (2013). Contribution of polypropylene fibre in improving strength of foamed concrete. In: *Advanced Materials Research*, vol. 626, pp. 762–768. Trans Tech Publ, Trans Tech Publications, Switzerland.

Hancilar, U., Durukal, E. and Erdik, M. (2010). Seismic assessment and rehabilitation of historical unreinforced masonry (urm) buildings in istanbul. In: *Improving the Seismic Performance of Existing Buildings and Other Structures*, pp. 1305–1316.

Hillerborg, A., Modeer, M. and Petersson, P. (1976). Analysis of crack formation and crack growth in concrete by means of fracture mechanics and finite elements. *Cement and Concrete Research*, vol. 6, pp. 773–781.

Hordijk, D.A. (1991). *Local Approach to Fatigue of Concrete.* Ph.D. thesis, Delft University of Technology.

JCI (2003). *Method of test for fracture energy of concrete by use of notched beam JCI-S-001-2003.*

Jensen, J., Bull, D. and Pampanin, S. (2007). Experimental investigation of existing hollowcore seating connection seismic behaviour pre and post retrofit intervention.

Jones, M. and McCarthy, A. (2005). Preliminary views on the potential of foamed concrete as a structural material. *Magazine of concrete research*, vol. 57, no. 1, pp. 21–32.

Kearsley, E. (1996). The use of foamed concrete for affordable development in third world countries. *Concrete in the Service of Mankind: Appropriate Concrete Technology*, vol. 3, p. 232.

Kearsley, E. and Mostert, H. (2003). The effect of polypropylene fibres on the properties of foamed concrete. In: *Proceedings of International Symposium: Role of Concrete in Sustainable Development, Dundee, Scotland*, pp. 557–566.

Kearsley, E. and Mostert, H. (2005). Designing mix composition of foamed concrete with high fly ash contents. In: *Use of Foamed Concrete in Construction: Proceedings of the International Conference held at the University of Dundee, Scotland, UK on 5 July 2005*, pp. 29–36. Thomas Telford Publishing.

Kearsley, E. and Wainwright, P. (2001). The effect of high fly ash content on the compressive strength of foamed concrete. *Cement and concrete research*, vol. 31, no. 1, pp. 105–112.

Kearsley, E. and Wainwright, P. (2002). Ash content for optimum strength of foamed concrete. *Cement and concrete research*, vol. 32, no. 2, pp. 241–246.

Kozlowski, M., Kadela, M. and Kukielka, A. (2015). Fracture energy of foamed concrete based on three-point bending test on notched beams. *Procedia Engineering*, vol. 108, pp. 349 – 354. ISSN 1877-7058.
Available at: `http://www.sciencedirect.com/science/article/pii/S187770581501111X`

Leonhardt, F. and Mönnig, E. (1977). *Vorlesungen über Massivbau. 3. Grundlagen zum Bewehren im Stahlbetonbau.* Springer.

Maekawa, K., Okamura, H. and Pimanmas, A. (2003). *Non-linear mechanics of reinforced concrete.* CRC Press.

McNaught, A. and Wilkinson, A. (1997). *Compendium of Chemical Terminology–The Gold Book, 2nd Edition.* Blackwell Science: Oxford.
Available at: `http://goldbook.iupac.org/pdf/goldbook.pdf`

Mydin, M.A.O. and Soleimanzadeh, S. (2012). Effect of polypropylene fiber content on flexural strength of lightweight foamed concrete at ambient and elevated temperatures. *Advances in Applied Science Research*, vol. 3, no. 5, pp. 2837–2846.

Narayanan, N. and Ramamurthy, K. (2000). Structure and properties of aerated concrete: a review. *Cement and Concrete Composites*, vol. 22, no. 5, pp. 321–329.

Negro, P. and Toniolo, G. (2012). Jrc scientific and policy report: Design guidelines for connections of precast structures under seismic actions.

NZS (1995). *NZS 3101-1&2:1995-Concrete Structures Standards-Parts 1 and 2.*

Oginni, F.A. (2015). Continental application of foamed concrete technology: Lessons for infrastructural development in africa. *British Journal of Applied Science & Technology*, vol. 5, no. 4, p. 417.

Oluokun, F. (1991). Prediction of concrete tensile strength from its compressive strength: an evaluation of existing relations for normal weight concrete. *ACI Materials Journal*, vol. 88, no. 3, pp. 302–309.

Pall, A.S., Marsh, C. and Fazio, P. (1980). Friction joints for seismic control of large panel structures. *PCI JOURNAL*, vol. 25, no. 6, pp. 38–61.

Park, R. (1995). A perspective on the seismic design of precast concrete structures in new zealand. *PCI journal*, vol. 40, no. 3.

Park, R. (2002). Seismic design and construction of precast concrete buildings in new zealand. *PCI journal*, vol. 47, no. 5, pp. 60–75.

PPC (2017). Ppc opc cem ii 52.5n.
Available at: `http://www.ppc.co.za/products/cement/products/opc/#.WYxi84iGMOO`

Rasheed, A. and Prakash, S. (2016). Effect of synthetic fiber reinforcement on compression and tension behavious of cellular lightweight concrete.

Retief, J.V. and Dunaiski, P. (2009). *Background to SANS 10160: Basis of structural design and actions for buildings and industrial structures*. AFRICAN SUN MeDIA.

RILEM (1985). Fmc 50 committee - determination of the fracture energy of mortar and concrete by means of three-point bending tests on notched beams. *Materials and Structures*, vol. 85, no. 85, pp. 285–290.

SANS (2000). *SANS 0100-1: 2000 - The structural use of concrete- Part 1: Design*. The South African Bureau of Standards.

SANS (2006). *SANS 5863:2006 - Concrete Testing - Compressive strength of hardened concrete*. The South African Bureau of Standards.

SANS (2010). *SANS 6892-1:2010 - Metallic materials - Tensile testing - Part 1: Method of test at room temperature*. The South African Bureau of Standards.

SANS (2011a). *SANS 10160-1:2011 - Basis of structural design and actions for buildings and industrial structures- Part 1: Basis of structural design*. The South African Bureau of Standards.

SANS (2011b). *SANS 10160-2:2011 - Basis of structural design and actions for buildings and industrial structures- Part 2: Self-weight and imposed loads*. The South African Bureau of Standards.

SANS (2011c). *SANS 920: 2011 - Steel bars for concrete reinforcement*. The South African Bureau of Standards.

SANS (2013). *SANS 50197-1:2013 - Cement- Part 1: Composition, specifications and conformity criteria for common cements*. The South African Bureau of Standards.

SANS (2014). *SANS 50450-1:2014 - Fly ash for concrete - Part 1: Definition, specifications and conformity criteria*. The South African Bureau of Standards.

SANS (2017). *SANS 10160-4:2017 - Basis of structural design and actions for buildings and industrial structures- Part 4: Seismic actions and general requirements for buildings*. The South African Bureau of Standards.

SAPY (2016). Sapy corehfil[TM] polypropylene fibres.
Available at: `http://sapy.com/wp-content/uploads/2016/06/SAPY-Corehfil-brochure.pdf`

Sauter, F. (1984). Earthquake resistant criteria for precast concrete structures. In: *Proc. 8th World Conf on Earthq Eng*, pp. 629–636.

Seifi, P., Henry, R. and Ingham, J. (2016). Panel connection details in existing new zealand precast concrete buildings. *Bulletin of the New Zealand Society for Earthquake Engineering*, vol. 49, no. 2.

Sika (2016). *SikaGrout ® 212 High Strength shrinkage conpensated cementicious grout.* Available at: `http://zaf.sika.com/dms/getdocument.get/aca6b2d7-b061-352c-8e7a-c4a10d2cddc7/SikaGrout%20-212.pdf`

Singh, M., Kijko, A. and Durrheim, R. (2009). Seismotectonic models for south africa: Synthesis of geoscientific information, problems, and the way forward. *Seismological Research Letters*, vol. 80, no. 1, pp. 71–80.

Smith, I.A. (1967). The design of fly-ash concretes. In: *Inst Civil Engineers Proc London,/UK/.*

Thorenfeldt, E., Tomaszewicz, A. and Jensen, J. (1987). Mechanical properties of high-strength concrete and application in design. In: *Proceedings of the symposium utilization of high strength concrete*, pp. 149–159. Tapir Trondheim Norway.

Ulula Ash (Pty)Ltd (2016). Ulula ash kriel power station: Test certificate for class s fly-ash. Available at: `http://www.ululaflyash.com/documents/Test%20CertificateTypical%2050450%20ClassS.pdf`

Van Rooyen, A. (2013). *Structural lightweight aerated concrete.* mathesis, Stellenbosch University.

Van Zijl, G. (2000). *Computational Modelling of Masonry Creep and Shrinkage.* phdthesis, Delft University of Technology.

Van Zijl, G., Van Rooyen, A., Mubatapasango, M., Dunn, T. and Grafe, J. (2017). Durability and bond of reinforced lightweight foamed concrete. In: *High Tech Concrete: Where Technology and Engineering Meet*, pp. 2185–2193. Springer.

Wittmann, F. (2002). Crack formation and fracture energy of normal and high strength concrete. *Sadhana*, vol. 27, no. 4, pp. 413–423.